AGH University of Science and Technology
Kraków, Poland

Faculty of Computer Science, Electronics and Telecommunications
Department of Electronics

Ph. D. Thesis

Witold Skowroński

Current induced magnetization switching and noise characterization of MgO based magnetic tunnel junctions

Supervisors:
Prof. Tomasz Stobiecki
Prof. Sebastiaan van Dijken

Kraków 2013

Witold Skowroński

Current induced magnetization switching and noise characterization of MgO based magnetic tunnel junctions

AGH University of Science and Technology

AGH UNIVERSITY OF SCIENCE AND TECHNOLOGY

DEPARTMENT OF ELECTRONICS

Supervisors:
prof. Tomasz Stobiecki
prof. Sebastiaan van Dijken

Declaration
I hereby declare that the work in this thesis is my own original work, except where indicated in the text.

Section Current induced magnetization switching in MTJ with a wedge MgO tunnel barrier is based on the publication: Skowroński, W., Stobiecki, T., Wrona, J., Rott, K., Thomas, A., Reiss, G., and van Dijken, S. *Journal of Applied Physics* **107**(9), 093917 (2010)

Section Optimal barrier parameters for spin torque memory application: TMR, coupling, damping is based on the publication: Serrano-Guisan, S., Skowroński, W., Wrona, J., Liebing, N., Czapkiewicz, M., Stobiecki, T., Reiss, G., and Schumacher, H. W. *Journal of Applied Physics* **110**(2), 023906 (2011)

Section Direct measurements of the spin transfer torque using ST-FMR is based on the publication: Skowroński W., Czapkieiwcz M., Frankowski M., Wrona J., Stobiecki T., Reiss G., Chalapat K., Paraoanu G. and van Dijken S., *arXiv*:1301.7186

Section High frequency spin torque oscillator based on MTJ with tilted free layer is based on the publication: Skowroński, W., Stobiecki, T., Wrona, J., Reiss, G., and van Dijken, S. *Applied Physics Express* **5**(6), 063005 (2012)

February 2013

Abstract

Recent developments in nanotechnology triggered intensive research on thin-film multilayer systems. It was found, that the properties of materials shrunk to a nanometer scale differ from those known from a macro world. In particular, an effective control and use of particle's spin (apart from its charge, which is a basic principal of the operation of electronic devices) is possible in a nanoscale and it gave rise to a new science field of spin-electronics. In spin-electronics, or spintronics, the control of the element's magnetization, which is directly coupled to the spin of the electrons, is of great importance as it allows for the design of novel spin-electronic devices.

This thesis presents detailed studies of magnetic tunnel junctions (MTJs), which is currently one of the most universal spintronic devices. The current induced magnetization switching (CIMS) effect, which is observed in MTJs with extremely thin (below 1 nm) tunnel barriers, creates a new mechanism of controlling the magnetization of the thin magnetic films, which is used, for example, in storage devices.

The thesis begins with a general introduction, which provides a necessary theoretical and technological background. Afterwards, a series of experiments investigating CIMS effect in MTJs are described in detail. A deeper insight into this phenomena led to an investigation of the spin-transfer-torque (STT) effect using dynamic experimental methods. The physics of STT gives a comprehensive description of the magnetization control by means of spin polarized currents. This part of the thesis was concluded by finding the optimal tunnel barrier parameters of MTJs for the memory device applications. Next, the low frequency noise measurements were performed on the same devices, in order to estimate the different electric and magnetic noise contributions to the overall device performance. Finally, by optimizing the magnetic free layer of the MTJ, a spin-torque oscillator prototype was proposed, which operates at the microwave-frequency range without the presence of the external magnetic field.

The thesis ends with both theoretical and practical implications of the results obtained during the PhD course. The optimization of the MTJs' tunnel barrier is important for the design of a novel magnetic memory cell, based on this technology. The microwave-oscillations measured in the optimized MTJ could in principal be

used in telecommunication systems, as a nano-oscillator. In the conclusion, a general outlook of nano-magnetism and spintronics is provided.

Acknowledgments

I would like to thank my supervisors: PROF. TOMASZ STOBIECKI and PROF. SEBASTIAAN VAN DIJKEN for their guidance throughout my PhD course and their enormous help in my research. I am grateful to PROF. TOMASZ STOBIECKI for the introduction to spintronics and magnetism and his constant encouragement. To PROF. SEBASTIAAN VAN DIJKEN I am thankful for his excellent advises and pointing the right direction.

My special thanks to my colleges from AGH: PIOTR WIŚNIOWSKI, WIESŁAW POWROŹNIK, JAROSŁAW KANAK, MAREK FRANKOWSKI, ALIKSANDR ZALESKI, ANTONI ŻYWCZAK, ZBIGNIEW SZKLARSKI and PIOTR MIETNIOWSKI who helped me in various ways. Particularly, I would like to acknowledge excellent samples from JERZY WRONA and accurate physical remarks from MACIEJ CZAPKIEWICZ. In addition, I am grateful to PIOTR OGRODNIK, MICHAŁ WILCZYŃSKI from Warsaw University of Technology and PROF. JÓZEF BARNAŚ from University in Poznań for fruitful theoretical discussions.

I am also grateful for enormous help from prof. GÜNTER REISS and his group at Bielefeld University. I would like to acknowledge ANDY THOMAS, AG VENKATESH, MARKUS SCHÄFFERS, VOLKER DREVELLO, PATRYK KRZYSTECZKO and, especially, KARSTEN ROTT, for their help in nanofabrication process and measurements techniques.

I thank members of PROF. SEBASTIAAN VAN DIJKEN's group at Aalto University: TUOMAS LAHTINEN, LAURA ÄKÄSLOMPOLO, LIDE YAO, KEVIN FRANKE, MIKKO KATAJA and SAMPO HÄMÄLÄINEN. I am especially grateful to QIHANG QIN for his help in the fabrication processes.

The collaboration with PROF. HANS SCHUMACHER and SANTIAGO SERRANO-GUISAN at PTB Braunschweig is gratefully acknowledged.

Finally, I would like to thank my family, my mother and my father in particular, and to my KAROLINA for their infinite support, to whom I dedicate this thesis.

My PhD program was financed by the Foundation for Polish Science through Krakow Interdisciplinary PhD-Project in Nanoscience and Advanced Nanostructures MPD Programme, co-financed by the EU European Regional Development Fund. Special thanks to PROF. BARTŁOMIEJ SZAFRAN who was the coordinator of the MPD program. Part of the research was also financed by the Polish Ministry of Science and Higher Education grant IP 2010037970, National Science Center grant NN 515544538, statutory activity grant 11.11.120.614 and Nanospin PSB-045-2010 project.

Contents

List of Figures

List of Tables

List of Abbreviation

AF - antiferromagnet
AFM - atomic force microscopy
AP - antiparallel
AM - amplitude modulation
AMR - anisotropy magnetoresistance
BCC - body center cubic
CIMS - current induced magnetization switching
CIPT - current in-plane tunneling
CMOS - complementary metal-oxide semiconductor
CPW - coplanar waveguide
DAC - digital to analogue converter
DAQ - data acquisition card
DC - direct current
DOS - density of states
DRAM - dynamic random access memory
DUT - device under test
FFT - fast Fourier transform
FL - free layer
G-S - ground signal configuration
GMR - giant magnetoresistance
HDD - hard disc drive
IEC - interlayer exchange coupling
IT - information technology
LLD - linear dynamic deposition
LLG - Landau-Lifshitz-Gilbert equation
MBE - molecular beam epitaxy
ML - monolayer
MRAM - magnetic random access memory
MOKE - magneto-optical Kerr effect
MTJ - magnetic tunnel junction
P - parallel
PCB - printed circuit board
PCM - phase change memory
PIMM - pulse inductive microwave magnetometer
PL - pinned layer
PSV - pseudo spin valve
PVD - physical vapor deposition
RA - resistance area product
RAM - random access memory

RF - radio frequency
RKKY - Ruderman-Kittel-Kasuya-Yosida interaction
RL - reference layer
RTN - random telegraph noise
SAF - synthetic antiferromagnet
SEM - scanning electron microscope
SMA - SubMiniature version A
SRAM - static random access memory
ST-FMR - spin torque ferromagnetic resonance
STO - spin torque oscillator
STT - spin transfer torque
TEM - transmission electron microscope
TMR - tunneling magnetoresistance
UHF - ultra high vacuum
VSM - vibrating sample magnetometer
XRD - X-ray diffraction

1 Introduction

This thesis discusses an effective control of the magnetization using spin polarized currents in the materials shrunk to nanometer scale dimensions. Information, next to knowledge, is considered the new goods, next to for example, the materials or energy. More and more information is being produced at an exponentially increasing rate. Storing this enormous amount of data has been a key problem in preserving civilization's knowledge and culture.

Up to now, one of the most effective ways of storing information has been achieved by placing texts and drawings on sheets of paper. However, the amount of paper produced every year is not capable of storing all the information our civilization currently produces, when taking into account, for example, all the stock exchange data, banking information, CCTV) images, etc. Thanks to a recent development in electronics, a digital electronic memory concept was introduced, that is capable of storing amounts of data, that people could not have predicted[1].

CCTV - closed circuit television

[1] Excerpt from brilliant minds like Richard Feynman stating: *Why can we not write the entire 24 volumes of the Encyclopedia Britannica on the head of a pin?*

To sustain this trend of ever increasing memory capacity, much effort has been put in by scientists and engineers to develop new memory devices based on different physical mechanisms. For decades, information stored in magnetic bits, either on spool tapes, tiny magnetic cores or discs plates has been one of the most reliable data storage concepts. However, ongoing research of further optimizing electronic memory performance, considering especially its power consumption, is of great importance.

Figure 1.1 presents the global power consumption of the IT devices predicted for another 15 years. In the next two decades, an increase in the energy consumption by a factor of nine is expected, which will eventually correspond to 15% of global power generation. Taking into account the limited amount of energy our civilization is able to produce nowadays, the IT power consumption must be reduced.

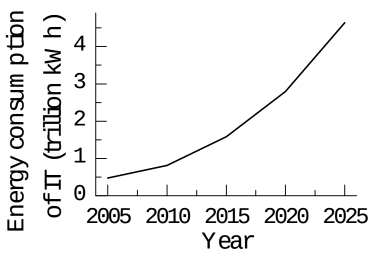

Figure 1.1: The global consumption of IT appliances, data from Japans Ministry of Economy, Trade and Industry, 2008
Adapted from S. Yuasa, unpublished.

In modern IT devices architecture, one can distinguish between two major types of memories. One, capacious, with a long data retention, typically represented by a HDD, and the other, smaller but much faster RAM used for frequent access operations. By reducing the power consumption of the first type of memory, one can improve, for example, the storage centers efficiency[2].

IT - information technology
HDD - hard disc drive
RAM - random access memory

[2] In 2011 data centers consumed about 2% of the total electric power in the USA.

However, tremendous change in both the IT devices efficiency and their functionality can be expected if current RAMs could be replaced with a fast and capacious nonvolatile memory. If one were to unplug a computer equipped with such memory and plug it back in at any time, it would remember all the information without a need to reboot. Moreover, such a computer could be in the off-state most of the time, when no interruption from user occurs. This could radically reduce it's power consumption.

A new approach towards designing of electronic circuits (especially integrated circuits) was proposed by H. Ohno[3], where a distribution of the memory elements within the circuit will reduce the electrical connections length and, therefore, increase the operation speed and reduce the power losses.

Magnetic RAM, produced by Everspin [4] is already available on the commercial market. Magnetic fields generated by the bit- and word-lines supplied with current pulses changes the orientation of the magnetization of the memory-cell. Up to date, the operation speed of 35 ns and capacity of 16 MB was achieved in this non-volatile technology. Reaching higher memory density in a field-driven design is limited, therefore a new magnetization control mechanism is needed.

[3] Takemura, R., Kawahara, T., Miura, K., Yamamoto, H., Hayakawa, J., Matsuzaki, N., Ono, K., Yamanouchi, M., Ito, K., Takahashi, H., Ikeda, S., Hasegawa, H., Matsuoka, H., and Ohno, H. *IEEE Journal of Solid-State Circuits* **45**(4), 869 (2010)

[4] http://www.everspin.com/

1.1 *Objective and scope*

The effective control of the magnetization of nano-scale materials is a very important problem in designing of the electronic memories that are capable of preserving the Moore's Law of density storage increase.

In this thesis it is proposed that high density, non-volatile and fast electronic RAM can be implemented by using a technology based on MTJ, using STT effect. The readout of each memory bit is possible thanks to a different resistance of the MTJ in parallel and antiparallel state, which is called the TMR effect. A similar mechanism has been engaged in MTJ-based field-driven devices. The control of the bit state, on the other hand, is realized using STT, which radically improves scalability of the MRAM, which can theoretically go beyond current DRAM technologies.

RAM - random access memory

MTJ - magnetic tunnel junction

STT - spin-transfer torque

TMR - tunneling magnetoresistance

MRAM - magnetic random access memory

DRAM - dynamic random access memory

The main building block of this memory - the MTJ, consist of two thin ferromagnetic electrodes, one magnetically hard, i.e., it is very difficult to change it's magnetization direction and the other, which is susceptible to the magnetization change. These two ferromagnets are separated by a thin insulating barrier.

The desired design of the memory cell is realized, when two bistable states are energetically equal when no external energy (for example from external magnetic fields or the STT) is delivered to the system. In MTJ, one boolean state is encoded, when the magnetic orientation of the two ferromagnets are parallel to each other, whereas, the second one, when they are antiparallel. The condition with bistable states of the MTJ-cell is fulfilled, for example, by se-

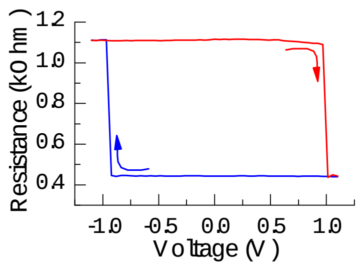

Figure 1.2: Bistable memory cell controlled with electric voltage. Starting from a high-resistance state and increasing voltage, the critical value is passed, and the system switches to the low-resistance state. Similarly decreasing voltage, switching back to the high-resistance state is realized.

lecting the proper physical dimensions of the magnetic layer. Figure 1.2 presents the MTJ resistance vs. applied voltage hysteresis loop of designed memory cell. Two states are easily detectable by the difference in the MTJ resistance.

The switching between these bistable states is realized by using voltage (current) pulses alone, without a need of external magnetic fields. Thus, two main memory-cell operations, i.e., writing and reading are performed with the same two-terminal connection using electrical signals.

However, the potential applications of the STT effects goes beyond memories. By taking advantage of the STT effect, it is possible to induce a precession of the magnetization in the nanomagnet. Typically these precessions lie within the microwave regime and can be controlled with a DC voltage (and external magnetic field). The electric detection (for example using spectrum analyzer) enables applications of such devices in conventional electronics. Due to the extremely small sizes of the oscillating elements, such observations are of great interest for the microwave electronics and telecommunication applications.

DC - direct current

Along with the extremely successful past of the MTJ, nanomagnetism and spintronics also have a very bright future. The control of the spin of the individual particle, opens up a highly anticipated perspective of using an additional particle's degree of freedom in the processing and storage of the information.

1.2 Research process

The research process used in this thesis is following: firstly, based on the theoretical prediction and existing knowledge, the experiments were designed. In practice, at the beginning, the multilayer structure consisting of different conducting (magnetic and nonmagnetic) and insulating materials was proposed. In most of the cases, an advanced technology of Singulus AG [5] was utilized. As a result, a few inch diameter wafers with layer thicknesses down to a few atomic monolayers, were deposited with excellent uniformity and parameters. After the deposition, the wafers were thoroughly characterized using various methods, from structural (XRD, AFM, TEM) to magnetic (MOKE, VSM, PIMM, CIPT).

[5] www.singulus.com

XRD - X-ray diffraction
AFM - atomic force microscopy
TEM - transmission electron microscopy

MOKE - magneto-optical Kerr effect
VSM - vibrating sample magnetometer
PIMM - pulse inductive microwave magnetometer
CIPT - current in-plane tunneling

Next, on the chosen multilayer samples, a nanolithography process was performed resulting in prototype spintronic devices. Usually, multilayers were patterned into planar shapes [6] with the appropriate electrical connections. The prototypes require two electrodes to pass the electrical current vertically through the device. After the patterning, the sample device was characterized electrically. Experimental observation were confronted with the theoretical prediction and complex analysis was undertaken to understand the physics behind the device.

[6] The specific shape was chosen depending on the device properties

1.3 *Guide to thesis*

The success of spin-electronics is well reflected in a number of publications and scientific thesis, presented after the introduction of the MTJ device and the discovery of the STT effect. In this thesis, the main effort was put on optimizing the insulating barrier parameters, important from the MTJ application point of view.

Research on this PhD course initiated with a first observation of the CIMS effect in Fall 2008. One-direction current induced switching, from the high- to low-resistive MTJ state was measured in a home-built transport measurement setup, on samples delivered by scientific partner INESC-MN. This observation coincided with a development of the MTJ sputtering process at Singulus AG with a thin insulating MgO barrier, which is crucial for STT-based switching observation. After an intensive nanolithography course at Bielefeld University a series of MTJs with a varied thickness of MgO barrier were fabricated. Detailed measurements and theoretical analysis led to the first publication, presented in section 3.1. In addition, the original publication is extended by the temperature dependent magneto-transport measurements and the finite-element model estimation of the temperature increase of the MTJ during switching events. Finally, the backhopping effect observed in the MTJ are described.

INESC-MN - Investigacao, Educacao, Incubacao, Consultoria Tecnologica - Micorsystemas & Nanotecnologias, Lisbon, Portugal

Similar unpatterned MTJ samples were investigated using dynamic inductive methods. This research, performed in cooperation with PTB Braunschweig group, focused on an investigation of the effective magnetic damping, which directly influences the current-induced switching performance of the MTJs. The description of these studies, presented in section 3.2 is enriched with the theoretical energy model, necessary to determine the MTJ parameters from the measurements.

PTB - Physikalisch-Technische Bundesanstalt

Section 3.3 contains the investigation of the STT effects, based on the so-called spin-torque diode effect measurements. Initial measurements of spin-torque diode signals led to a deeper insight into the STT components. Detailed analysis of the spin-torque ferromagnetic resonance, supported by the macrospin simulations, revealed the complex influence of the coupling on the magnetization homogeneity. Based on the experimental procedure described in Ref. [7] the STT-components are derived.

[7] Wang, C., Cui, Y., Sun, J., Katine, J., Buhrman, R., and Ralph, D. *Physical Review B* **79**(22), 224416 (2009)

Finally, a low and high frequency noise is investigated in sections 3.4 and 3.5, respectively. The different noise contributions to the overall magnetic and electric noise is discussed. By optimizing the free magnetic layer properties and taking advantage of the coupling, which is thoroughly described in the previous sections, a prototype spin-torque nano-oscillator is proposed.

The thesis concludes with theoretical and practical implications of the results obtained. After the summary, the outlook and possible ways of development of the field of spintronics and nanomagnetism is discussed.

2

Theoretical foundations

Good experimental work should be preceded with a proper theoretical background. The theoretical foundation for this thesis is divided into a few sections. First, the fundamental definitions of the magnetic tunnel junction is provided. It consist of a description of the quantum tunneling mechanism through a thin insulating barrier and specifically the crystalline magnesium oxide barrier. Also, the band structure of utilized ferromagnetic electrodes is discussed, which is inherently connected with the spin polarization. Afterwards, the macrospin model is introduced, which describes the behavior of a nanomagnet in the presence of the external magnetic field. Next, the magnetic coupling description present in MTJs is provided. Thereafter, the spin transfer torque effect is introduced with its basic idea and comprehensive theoretical model that predicts two components of STT. Finally, both a low and high frequency noise, which is characteristic for MTJs is discussed.

2.1 Magnetic tunnel junction

The magnetic tunnel junction was discovered by Jullier in 1975[1]. The MTJ's principals of operation were as following. Two thin ferromagnetic films, in this case made of iron and cobalt, separated by a 10 nm (semi)insulating germanium film, made up the very first MTJ. Transport measurement performed at liquid helium temperature[2] showed that by changing the magnetic orientation of Fe and Co electrodes from parallel to antiparallel the conductance of the stack changes by 16% - Fig. 2.1.

The explanation of the observed phenomenon is as following. Certain bias voltage (V_B = 4 mV) was applied in order to measure the resistance. The voltage potential caused effective change of the Fermi levels in the ferromagnets, thus electron started to tunnel through the energy barrier, towards positive voltage potential. The spin of the electrons were aligned with the magnetization direction of the source electrode (with a certain efficiency called spin polarization). It was assumed, that this spin was conserved during the tunneling and the process of entering the second ferromagnetic electrode depends on it's magnetic orientation. When the orientation was parallel to the source electrode, there were many unoc-

[1] Julliere, M. *Physics Letters* **54A**(3), 225 (1975)

[2] In order to enhance physical properties and reduce an influence of the thermal noise on the measurement, very often initial investigation of certain physics are performed at liquid helium - 4.2 K or liquid nitrogen temperatures - 88 K)

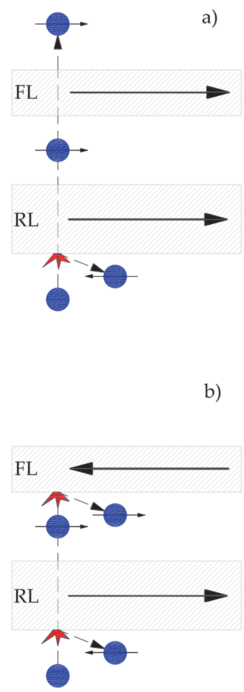

Figure 2.1: Schematic of the TMR effect in investigated MTJ trilayer. When the magnetizations of the FL and RL are parallel, spin-polarized electrons can pass through both layers (a). When the magnetizations are antiparallel FL (RL) does not allow electrons of spins aligned along RL (FL), which results in higher electrical resistance (b).

cupied states the electron could tunnel to and smaller resistance was measured. Contrary, if the orientation of the second electrode was antiparallel, the electrons encounter less available states, and the probability of reflection and thus electrical resistance increases. More detailed explanation includes the band structure discussion of the ferromagnetic electrodes.

In order to experimentally observe the TMR effect, two ferromagnets should change the magnetization at different magnetic fields, so that both parallel and antiparallel state are stable at given magnetic field. In other words, they should have a different coercive field. Practically, one of the layers should be magnetically harder and constitute so called RL, than the other, magnetically softer FL. To achieve this situation, called the PSV structure, it is possible to use different materials or different thickness of electrodes.

RL - reference layer

FL - free layer

PSV - pseudo spin-valve

For practical applications, however, a multilayer system with an exchange bias [3] and synthetic antiferromagnet was engineered. In this structure, the RL is deposited on the additional magnetic layer called PL , from which it is separated by a thin Ru layer (typically 0.8 - 0.9 nm thick). Such combination results in antiferromagnetically coupled RL and PL. This system is called SAF (detailed description of this mechanism is provided in section 2.1.5). The PL is deposited directly on an antiferromagnet. When such bilayer is annealed and cooled through the Néel temperature of the antiferromagnet, an exchange bias is induced. As a result, PL has a strong unidirectional anisotropy with the direction along the top antiferromagnet layer and antiferromagnetically coupled to it RL has, therefore, fixed magnetization.

[3] Dieny, B., Speriosu, V. S., Gurney, B. A., Parkin, S. S. P., Wilhoit, D. R., Roche, K. P., Metin, S., Peterson, D. T., and Nadimi, S. *Journal of Magnetism and Magnetic Materials* **93**, 101 (1991); and Nogues, J. and Schuller, I. K. *Journal of Magnetism and Magnetic Materials* **192**, 203 (1999)

PL - pinned layer

SAF - synthetic antiferromagnet

Material	Spin polarization (%)
Fe	44
Co	34
Ni	11
Heusler	100

Table 2.1: Spin polarization of certain ferromagnetic materials measured using the tunneling method by Tedrow and Meservey

Adapted from Tedrow, P. M. and Meservey, R. *Physical Review B* **7**(1), 318 (1973).

2.1.1 *Spin polarization*

Spin polarization is the key phenomena necessary to understand the principals of the operation of any spintronics device. In nonmagnetic metal, for example in a long copper wire, the electrons carry randomly distributed spin. In ferromagnetic materials on the other, the conducting electrons tend to align it's spin parallel to the local magnetization direction, which results in positive spin polarization or antiparallel, resulting in a negative spin polarization.

Therefore, injection of the electrons to the uniformly magnetized thin film will result in spin polarized currents on the output. Spin polarization is the inherent property of the ferromagnet and depends mainly on the band structure of the material and density of states at given energy level. An alternative way of obtaining high spin-polarized currents using Spin Hall Effect [4] or spin-pumping phenomena [5] have been also proposed.

[4] Liu, L., Pai, C.-F., Li, Y., Tseng, H. W., Ralph, D. C., and Buhrman, R. A. *Science* **336**(6081), 555 (2012)

[5] Kajiwara, Y., Harii, K., Takahashi, S., Ohe, J., Uchida, K., Mizuguchi, M., Umezawa, H., Kawai, H., Ando, K., Takanashi, K., Maekawa, S., and Saitoh, E. *Nature* **464**(7286), 262 March (2010)

An example of a calculated spin resolved band structure is presented in Fig. 2.2. The density of states at the Fermi energy for up and spin bands are not equal but they differ by an exchange splitting parameter. Thus, from theoretical calculations, the spin polarization can be derived directly from DOS, according to the following equation:

$$p = \frac{D_\uparrow(E_F) - D_\downarrow(E_F)}{D_\uparrow(E_F) + D_\downarrow(E_F)} \tag{2.1}$$

In the experiments, however, it was discovered that the spin polarization of Fe, Co and Ni is positive, although, based on data presented in Fig. 2.2 and Eq. 2.1 it should be negative, i.e., dominated by the electrons with down-spins (minority). Moreover, such simple model cannot predict an influence of the tunnel barrier parameters, like height or thickness, on the spin polarization.

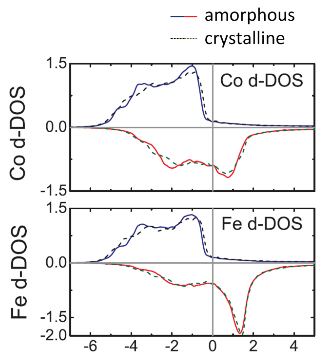

Figure 2.2: Spin resolved density of 3d states calculated for amorphous Fe and Co. At the Fermi energy level (E = 0), a clear difference in DOS is observed.

Adapted from Paluskar, P., Attema, J., de Wijs, G., Fiddy, S., Snoeck, E., Kohlhepp, J., Swagten, H., de Groot, R., and Koopmans, B. *Physical Review Letters* **100**(5) February (2008).

The first theoretical approach in building more complex model was done by Slonczewski [6]. He assumed that the ferromagnets separated by thin tunnel barrier are not independent. Each electrode was described using parabolic-shape bands (one for majority and one for minority spins) shifted in energy by a value of the exchange splitting. By solving the Schrödinger equation of such system he calculated the spin polarization:

[6] Slonczewski, J. C. *Physical Review B* **39**(10), 6995 (1989)

$$p = \frac{k^\uparrow - k^\downarrow}{k^\uparrow + k^\downarrow}\frac{\kappa^2 - k^\uparrow k^\downarrow}{\kappa^2 + k^\uparrow k^\downarrow} \tag{2.2}$$

where, $k^\uparrow$ and $k^\downarrow$ are the Fermi wave vectors of the up and down-spin bands and $\hbar\kappa = \sqrt{2m\,(E_b - E_F)}$, with m being the electron mass, and E_b the tunnel barrier height. With wave vectors proportional to the density of states at the Fermi energy level, first term in Eq. 2.2 corresponds to Eq. 2.1. The second term depends highly on the barrier parameter and can even change the sign of the spin polarization, thus, explain the experimental observation. Even more realistic values can be predicted using theory based on Landauer formalism [7], tight-binding models [8] or *ab initio* approach (see details in section 3.3.5).

[7] Moodera, J. and Mathon, G. *Journal of Magnetism and Magnetic Materials* **200**, 248 (1999)

[8] Mathon, J. *Physical Review B* **56**(18), 11810 (1997)

2.1.2 *Tunneling magnetoresistance*

The resistance of the MTJ depends on the orientation of the two ferromagnetic electrodes. In order to calculate the TMR ratio, the Julliere model is commonly used:

$$TMR = \frac{R_{AP} - R_P}{R_P} = \frac{2p_1p_2}{1 - p_1p_2} \tag{2.3}$$

R_{AP} and R_P are the resistance measured at antiparallel and parallel magnetic orientation respectively and p_1 and p_2 are the spin polarization of two ferromagnetic electrodes respectively.

A simple model developed by Julliere gives a qualitative estimation of the TMR ratio. To give more accurate results, other approaches were proposed to predict the magnetoresistance, including the numerical evaluations [9] and *ab initio* approach [10]. More practically, the effective spin polarization in case of symmetric electrodes, can be calculated based on measured TMR ratio:

[9] MacLaren, J. M., Zhang, X. G., and Butler, W. H. *Physical Review B* **56**(18), 11827 (1997)

[10] Butler, W., Zhang, X., Schulthess, T., and MacLaren, J. *Physical Review B* **63**(5), 054416 (2001)

$$p = \sqrt{\frac{TMR}{2 + TMR}} \tag{2.4}$$

In addition, phenomenologically, the resistance R of the MTJ is the cosine function of the angle θ between the magnetization orientation of two ferromagnetic electrodes [11]:

$$R = R_p + \frac{R_{ap} - R_p}{2} (1 - \cos\theta) \tag{2.5}$$

[11] Rijks, T. G. S. M., Coehoorn, R., Daemen, J. T. F., and de Jonge, W. J. M. *Journal of Applied Physics* **76**(2), 1092 (1994)

2.1.3 *Incoherent and coherent tunneling*

As mentioned, when bias voltage is applied to the MTJ, the electrons tunnel quantum mechanically through the tunnel barrier, conserving the spin orientation. In reality however, the tunneling process also depends on the parameters of the tunnel barrier itself. Tunneling process via an amorphous barrier (for example Al_2O_3) allows every electronic state (Bloch state) to tunnel with an equal probability. This situation is depicted in Fig. 2.3a. This situation was assumed by Slonczewski in Eq. 2.2.

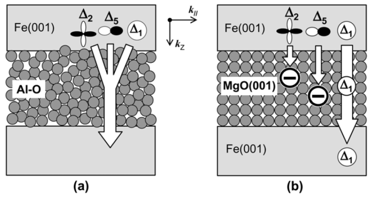

Figure 2.3: Sketch of the tunneling process in an amorphous (a) and crystalline (b) barrier.
Adapted from Yuasa, S. and Djayaprawira, D. D. *Journal of Physics D: Applied Physics* **40**, R337 (2007).

This tunneling process can be described as incoherent tunneling. In the case of crystalline tunnel barriers the situation is very different. In ferromagnetic metals, electronic states with a certain symmetry (Δ_1) have higher spin polarization than the others (Δ_2, Δ_5)[12]. Crystalline barriers, like BCC(001) MgO for example, can grow epitaxially on certain ferromagnetic materials, like Fe, Co or its compounds. Ideal crystal barrier favor only certain electronic states. In the case of MgO, electrons with Δ_1 symmetry dominate during the tunneling process. Due to the fact that these electrons are highly spin polarized, higher TMR ratios can be expected. Discussion on the crystalline structure of the MTJ fabricated for the purpose of this thesis can be found in section 5.1.

[12] Yuasa, S. and Djayaprawira, D. D. *Journal of Physics D: Applied Physics* **40**, R337 (2007)

BCC - body center cubic

The tunneling process and spin polarization is therefore bound together, and often the Julliere approach is not precise. Due to the technological issues, an ideal crystal is difficult to grow and therefore, the extremely high TMR values of 1000% predicted by the theory are hard to obtain [13]. To date, the highest TMR measured reached 604 % at room temperature (value measured at 5 K increased to 1140 %) [14]. Crystalline tunnel barriers can be considered as active barriers, because they can enhance the magnetoresistive properties of the devices. Later in this work, mostly structures with a poly-crystalline MgO barrier will be discussed.

[13] Mathon, J. *Contemporary Physics* **32**(3), 143 (1991); Butler, W., Zhang, X., Schulthess, T., and MacLaren, J. *Physical Review B* **63**(5), 054416 (2001); and Tsymbal, E. Y., Mryasov, O. N., and LeClair, P. *Journal of Physics: Condensed Matter* **15**(4), R109 (2003)

[14] Ikeda, S., Hayakawa, J., Ashizawa, Y., Lee, Y. M., Miura, K., Hasegawa, H., Tsunoda, M., Matsukura, F., and Ohno, H. *Applied Physics Letters* **93**(8), 082508 (2008)

2.1.4 *Macrospin energy model*

The most common model that describes the behavior of the ferromagnet in the presence of an external magnetic field is the Stoner-Wolfarth model [15]. This model assumes a coherent rotation of the magnetization, i.e., the magnetism in the entire magnet is uniform and can be described using a single vector $\vec{M}$.

[15] Stoner, E. C. and Wohlfarth, E. P. *Phil. Trans. R. Soc. Lond. A* **240**, 599 (1948)

In a general approach, the ferromagnetic layer can be described using the following energy density equation:

$$E = -\mu_0 M_s \vec{m} \circ \vec{H} - \frac{\mu_0 M_s}{2} \vec{H}_D \circ \vec{m} - K_u \vec{m} \circ \vec{m}' \tag{2.6}$$

where, $\vec{m} = \frac{\vec{M}}{M_s}$ is the unit remanence magnetization vector, $\vec{H}$ is the magnetic field vector K_u is the uniaxial energy constant, $\vec{m}'$ is the magnetization direction in the presence of the magnetic field and $\vec{H_D}$ is the demagnetization field: $\vec{H_D} = N\vec{M}$, where N is the demagnetization tensor. In the case of unpatterned thin film, the demagnetization term favors in-plane magnetization and therefore $N = (0\ 0\ 1)$[16]. Terms in Eq. 2.6 corresponds to the Zeeman energy, demagnetization energy and anisotropy energy, respectively.

[16] If patterned samples are considered, demagnetization tensor data can be found for example in Cornelissen, S., Bianchini, L., Helmer, A., Devolder, T., Kim, J., de Beeck, M. O., Roy, W. V., Lagae, L., and Chappert, C. *Journal of Applied Physics* **105**(7), 07B903 (2009)

Assuming that both the magnetic field and the uniaxial magnetic anisotropy lie in the sample plane and the MTJ stack consists of FL, RL, PL and AF, Eq. 2.6 can be rewritten as follows:

$$E = -\sum_j (\mu_0 M_j H \cos\theta_j \cos(\phi_j - \varphi) + \frac{1}{2}\mu_0 M_j H_D +$$
$$+ K_j \cos^2\theta_j \cos^2\phi_j + \frac{J_j}{t_j}\cos(\theta_j - \theta_{j+1})\cos(\phi_j - \phi_{j+1})) \tag{2.7}$$

where, $\mu_0 M_j$ is the magnetization of the j layer in T, H is the external magnetic field in A/m, (θ, ϕ) are the polar coordinates of the magnetization of j layer, φ is the in-plane orientation of the magnetic field with respect to the easy magnetization axis, K_j is the uniaxial energy constant of the j layer and t_j is the j layer thickness. The last, additional term in this equation, J_j is the exchange energy constant (coupling energy) between j and the $j+1$ layer, i.e., the coupling between FL and RL, between RL and PL and between PL and AF. For the AF layer has no net magnetic moment: $M_{AF} = 0$.

In order to calculate angels θ and ϕ for given material parameters and the external magnetic field H, it is necessary to find the energy minimum - Eq. 2.7. For the purposes of this thesis, software MAGEN2, developed by M. Czapkiewicz, which calculates the energy minimum by means of a gradient search method, was used.[17] This approach enables macrospin simulation of the magnetic hysteresis curve of the multilayer system. On the basis of Eq. 2.5 it is also possible to calculate the normalized TMR loop. The above described model is used in sctions 3.1, 3.2 and 3.3.

[17] MAGEN2, developed by M. Czapkiewicz, AGH 2009

Apart from the macrospin model, many different approaches were proposed to simulate more complicated magnetic structures. These models are necessary when the magnetization in one layer is not uniform, but rather inhomogeneous. Such inhomogeneity can arise from interface roughness, complex planar shape (see section 5.2) or interplay between various coupling mechanisms, discussed below. Often, the magnetic structure consist of regions which has uniform magnetization, called magnetic domains, separated by borders, called domain walls.

2.1.5 Coupling mechanisms

Another physical phenomena observed in the system when two ferromagnetic films are placed very close to each other are the various types of coupling between them. Especially in MTJs, where the insulators thickness is typically in the range of 0.5 - 3 nm, the magnetization of one layer will strongly depend on the orientation of the other.

The most common type of coupling is the magnetostatic coupling. Similarly to the macro-scale world, two magnets (dipoles) placed parallel and close to each other will align themselves antiferromagnetically due to the stray fields interactions. The exact estimation of the magnetostatic coupling energy is possible using either an analytic approach [18] or numerical micromagnetic simulations.

[18] Engel-Herbert, R. and Hesjedal, T. *Journal of Applied Physics* **97**(7), 074504 (2005)

A simple trilayer with two 2-nm thick ferromagnets separated by a 1 nm thin insulator with an elliptical cross-section of 150 × 250 nm, presented in Fig. 2.4, was implemented in OOMMF. The magnetic anisotropy energy of 100 J/m^3 and the saturation magnetization of 1080 kA/m (corresponding to $\mu_0 M_s$ = 1.35 T) was assumed.

OOMMF - The Object Oriented MicroMagnetic Framework project http://math.nist.gov/oommf/

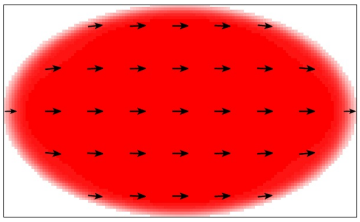

Figure 2.4: Cross-section of the FL of the simulated MTJ structure. Arrows indicate magnetization direction.

The resistance vs. magnetic field applied along a longer axis of the ellipse was simulated using magneto-resistance extension developed in Ref. [19]. The magnetoresistance hysteresis loop, presented in Fig. 2.5 is shifted towards the negative fields by H_s = -120 Oe, which evidence an antiferromagnetic coupling. Assuming that:

$$J = \mu_0 M_s H_s t \tag{2.8}$$

where, H_s is the loop shift in A/m, the coupling energy J = -26 μJ/m^2. It should be noted that smaller offset fields originating from the stray fields interactions are measured in experiments (see section 3.3), because simulation is performed on ideal pillar structures without any roughness or shape imperfection, however a similar tendency is retained.

[19] Frankowski, M. *MSc thesis*. AGH University of Science and Technology, (2012)

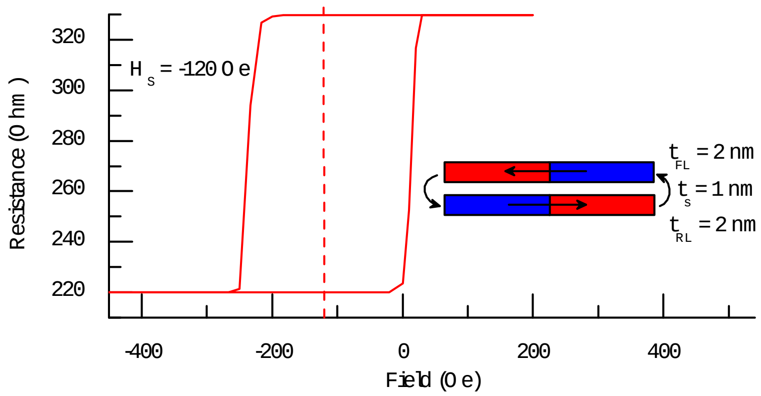

Figure 2.5: Resistance vs. magnetic field loop simulated using an OOMMF package, simulated by M. Czapkiewicz. Antiferromagnetic coupling is evidenced by the loop shift towards negative field values.

Another source of coupling is non-ideal interface between layers in the system. Dependent on the multilayer deposition process as well as the materials used, typically the interface is not ideally smooth, but rough. Physically, it means that small magnetic dipoles created in the roughness pits and ditches will create small stray fields, which favors parallel magnetization of the two ferromagnets separated by a non-magnetic spacer - Fig. 2.6. This type of coupling is referred to as Néel coupling or "orange-peel" coupling.

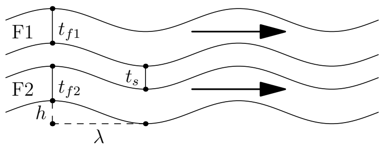

Figure 2.6: Schematics of the magnetostatic coupling called Neél coupling or "orange-peel" coupling present in a trilayer system with rough interfaces.

In order to estimate these effects, an analytic model was developed by Kools et al. [20]. When two ferromagnets with thicknesses of t_{f1} and t_{f2} are separated by a non-magnetic spacer with a thickness of t_s the interface roughness can be estimated using a sine wave function, with a magnitude of h and a wavelength of λ, the offset magnetic field (coupling energy) can be calculated from the following formula:

[20] Kools, J. C. S., Kula, W., Mauri, D., and Lin, T. *Journal of Applied Physics* **85**, 4466 (1999)

$$H_s = \frac{\pi^2 h^2 M_s}{\sqrt{2}\lambda t_{f1}} \left(1 - \exp\left(\frac{-2\pi\sqrt{2}t_{f1}}{\lambda}\right)\right) \times \left(1 - \exp\left(\frac{-2\pi\sqrt{2}t_{f2}}{\lambda}\right)\right) \exp\left(\frac{-2\pi\sqrt{2}t_s}{\lambda}\right) \tag{2.9}$$

AFM - Atomic force microscope

Practically, by measuring the interfaces roughness, using for example AFM one can estimate the "orange-peel" coupling contribution [21].

[21] Stobiecki, T., Kanak, J., Wrona, J., Reiss, G., and Brückl, H. *Journal of Magnetism and Magnetic Materials* **316**(2), e998 September (2007); and Kanak, J. *PhD thesis*. AGH University of Science and Technology, (2006)

Finally, the magnetic coupling in the multilayer system is caused by the interaction between electrons in two ferromagnets placed closely together. This type of coupling was observed experimentally for the first time in 1986 by Grünberg et al. [22]. Two Fe layers separated by a thin Cr spacer were antiferromagnetically coupled and this type of coupling was called IEC.

[22] Grünberg, P. A., Schreiber, R., and Pang, Y. *Physical Review Letters* **57**(19), 2442 (1986)

IEC - Interlayer exchange coupling

Later on, in 1990 Parkin et al. discovered the oscillating character of this coupling, from antiferromagnetic to ferromagnetic and that it is a function of the spacer thickness [23]. The magnitude of the coupling changes approximately as $\cos(x)/x^3$ with a period of π/k_F [24]. Theoretically, it was possible to predict interaction between electrons using the RKKY model, where magnetic moments of nucleus in the ferromagnets are coupled using electrons of *s* and *d* shell.

[23] Parkin, S. S. P., More, N., and Roche, K. P. *Physical Review Letters* **64**(19), 2304 (1990)

[24] Czapkiewicz, M. *PhD thesis*. AGH University of Science and Technology, (1999)

Thanks to the oscillating character of this coupling, it was possible to design a first magnetoresistive read head for a disc drive based on the GMR effect [25].

RKKY - Ruderman-Kittel-Kasuya-Yosida interaction
GMR - Giant magnetoresistance

IEC is also present in MTJs with tunnel barrier spacer. In the Fe/MgO/Fe trilayer, a coupling energy was measured and calculated using the Slonczewski model as a function of the tunnel barrier thickness [26]. The authors discovered, that the coupling changes monotonically from weak ferromagnetic above 0.8 nm thick MgO to strong antiferromagnetic interaction below 0.8 nm down to 0.5 nm. Similar behavior was observed by Katayama et al. [27], where additionally, IEC was estimated from *ab initio* calculations for an ideal Fe/MgO/Fe and for the MTJs with O vacancies. Depending on the multilayer quality and especially the quality of the interfaces, the IEC can be either ferro- or antiferromagnetic.

[25] Baibich, M. N., Broto, J. M., Fert, A., Van Dau, F. N., Petroff, F., Etienne, P., Creuzet, G., Friederich, A., and Chazelas, J. *Physical Review Letters* **61**(21), 2472 (1988)

[26] Faure-Vincent, J., Tiusan, C., Bellouard, C., Popova, E., Hehn, M., Montaigne, F., and Schuhl, A. *Physical Review Letters* **89**(10), 107206 (2002)

[27] Katayama, T., Yuasa, S., Velev, J., Zhuravlev, M. Y., Jaswal, S. S., and Tsymbal, E. Y. *Applied Physics Letters* **89**(11), 112503 (2006)

All the above mentioned coupling mechanisms exist in MTJs and are of particular importance in junctions with the thin (below 1 nm) tunnel barrier discussed in this thesis. They scale in a different way dependent on the materials thicknesses and sizes, different coupling signs help to identify each contribution and also enable one to use them in the device design.

2.2 *Spin transfer torque*

Controlling the magnetization of the nanoscale elements in an efficient way is the key issue for designing non-volatile magnetic memories. Existing magnetic memories (both hard disc drives and MRAMs) take advantage of Ampere's law, where writing heads or bit- and word lines are supplied with a high density current, that induces a rotation magnetic field around them, that can manipulate the magnetic moment of the writing layer. Using Ampere's law, however, becomes inefficient as the dimension of the storage cell decreases below micrometer size. Therefore, high capacities of MRAM with this approach are not possible.

The mechanism of the spin polarization, described in section 2.1.1 was a relatively well known mechanism for producing spin polarized current by injecting unpolarized electrons to a magnetized layer.

In 1996 two theoreticians, Slonczewski [28] and Berger [29] independently predicted the existence of the so called STT effect, which describes the behavior of the magnet with the presence of a spin polarized current flow. This groundbreaking theory model predicted that the spin polarized current flowing through a nanomagnet can also affect it's magnetization.

[28] Slonczewski, J. C. *Journal of Magnetism and Magnetic Materials* **159**(1-2), L1 (1996)
[29] Berger, L. *Physical Review B* **54**(13), 9353 (1996)

STT - Spin Transfer Torque

2.2.1 *Toy model*

Let us discuss a typical geometry of the MTJ presented in Fig. 2.7. The magnetically hard RL is separated from the softer FL by a thin tunnel barrier. The bias voltage is applied, so that the electrons tunnel from the RL towards the FL (in this thesis, positive voltage always denotes electron tunneling from the RL to the FL). Randomly polarized electrons passing through the RL will be effectively polarized along the RL magnetization with an efficiency proportional to the material's polarization. It is assumed that while tunneling through the barrier, the spin of the electrons is conserved (spin diffusion length is longer than the barrier thickness). Again, entering the FL the electrons will be polarized along the FL magnetization. However, if the FL is soft enough, its magnetization will be affected by the incoming electrons' spin. This situation is the most effective when the magnetization direction of the RL and FL are different (especially antiparallel). The spin carried by the electrons will be transferred from the RL to FL and the torque will change the orientation of the magnetization of the FL towards parallel to the RL - Fig. 2.7a.

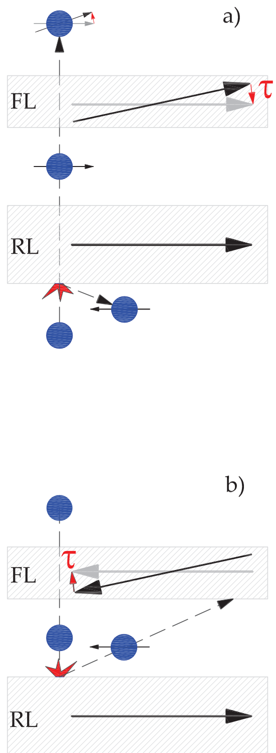

Figure 2.7: Schematic of the STT in the discussed MTJ trilayer. Electrons tunneling from the RL to the FL favor parallel magnetization alignment (a), whereas, electrons tunneling from the FL to the RL favor an antiparallel magnetization state (b). The black arrows indicate initial magnetization direction, whereas, grey arrows indicate final magnetization direction, after the torque is exerted (red arrows).

The situation is different when voltage of the opposite polarity is applied. The electrons are polarized in the FL and tunnel towards RL. The RL is energetically much more stable, and therefore the electrons that have spin opposite to its magnetization will be reflected. These electrons, with spins antiparallel to the RL direction accumulate in the FL and finally change its magnetization. This voltage polarity will favor the anti-parallel magnetization state - Fig. 2.7b. Because CIMS from the P to AP state is based on the electrons reflection effect, the spin-torque efficiency (see section 2.2.2) is typically smaller than the opposite CIMS from AP to A state.

If a system is designed, so that there are only two energy minima for the FL, for example if the shape and the crystalline anisotropy will favor only 0° and 180° orientation of the magnetization with respect to the RL - Fig. 2.8 - the magnetization can be switched from the P to AP state by only using a spin polarized current. This effect is called CIMS.

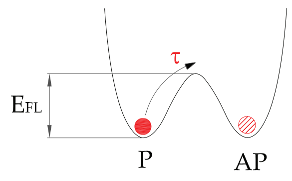

Figure 2.8: Energy profile of the MTJ's FL with two bistable states. Without an external energy delivered to the system, the MTJ can be either in the P or AP magnetization state. The switching between these states is realized by means of a spin polarized current that exerts torque (τ) on the FL. E_{FL} correspond to the energy barrier that has to be overcome during a switching event.

CIMS - Current Induced Magnetization Switching

2.2.2 *Critical current*

In order to calculate the current that is able to flip the magnetization from P to AP and in reverse, called the critical current, the energy delivered to the system by a spin polarized current can be compared to the energy of the FL. The energy E_I of the current I can be written as:

$$E_I = \eta \frac{\hbar}{2e} I \tag{2.10}$$

where, η is the spin transfer efficiency $\hbar$ is the reduced Planck's constant and e is the electron charge. On the other hand, the energy of the FL E_{FL} is equal to:

$$E_{FL} = \mu_0 M_S H_{\text{eff}} A t \tag{2.11}$$

where H_{eff} is the effective magnetic field, A and t are the area and the thickness of the FL, respectively. Assuming that these two energies should be equal to each other and that the E_{FL} is diminished by an energy loss rate equal to the damping α, in order to change the magnetization of the FL one can calculate the critical current density [30], that is a quantitative estimation of the CIMS efficiency process:

[30] Sun, J. Z. *Physical Review B* **62**(1), 570 (2000)

$$J_{c0} = \frac{2e\alpha\mu_0 M_S H_{\text{eff}} t}{\eta\hbar} = \frac{2e\alpha E_{FL}}{\eta\hbar A} \tag{2.12}$$

Spin transfer efficiency can be phenomenologically expressed as:

$$\eta = \frac{p}{2\left(1 + p^2 \cos(\theta)\right)} \tag{2.13}$$

where p can be estimated using a Julliere model - Eq. 2.1 from the measured TMR using Eq. 2.3. J_{c0} can be easily reduced by decreasing the energy of the FL (mainly affected by the anisotropy), the effective damping α and by increasing the polarization p. This can be achieved by choosing different ferromagnetic materials, for example, characterized by a high perpendicular anisotropy, increased polarization and low effective damping. In order to estimate the effective magnetic field, one can analyze different field contributions. Typically, in the in-plane magnetized ferromagnetic layer, the effective field is the sum of the external magnetic field H_{eff}, anisotropy field H_a and the demagnetizing field which in the case of in-plane magnetized film is $H_D = \mu_0 M_S/2$

$$H_{\text{eff}} = H_{\text{ext}} \pm H_a \pm M_S/2 \tag{2.14}$$

It should be noted, that this effective field can be reduced, using FL materials with perpendicular magnetic anisotropy, this has been extensively investigated in recent years [31]. Although the anisotropy field of such materials is usually much higher than for the in-plane magnetized materials, H_{eff} in this case is reduced to:

[31] Ikeda, S., Miura, K., Yamamoto, H., Mizunuma, K., Gan, H. D., Endo, M., Kanai, S., Hayakawa, J., Matsukura, F., and Ohno, H. *Nature Materials* **9**(9), 721 (2010)

$$H_{\text{eff}} = H_{\text{ext}} \pm (H_a - M_S) \tag{2.15}$$

All quantities mentioned in Eqs. 2.12 - 2.15 are well known physical constant or material parameters that can be measured using static and dynamic magnetometer methods. Therefore, it is possible to estimate the J_{c0} based on this theory. In order to compare these value with the experimental findings, it is necessary to assume thermal effects [32]. In MTJs with a thin tunnel barrier exhibiting CIMS effects, the current density can reach $J = 10^8$ A/m^2 which can heat up the junction by over 100° C, depending on the current pulse duration t_p (for the detailed calculation see section 3.1.3). The temperature will affect the energy of the free layer and therefore the Jc will be lower. In a thermal activation regime phenomenological expression describing relation between t_p and Jc is:

[32] Kubota, H., Fukushima, A., Ootani, Y., Yuasa, S., Ando, K., Maehara, H., Tsunekawa, K., Djayaprawira, D. D., Watanabe, N., and Suzuki, Y. *Applied Physics Letters* **89**(3), 032505 (2006); and Hayakawa, J., Ikeda, S., Lee, Y. M., Sasaki, R., Meguro, T., Matsukura, F., Takahashi, H., and Ohno, H. *Japanese Journal of Applied Physics* **45**(40), L1057 (2006)

$$J_c = J_{c0}\left(1 - \left(\frac{2k_BT}{E_{FL}}\right)\ln\left(\frac{t_p}{t_0}\right)\right) \tag{2.16}$$

where T is the MTJ temperature and t_0 is the inverse of the attempt frequency, which is typically set to 1 ns. The term before the logarithm is inversely proportional to a thermal stability factor Δ:

$$\Delta = \frac{E_{FL}}{k_BT} \tag{2.17}$$

As pointed out, the J_{c0} can be reduced by decreasing E_{FL}, however, this would also reduce Δ. Practically, this would make the information (a bit) stored in the FL unstable with time or temperature. The industry standard implies $\Delta \geq 60$ [33], in order to retain the data stored in the memory for more than ten years.

[33] Khalili Amiri, P., Zeng, Z. M., Upadhyaya, P., Rowlands, G., Zhao, H., Krivorotov, I. N., Wang, J., Jiang, H. W., Katine, J. A., Langer, J., Galatsis, K., and Wang, K. L. *IEEE Electron Device Letters* **32**(1), 57 (2011)

2.2.3 *STT dynamics*

The estimation of the CIMS effects in a time regime below 10 ns, requires deeper insight into the STT dynamics.

The precessional motion of the magnetization in a magnetic body placed in the magnetic field is described by the LLG equation. If the effective magnetic field $\vec{H_{\text{eff}}}$ is applied to the magnet, its magnetization vector $\vec{M}$ will precess around the field direction[34]. Due to an inherit damping, this precession will vanish with an α constant [35]. With a presence of the STT, this precession can be sustained or amplified depending on current polarization.

LLG - Landau Lifshitz Gilbert equation

[34] Landau, L. D. and Lifshitz, E. *Phys. Z. Sowietunion* **100**, 1243 (1935)

[35] Gilbert, T. *Physical Review* **8**, 153 (1955)

This phenomenological description can be written as:

$$\begin{aligned} \frac{d\vec{M_{FL}}}{dt} &= -\gamma_0 \vec{M_{FL}} \times \vec{H_{\text{eff}}} + \alpha \vec{M_{FL}} \times \frac{d\vec{M_{FL}}}{dt} \\ &\quad -\gamma_0 \frac{\tau_{\|}}{M_S A t} \left(\vec{M_{FL}} \times \left(\vec{M_{FL}} \times \vec{M_{RL}} \right) \right) \\ &\quad -\gamma_0 \frac{\tau_{\perp}}{M_S A t} \left(\vec{M_{FL}} \times \vec{M_{RL}} \right) \end{aligned} \tag{2.18}$$

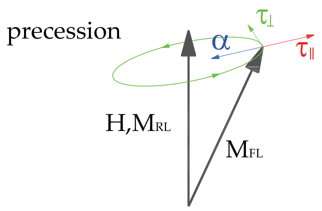

Figure 2.9: The directions of precession, damping and STT components in a nano-magnet. Note that α in this case indicates a damped torque, which acts against the STT induced by a spin polarized current.

where $\vec{M_{FL}}$ and $\vec{M_{RL}}$ are the magnetization vectors of the FL and the RL respectively, γ_0 is the gyromagnetic ratio and $\tau_{\|}$ and $\tau_{\perp}$ are the in-plane and perpendicular torque components predicted by the theory [36]. The first term on the right side of the Eq. 2.18 corresponds to the Landau-Lifshitz term (precession), the second one is a Gilbert term (damping), the third one is the in-plane torque (negative damping) and the fourth one is the perpendicular torque - Fig. 2.9.

[36] Slonczewski, J. C. *Journal of Magnetism and Magnetic Materials* **159**(1-2), L1 (1996)

This description has a few consequences. First of all, CIMS is the dynamic process. In time scale, which is comparable to an inverse of the attempt frequency $1/f_0 = 1$ ns, J_c is no longer *ln* of the pulse duration time, but switching of the FL or rather probability of switching depends on specific dynamical properties. Secondly, the magnetization precession is also excited by current densities smaller than J_c. Although no switching is observed, oscillations may be detected by measuring noise generated in a frequency characteristic for the nanomagnet.

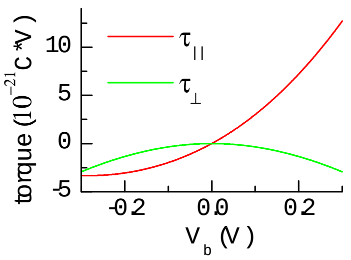

Figure 2.10: $\tau_{\|}$ and $\tau_{\perp}$ calculated for a low V_B range using the free-electron model by. M. Wilczyński

It is important to note, that STT has two perpendicular to each other components: $\tau_{\|}$ and $\tau_{\perp}$. In the case of in-plane magnetized materials, $\tau_{\|}$ has a direction opposite to the damping torque (Fig. 2.10). In addition, at low bias voltages, the magnitude of $\tau_{\|}$ is one order of magnitude greater than $\tau_{\perp}$ (for details see section 3.3) and, therefore, it is mainly responsible for the CIMS events. In the case of high bias voltages (of approximately 0.7 V in our case) $\tau_{\perp}$ starts to play an important role in CIMS. When both torque components have the opposite polarity, a backhopping effect [37], may occur. The backhopping is defined as a random switching from one stable magnetization state to the other and back (contrary to the simple situation presented in the section 2.2.1), which can significantly reduce the STT-RAM reliability.

[37] Sun, J. Z., Gaidis, M. C., Hu, G., O'Sullivan, E. J., Brown, S. L., Nowak, J. J., Trouilloud, P. L., and Worledge, D. C. *Journal of Applied Physics* **105**(7), 07D109 (2009)

Fig.2.10 presents $\tau_{\|}$ and $\tau_{\perp}$ calculated using a free-electron model [38] for the MTJ with an area of 0.022 μm^2, exchange splitting of 1.96 eV, fermi Energy of 2.62 eV, tunnel barrier thickness of 0.7 nm, barrier height of 1.5 eV and angle $\theta = 90^\circ$. $\tau_{\|}$ changes approximately linearly with V_B, whereas $\tau_{\perp}$ is a parabolic func-

[38] Wilczyński, M. *Journal of Magnetism and Magnetic Materials* **323**(11), 1529–1536 June (2011)

tion. Note, that $\tau_\perp$ = -0.25 $\times$ 10^{-19} CV for V_B = 0 (value subtracted in Fig. 2.10) is proportional to the interlayer exchange coupling. This value, calculated from the free-electron model corresponds to the coupling discussed in section 2.1.5. However, due to a complexity of the CoFeB/MgO interface [39], more advance approaches, including *ab initio* calculations must be used for precise coupling estimations.

[39] Yang, H. X., Chshiev, M., Kalitsov, A., Schuhl, A., and Butler, W. H. *Applied Physics Letters* **96**(26), 262509 (2010)

In addition to the free-electron model, the STT components can be calculated from atomic first principals [40]. At low bias voltage regime, up to V_B = 0.5 V in magnitude, the $\tau_\parallel$ and $\tau_\perp$ as a function of V_B are linear and quadratic, respectively, which agrees with the experimental results presented in section 3.3.

[40] Jia, X., Xia, K., Ke, Y., and Guo, H. *Physical Review B* **84**(1), 014401 (2011)

In order to estimate the characteristic frequency ω of a nanomagnet the Kittel formula[41] can be used:

$$\omega = \gamma_0 \sqrt{(H_{\text{ext}} \pm H_a)\,(H_{\text{ext}} \pm H_a + NM_S)} \tag{2.19}$$

[41] Kittel, C. *Phys. Rev.* **71**, 270 (1947)

where N is the matrix of the demagnetizing factors. For unpatterned thin film, the demagnetization matrix can be written as N_{up} = (0, 0, 1). For a patterned nanopillars, N depends on the film thickness, pillar dimensions and shapes. Table 2.2 presents demagnetizing factors for a few nanopillar examples. Depending on the different magnetic parameters, namely M_S and H_a, these frequencies are typically in the GHz regime.

Size (nm)	N_x	N_y	N_z
50 × 100	0.073	0.038	0.89
75 × 140	0.054	0.027	0.92
100 × 200	0.048	0.022	0.93

Table 2.2: Demagnetizing factors of a nanopillar shape MTJ calculated from the stray field model using OOMMF program.
Adapted from Cornelissen, S., Bianchini, L., Helmer, A., Devolder, T., Kim, J., de Beeck, M. O., Roy, W. V., Lagae, L., and Chappert, C. *Journal of Applied Physics* **105**(7), 07B903 (2009).

2.3 Noise

All electronic devices exhibit noise as their internal property, which is inseparably connected with the character of the charge transport. Noise can be divided into several types, depending on its origin. In addition, one can distinguish different mechanisms that make noise not only less destructive but also productive.

Thermal noise Every electronic component operating at a temperature above absolute zero [42] is subjected to a random fluctuation of electric charge in a conductive material, characterized by the resistance R. Such fluctuations can be regard as a Brownian motion in the electric carrier scale. Practically, the power spectral density per Hz of bandwidth of this noise can be approximated using the following formula:

[42] practically every device

$$\bar{v_n^2} = 4k_B TR \tag{2.20}$$

where k_B is the Boltzman's constant. The power spectral density is independent of the frequency spectrum and noise is considered *white*.

The 1 kΩ resistor will exhibit $\sqrt{\bar{v_n^2}}$ = 4.07 nV/$\sqrt{Hz}$ at room temperature

Shot noise Another kind of noise - the shot noise - can be measured when an electric current flows through a conductor. Considering the time-dependent fluctuation of the electric charge caused by the thermal fluctuation, stochastic and uncorrelated emission events result in a Poisson distribution noise with the following power density:

$$v_s^2 = 2eIR^2 \tag{2.21}$$

where I is the average DC current. A deviation from a Poissonian shot noise in MTJs can be measured, when current tunnels through a barrier [43]. Considering these two inevitable sources of noise, they can be modeled with the following expression:

[43] Lei, Z. Q., Li, G. J., Egelhoff, W. F., Lai, P. T., and Pong, P. W. T. *IEEE Transactions on Magnetics* **47**(3), 602 (2011)

$$v_{sn}^2 = 2eIR^2 \coth\left(\frac{eV}{2k_BT}\right) \tag{2.22}$$

For low voltages the total noise approaches a thermal noise limit, whereas, for a very low ambient temperature or high voltages it reaches a shot noise limit.

1/f noise The two noises mentioned above are frequency independent. At low frequencies, however, another type of distortion is visible called flicker noise or, because of its dependence on frequency , 1/f noise. Typically, the power density of 1/f noise is much higher at low (below a few hundreds of kHz) than thermal or shot noise and, therefore, affects mainly the devices working in this frequency range, such as magnetic field sensors. The common magnetoresistive sensors are based not only on the TMR effect, but also AMR and GMR effects [44].

AMR - anisotropy magnetoresistance

[44] Tumański, S. *Thin film magnetoresistive sensors*. IOP Publishing, Bristol, (2001)

The main origin of 1/f noise can be attributed to electrons trapping in the tunnel barriers and interfaces of the MTJ. Current flowing through a junction is subjected to local disturbances on various defects and therefore the carriers are effectively slowed down.

There is also a magnetic contribution to the overall 1/f noise. It was found, that the noise power increases near magnetic switching of the FL or RL [45]. The source of it may be associated with magnetic fluctuations caused by magnetic domain switching between stable states that exist close to the coercive fields.

[45] Jiang, L., Nowak, E., Scott, P., Johnson, J., Slaughter, J., Sun, J., and Dave, R. *Physical Review B* **69**(5), 054407 (2004)

Quantitatively, this noise amplitude can be described using Hooge parameter α_H [46]:

[46] Hooge, F. N. *Physica B+C*, **83**, 14 (1976)

$$\alpha_H = \frac{Afv_{1/f}}{V^2} \tag{2.23}$$

where, $v_{1/f}$ is the measured power spectrum of 1/f noise, A is the MTJ area and V is the applied bias voltage. Practically, 1/f noise depends mainly on A, the tunnel barrier thickness and magnetic and electric biasing conditions. A detailed discussion of the noise measurement in the MTJs is provided in section 3.4.

Random telegraph noise Another type of noise, typically appearing in the same frequency range as the 1/f noise is RTN . It is mostly visible in the time domain measurements, were random step-like changes are observed. There are two origins of RTN discussed in scientific literature, one caused by a repeated random charge trapping in the tunnel barrier, and the other caused by a fluctuation

RTN - random telegraph noise

of the FL. Magnetic domains or inhomogenous magnetization in the FL can result in a random resistance change of the MTJ and therefore create the RTN spectrum.

High frequency noise Last discussed source of the noise is the STT based oscillations. As mentioned in section 2.2, sufficient current densities below J_c can induce steady state precession of the magnetization. Typically these oscillations lay in a microwave frequency regime, high above the 1/f noise. If these oscillations can induce coherent change in the spin valve resistance, for example in an MTJ due to a TMR effect, according to Eq. 2.5, an electrical signal can be detected.

The trajectory of the FL oscillations can be more or less chaotic. If coherent oscillations can be realized, one should rather discuss a signal generations, rather than noise. The narrower the peak measured or calculated in a frequency spectrum, the closer the signal is to an ideal sine wave. If high enough power can be achieved using STT, a prototype STO device can be designed - a microwave generator based on nano-MTJ, that only needs DC current to operate. This phenomena is presented in section 3.5.

STO - spin torque oscillator

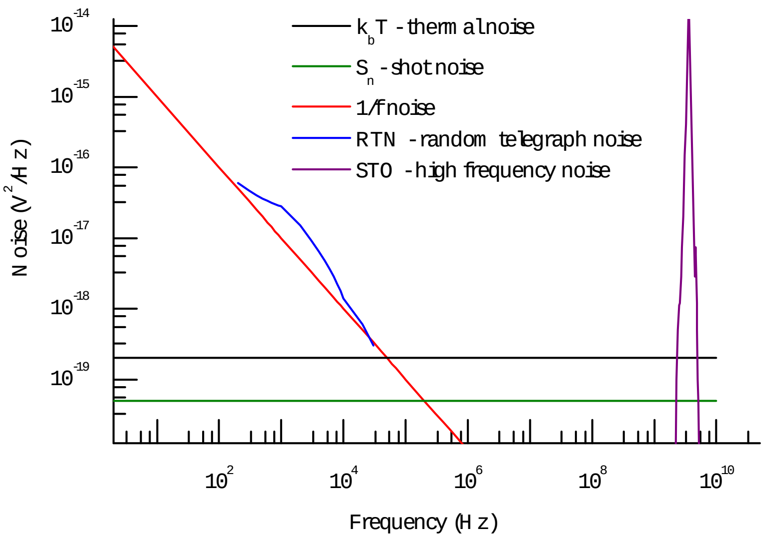

Figure 2.11: Summary of all the discussed noise sources and their frequency dependence. Both thermal and shot noise are frequency independent with white spectra. RTN and 1/f noise appear at lower frequencies, whereas STO can be induced by the STT effect at microwave frequencies.

Figure 2.11 summarizes the spectra of the discussed noises. White noises (the sum of thermal and shot noise) exist in the entire frequency bandwidth and, therefore, are valid for all electronic devices. 1/f noise dominates at lower frequencies below $f < 1$ MHz and is of particular importance for low frequency magnetic field sensors. Spin-torque induced high frequency noise affects the devices operating at the microwave bandwidth. In addition spin-torque devices can be used in microwave electronics.

3
Results and Discussion

This chapter contains the most important results obtained during the PhD process. It begins with the CIMS experiment description performed on the MTJs with a varied thickness of the MgO tunnel barrier. The interesting findings led to further investigation of the properties of junctions using dynamical methods on MTJ wafers. These studies focused on the effective damping and coupling in MTJ samples. Afterwards, a deeper insight into torques and torkances was carried out based on spin-torque diode method. STT parameters were derived for samples with different tunnel barrier thickness, which was supported by the theory. Finally, optimization of the free layer led to a design of the prototype spin torque oscillator that operates without an external magnetic field at high frequency. This studies implied low and high frequency noise measurements. Each section is followed by a discussion.

3.1 Current induced magnetization switching in MTJ with a wedge MgO tunnel barrier

The content of this section is based on work: Skowroński, W., Stobiecki, T., Wrona, J., Rott, K., Thomas, A., Reiss, G., and van Dijken, S. *Journal of Applied Physics* **107**(9), 093917 (2010). The author's contribution on: nanofabrication of samples, magnetic, electric and temperature measurements, data analysis, finite element model simulations, manuscript preparation.

3.1.1 Introduction

As discussed in the chapter 1, nonvolatile and high-density MRAM cell can be based on MTJ operating using STT effect. Switching of the cell state from a low- to high-resistive is realized using CIMS. It has been already presented, that it is possible to switch a nano-MTJ using spin polarized current [1] with a presence of the weak magnetic field. In this section we explored what is the influence of the tunnel barrier thickness t_B on J_c as well as other parameters crucial for the proper operation of the MTJ as a memory unit.

[1] Huai, Y., Albert, F., Nguyen, P., Pakala, M., and Valet, T. *Applied Physics Letters* **84**(16), 3118 (2004)

The theory predicts, according to the Eq. 2.12, that J_c can be reduced by enhancing the spin polarization efficiency η or reducing an effective damping α. Our aim was to perform a CIMS experiments on identical MTJs, but with a different tunnel barrier thickness and derive J_c as well as all other characteristic quantities.

We have demonstrated that MTJs with extremely thin tunnel barriers can be switched with a spin polarized current. Changing the barrier width influences J_c as well as other parameters like the TMR, RA product or the overall coupling.

RA product - resistance area product

3.1.2 *Experimental*

SAF - synthetic antiferromagnet

MTJs with the following multilayer structure : buffer / EB-SAF / $Co_{40}Fe_{40}B_{20}$(2.3) / wedge MgO(0.6 - 1) / $Co_{40}Fe_{40}B_{20}$(2.3) / capping (thickness in nm) was deposited in a Timaris PVD cluster tool system from Singulus Technologies. Details on the deposition process can be found in section 5.1. After the deposition wafer was thoroughly characterized using various methods: CIPT, MOKE and AFM. t_B was calibrated using X-ray reflectivity. Afterwards, the samples were cut into smaller pieces for patterning of MTJ nanopillars with different t_B. Using e-beam lithography, ion beam milling and lift-off, the junctions were patterned into elliptical shapes with the long diameter parallel to the easy magnetization axis. For details about the nanofabrication process see section 5.2. The sizes of the MTJs were 160 × 250, 280 × 430 and 280 × 620 nm^2. Magnetotransport measurement were carried out using the four-point method using the source voltage mode. In order to measure the CIMS curves, a sequences of voltage pulses with different amplitude were applied. The pulse duration length varied from 1 ms up to 500 ms. Throughout the thesis, positive voltage indicates electron tunneling from the bottom RL to the top FL.

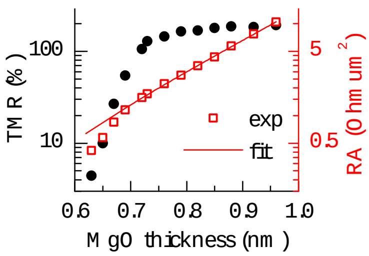

Figure 3.1: TMR and RA product as a function of the MgO barrier thickness measured on unpatterned multilayer stacks using CIPT. The RA product is measured with parallel aligned magnetic moments. The TMR exceeds 150% for MTJs with RA product greater than 3 $\Omega\mu m^2$. Measurement performed at Singulus AG by J. Wrona, before the wafer was delivered to the author for the nanofabrication process.

3.1.3 *Data and analysis*

TMR and RA product Figure 3.1 depicts the TMR and RA product as a function of MgO thickness, measured using the CIPT method on an unpatterned multilayer stack.

For thick MgO barriers down to 0.75 nm, the change of the TMR value is relatively small (from 170% to 150%), indicating good barrier quality and an absence of pinholes, i.e., direct ohmic contact through nanobridges between FL and RL. The RA product increases exponentially with the MgO thickness. When the RA product is reduced to 1.5 $\Omega\mu m^2$ (which corresponds to an MgO thickness of about 0.7 nm) the TMR starts to drop. This can be explained by barrier imperfections which are also reflected by a change of the slope of the RA product vs. MgO thickness curve. Magnetotransport measurements were performed on selected MTJ samples as a function of temperature ranging from 4K up to room temperature.

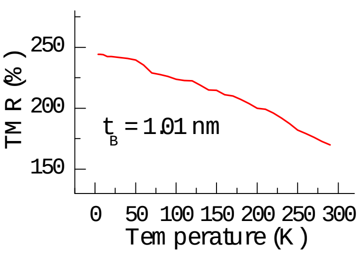

Figure 3.2: TMR ratio as a function of temperature. TMR drops from 250 % at 4K down to 170 at room temperature.

For all investigated t_B resistance of both parallel (P) and antiparallel (AP) magnetization state decreases with increasing temperature, which is a signature of a tunneling character of a charge transport [2]. The TMR ratio measured at lower temperatures reaches 250% (Fig. 3.2). Electrons tunneling through the barrier are scattered by magnons and phonons. Decreased scattering probability as well as thermal smearing affects transport properties and can explain the increased TMR measured at lower temperatures[3].

[2] Ventura, J., Teixeira, J., Araujo, J., Sousa, J., Wiśniowski, P., and Freitas, P. *Physical Review B* **78**(2), 024403 (2008)

[3] Drewello, V., Schmalhorst, J., Thomas, A., and Reiss, G. *Physical Review B* 77(1) (2008)

Coupling Magnetic hysteresis loops of unpatterend multilayer stacks in high (major loop) and low (minor loop) magnetic field were measured using MOKE. Representative results of minor loops for selected MgO barrier thicknesses (0.96, 0.88, 0.82 and 0.71 nm) are presented in Fig. 3.3. Using the CIPT technique, similar

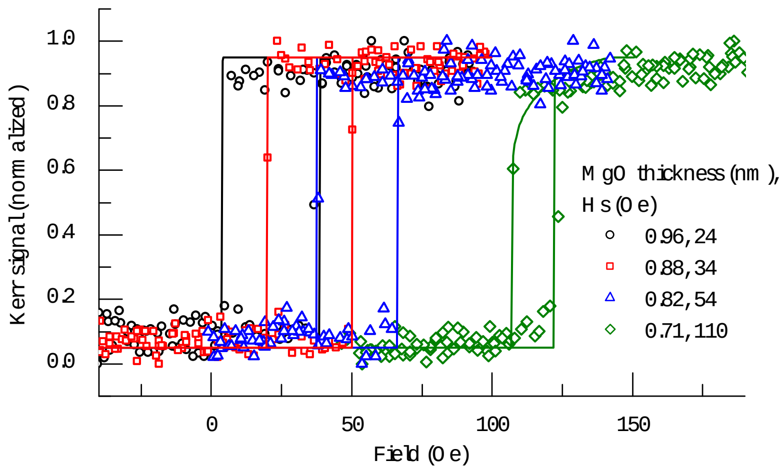

Figure 3.3: Minor MOKE loops of the multilayer stacks with 0.96 nm, 0.88 nm, 0.81 nm and 0.71 nm MgO barriers. Solid lines represent theoretical fits.

results for magnetization reversal in the free layer were obtained. Both measurement techniques clearly show that minor loops are shifted towards the positive field values, which in this case indicates ferromagnetic coupling between the FL and RL of the multilayer stack. The overall coupling energy was calculated using Eq. 2.8. The macrospin simulation results, obtained from the Stoner-Wolfarth model, discussed in section 2.1.4, are shown in Fig. 3.3. It was assumed that the anisotropy energy of the FL and RL: K_{FL} = K_{RL} = 940 J/m^3, the magnetization of the FL and RL: $\mu_0 M_{FL}$ = $\mu_0 M_{RL}$ = 1.35 T and the magnetization of the PL: $\mu_0 M_{PL}$ = 1.6 T. Down to 0.7 nm MgO barrier thickness, the data can be fitted by an exponential function $J_C \propto \exp(-t_B)$. For thinner barriers, however, additional effects due to e.g. pinholes become significant and the dependence of the coupling on the MgO barrier thickness is no longer described by an exponential function.

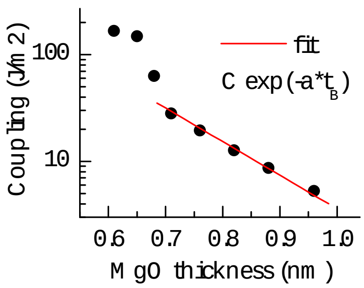

Figure 3.4: Coupling energy between the FL and RL as a function of the MgO tunnel barrier thickness. The data can be fitted using an exponential function down to 0.7 nm thick MgO.

As expected, the exchange coupling energies of other interfaces were found to be independent of barrier thickness. From major magnetic hysteresis loops, the following values were determined: exchange bias energy (PtMn/CoFe) J_{EB} = 0.19 mJ/m^2 and synthetic antiferromagnet (SAF) coupling energy (CoFe/Ru/CoFeB) J_{SAF} = -0.22 mJ/m^2. These values are much larger than the coupling between the FL and the RL and therefore ensure good pining of the bottom CoFeB electrode. Our results on the barrier thickness dependence of IEC contrasts with the experiments by Faure-Vincent et al. [4] and Katayama et al. [5] on epitaxial Fe(001)/wedge MgO(001)/Fe(001) structures, as we did not observe the reported ferro- to antiferromagnetic exchange coupling transition with decreasing MgO barrier thickness. This discrepancy can be partially explained by the existence of dipolar ferromagnetic coupling, named after Néel as the "orange-peel" coupling [6] in sputtered MTJ stacks, due to interface roughness, which might be smaller in epitaxially grown MTJs. Our results, however, cannot be explained by the existence of "orange-peel" coupling alone.

[4] Faure-Vincent, J., Tiusan, C., Bellouard, C., Popova, E., Hehn, M., Montaigne, F., and Schuhl, A. *Physical Review Letters* **89**(10), 107206 (2002)

[5] Katayama, T., Yuasa, S., Velev, J., Zhuravlev, M. Y., Jaswal, S. S., and Tsymbal, E. Y. *Applied Physics Letters* **89**(11), 112503 (2006)

[6] Néel. *Comptes. Rendus* **255**, 1676 (1962)

We estimated the influence of the interface roughness on the overall coupling using Eq. 2.9. The roughness amplitude of the bottom CoFeB electrode after annealing was measured with AFM and did not exceed 0.25 nm. The roughness wavelength in the whole stack originates mainly from the buffer, in our case thick and smooth CuN/Ta. We assume, that both amplitude and wavelength of the roughness do not depend on the MgO barrier thickness.

Varying the roughness amplitude and wavelength of the CoFeB electrode in the range of h = 0.15 - 0.25 nm and λ = 20 - 50 nm, respectively, and assuming the saturation magnetization M_S = 1 MA/m, the maximum value of the Néel coupling energy is 5 μJ/m^2, which corresponds to the shift of the magnetic loop of 25 Oe. This value is much smaller than the loop shift in our measurements and therefore the majority of the shift is attributed to a direct ferromagnetic IEC across the MgO barrier. In order to attribute coupling vs. t_B to "orange-peel" coupling only, the barrier roughness parameters should be h = 1 nm and λ = 1 nm. These values are physically impossible in the MTJ exhibiting tunneling character of transport. Based on *ab initio* calculations of an ideal single crystal Fe(001)/MgO (001)/Fe(001) system, with a similar MgO barrier thickness range, Zhuravlev et al. [7] obtained the ferromagnetic IEC, exponentially decaying with MgO barrier thickness. However, the amplitude of the exchange coupling energy is of two orders of magnitude higher than in our experimental data. They showed, that for junctions containing a variable concentration of oxygen vacancies or localized defect states, it is possible to reduce, or even change the sign of the exchange coupling energy. In our experiment, during an annealing process the B atoms from the CoFeB electrode can diffuse into the MgO barrier [8] (which is not the case in pure Fe electrodes used in the experiments in Refs. [9]), which can, therefore, result in other exchange mechanisms. We believe that our results of ferromagnetic IEC in polycrystalline textured junctions FeCoB (001)/MgO (001)/FeCoB(001) can be understood on the basis of the band calculations of a non ideal single crystal junction.

CIMS Representative TMR loops of the MTJ nanopillars with different MgO barrier thicknesses are shown in Fig. 3.5. The shift of the TMR loops decreased in every case of the different MgO

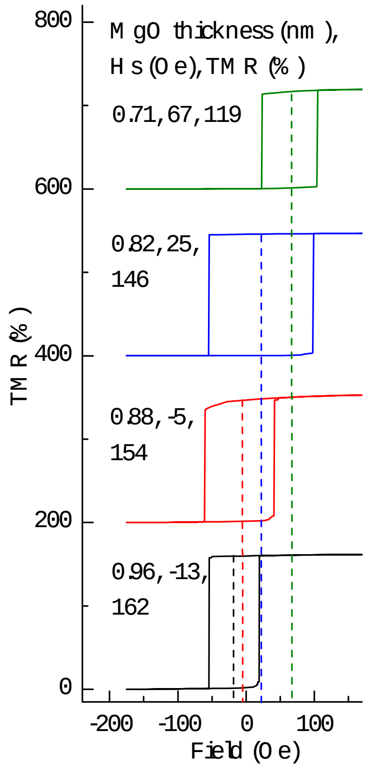

Figure 3.5: TMR minor loops of the MTJ nanopillars with different MgO thicknesses. The TMR loops are less shifted than the loops measured for unpatterned MTJs, because of the magnetostatic coupling influence.

[7] Zhuravlev, M. Y., Velev, J., Vedyayev, A. V., and Tsymbal, E. Y. *Journal of Magnetism and Magnetic Materials* **300**(1), e277 (2006)

[8] Read, J. C., Cha, J. J., Egelhoff, W. F., Tseng, H. W., Huang, P. Y., Li, Y., Muller, D. A., and Buhrman, R. A. *Applied Physics Letters* **94**(11), 112504 (2009)

[9] Faure-Vincent, J., Tiusan, C., Bellouard, C., Popova, E., Hehn, M., Montaigne, F., and Schuhl, A. *Physical Review Letters* **89**(10), 107206 (2002); and Katayama, T., Yuasa, S., Velev, J., Zhuravlev, M. Y., Jaswal, S. S., and Tsymbal, E. Y. *Applied Physics Letters* **89**(11), 112503 (2006)

tunnel barrier thicknesses, in comparison to the unpatterned MTJ stack. The offset field in nanopillars is a result of the competition between ferromagnetic IEC and magnetostatic coupling at the edges of the magnetic layers [10]. In MTJs with sizes of 160 × 250 nm^2, the magnetostatic coupling results in a shift of the TMR loops of 30 - 40 Oe, towards the antiferromagnetic direction (comparison between the offset field in Fig. 3.3 and Fig. 3.5). All MTJs exhibit clear CIMS. Fig. 3.6 presents the voltage pulse duration (t_p) dependence of the critical current density (J_c) for junctions with a 0.96 nm thick MgO tunnel barrier. A typical example of resistance vs. voltage loops measured in an external magnetic field that compensated the total interlayer coupling are presented in Fig. 3.7. According to the theoretical model, J_c can be expressed as in Eq. 2.16. The experimental value of J_{c0} can be obtained by extrapolation of the switching current densities to $\ln(t_P/t_0) = 1$. In our experiment, the results are: $J_{c0}^+ = 6.4 \pm 0.5 \times 10^6$ A/cm^2 for switching from the AP to the parallel P state and $J_{c0}^- = -1.5 \pm 0.2 \times 10^7$ A/cm^2 for switching from P to AP.

[10] Kubota, H., Ando, Y., Miyazaki, T., Reiss, G., Brückl, H., Schepper, W., Wecker, J., and Gieres, G. *Journal of Applied Physics* **94**(3), 2028 (2003)

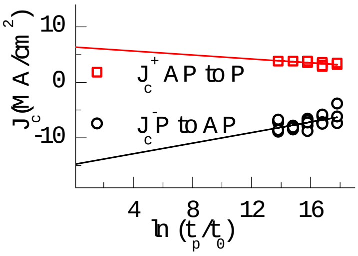

Figure 3.6: The switching current density dependence on the current pulse duration for an MTJ with a 0.96 nm thick MgO tunnel barrier.

Theoretically, the value of the J_{c0} can be estimated using a phenomenological model as expressed in Eq. 2.12. Assuming α = 0.017 (measured on the same samples using PIMM - see section 3.2), $H_K \ll \mu_0 M_S = 2H_D$ = 1.35T, t_F = 2.3 nm and η from Eq. 2.13 and θ = 0° and 180° for switching from the P and AP state respectively, the calculated values are $J_{c0}^+ = 7.7 \times 10^6$ A/cm^2 and $J_{c0}^- = -2.1 \times 10^7$ A/cm^2.

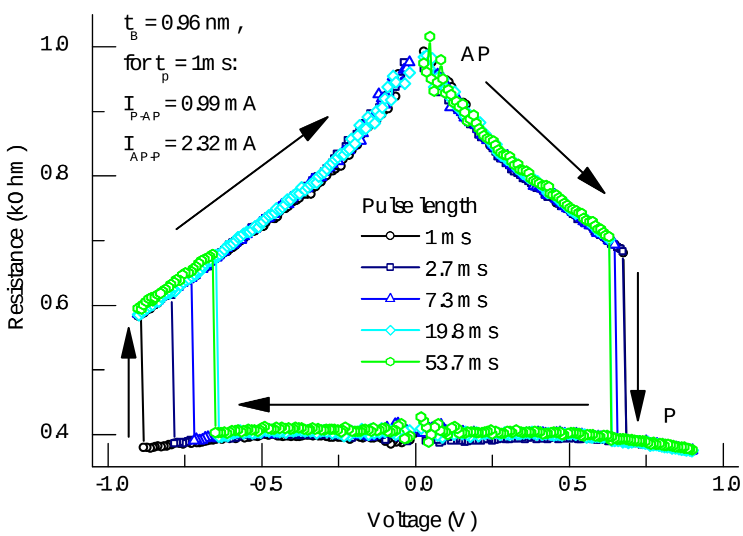

Figure 3.7: Resistance vs. voltage - CIMS loops measured with different voltage pulse duration times of MTJ with t_B = 0.96 nm. According to the model described by Eq. 2.16 switching current (voltage) increases with decreasing pulse length. The resistance was measured on the voltage pulse, therefore a significant decrease of the R_{AP} with V_B is observed. The switching current was calculated according to Ohm's law.

A similar experiment was performed on MTJs with thinner MgO barriers. The results are compiled in Fig. 3.8. The observed increase of the switching current density with decreasing tunnel barrier thickness is mainly explained by a reduction of the spin polarization p [11]. A similar tendency is also indirectly illustrated by the decrease of the TMR in Fig. 3.1. Fig. 3.8 also shows theoretical val-

[11] Itoh, H. *Journal of Physics D: Applied Physics* **40**, 1228 (2007)

ues for J_{c0} that were calculated using Eq. 2.12.

The spin polarization p was calculated from the TMR ratio at low bias voltage using Julliere's formula - Eq. 2.3, whereas the damping was determined from the PIMM. The difference in the asymmetry of the switching current densities between the junctions with a 0.71 nm (small asymmetry) and thicker (large asymmetry) MgO tunnel barrier is explained by a change in the damping constant, which also influences the switching current process. In our experiments, the junctions with a 0.71 nm MgO tunnel barrier exhibited $\alpha = 0.03$ and $\alpha = 0.017$ for the AP and P magnetization state, respectively, whereas junctions with a thicker barrier showed equal damping factors for both states (section 3.2).

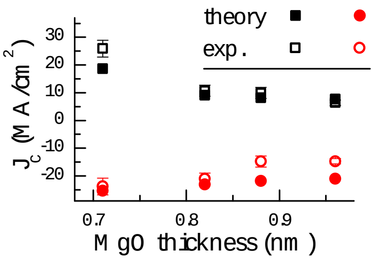

Figure 3.8: The switching current density for MTJs with different MgO barrier thicknesses. Theoretical values were calculated using Eq. 2.12 and TMR and PIMM results

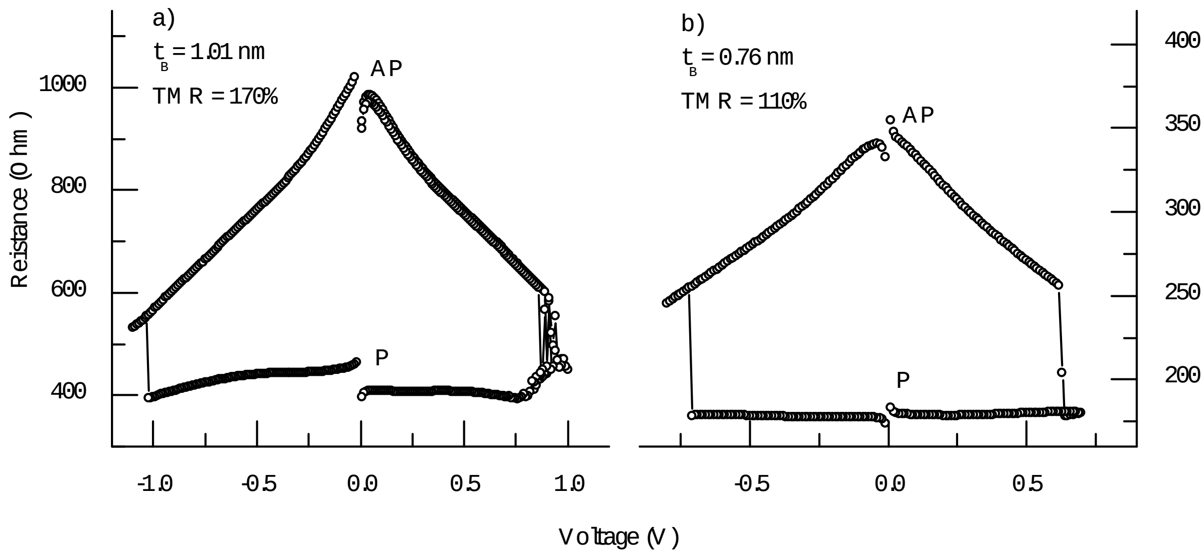

Figure 3.9: CIMS loops measured for the MTJ with thick (t_B = 1.01 nm) and thin (t_B = 0.76 nm) MgO tunnel barriers. Although the I_c increases with decreasing MgO thickness from 1.4 mA for the switching from AP to P state and -2.63 mA for the switching from P to AP state (t_B = 1.01 nm) up to 2.42 mA for the switching from AP to P state and -3.97 mA for the switching from P to AP state (t_B = 0.76 nm), the switching voltage decreases.

Backhopping When the switching current corresponds to a relatively high V_B, the backhopping effect, introduced in section 2.2.3, can be measured. Fig. 3.9 presents CIMS loops measured for the MTJs with 1.01 nm and 0.76 nm thick MgO tunnel barriers. As mentioned above, I_c increases for thinner barriers, however, the switching voltage decreases, due to reduced tunneling resistance of the MTJ. For high V_B in the case of a thick MgO tunnel barrier, the magnitudes of in-plane and perpendicular torques are comparable. In this case, in-plane and perpendicular torques are of opposite polarity and, therefore, the backhopping events are present for the currents that favors switching from AP to P state. For the reverse current polarity, favoring the switching from P to AP state, the backopping is not present, because, in this case, both in-plane and perpendicular torques are of the same sign and both contribute to CIMS. In the case of the MTJ with a thin MgO tunnel barrier, V_B is approximately 70 % smaller. At this voltage, the in-plane torque is greater than the perpendicular torque and contributes mostly to the current induced switching (refer to Fig. 2.10 in section 2.2.3). Therefore, independent of the current polarity, a single backhopping-free switching is measured both for AP to P and for P to AP tranistions. The backhopping effect must be taken into account when designing the MRAM based on CIMS in MTJs[12].

[12] Min, T., Chen, Q., Beach, R., Jan, G., Horng, C., Kula, W., Torng, T., Tong, R., Zhong, T., Tang, D., Wang, P., Chen, M.-m., Sun, J. Z., Debrosse, J. K., Worledge, D. C., Maffitt, T. M., and Gallagher, W. J. *IEEE Transactions on Magnetics* **46**(6), 2322 (2010); and Zhou, Y., Akerman, J., and Sun, J. Z. *Applied Physics Letters* **98**(10), 102501 (2011)

[13] http://www.comsol.com/

Temperature estimation of the MTJ during CIMS In order to estimate the temperature of the MTJ during CIMS events, finite element model simulations using COMSOL[13] software were performed. The calculations were based on an *electrical current* model for voltage and current distribution and *heat transfer in solids* for the temperature estimation. Firstly, the geometry of the MTJ nanopillar was created. The overlap between top and bottom electrode is 2 x 2 μm^2. The pillar has an elliptical cross-section of 150 x 250 nm. The material parameters (electrical conductivity, thermal conductivity etc.) were assumed as the closest to realistic values, based on the data provided by the software manufacturer. Current densities in the MTJ structures were simulated using the *electric currents* mode.

Inside the nanopillar, the obtained current density is $J = 10^{11}$ A/m^2, which is similar to the experimental values. Afterwards, the current density was integrated through one of the electrode's cross-section. The resulting current was at the bias voltage of $V_B = 1$ V was approximately $I = 2.9$ mA, which corresponds to the MTJ resistance of $R = 350\ \Omega$. This value is comparable to the experimental findings for the MTJ with an MgO thickness of $t_B = 0.96$ nm. Finally, the *heat transfer in solids* mode was used, in order to estimate the temperature inside the nanopillar. This mode uses the same currents and voltages to calculate the temperature originating from Joule heating. It was assumed that:

- the bottom surface of the SiO_2 under the bottom lead is at room temperature,
- the top surface of the top lead is subjected to convective cooling with a heat transfer coefficient of $h = 10$ (W/m^2 K),
- each geometry element heats up.

In order to simulate MTJs with a different RA product, the conductivity of the MgO barrier was changed, which resulted in the MTJs resistances changing from approximately $R_P = 350\ \Omega$ down to $R_P = 60\ \Omega$. These values are consistent with the experimental measurements. Simulated temperatures of the MTJs are gathered in Tab. 3.1. In order to compare the MTJ resistance influence on the simulation results, the bias voltage was fixed to $V_B = 0.5$ V.

The maximum temperature in the nanopillar increases with decreasing t_B. For the MTJ with the thinnest measured barrier, it exceeds 413 K. This temperature increase should be taken into account during the design of any device based on CIMS in MTJs with thin tunnel barriers.

t_B (nm)	RA product ($\Omega \mu m^2$)	R_P (Ω)	T_{max} (K)
0.71	1.8	58	413
0.82	3	96	366
0.88	5	150	337
0.96	11	350	313

Table 3.1: Maximum temperature and a temperature gradient across the MgO tunnel barrier calculated using the barrier conductivity which emulates the real MTJs resistance.

3.1.4 Conclusion

In summary, we have investigated the influence of the tunnel barrier thickness on different properties of MTJs. In the unpatterned multilayer stacks the coupling was found to be ferromagnetic for all MgO thicknesses. A decrease in the coupling energy was measured after patterning into nanopillars due to magnetostatic coupling. Within the measured MgO tunnel barrier thickness ranges, all MTJs exhibited CIMS. Measurements on nanopillar junctions with an RA product ranging from 1.8 to 10 $\Omega\mu\text{m}^2$, sizes of 0.03 μm^2, and TMR values of up to 170%, indicated an increase of the switching current density with decreasing tunnel barrier thickness. This effect and the related reduction of switching asymmetry are mainly attributed to a decrease of the tunnel current polarization and a stronger damping in MTJs with very thin MgO barriers.

Additional studies discussed the backhopping events in the MTJs with different thickness of MgO barrier. It was shown that in MTJs with thin tunnel barriers, due to the ferromagnetic coupling between FL and RL, that backhopping is not present, unlike in the MTJs with thicker tunnel barriers, where the ferromagnetic coupling is relatively small. Moreover, for the MTJs with thicker tunnel barriers, CIMS effects occur at higher bias voltage, when the ratio between in-plane and perpendicular torque is smaller than for MTJs with thinner MgO and, therefore, increases the backhopping probability. Additional finite-element model simulations showed, that the temperature in the nanopillar MTJ during CIMS events can exceed 400 K.

3.2 Optimal barrier parameters for spin torque memory application: TMR, coupling, damping

The content of this section is based on work: Serrano-Guisan, S., Skowroński, W., Wrona, J., Liebing, N., Czapkiewicz, M., Stobiecki, T., Reiss, G., and Schumacher, H. W. *Journal of Applied Physics* **110**(2), 023906 (2011). The author's contribution: magnetic measurements, magnetic data analysis, assistance in manuscript preparation.

3.2.1 Introduction

As pointed out in the previous section, the thickness of the MgO tunnel barrier t_B defines crucial parameters of the MTJ, namely the RA product and the spin polarization and hence the TMR ratio. These two parameters are optimal in different tunnel barrier thicknesses, meaning, the TMR is the highest at $t_B > 2$ nm, whereas, the RA product necessary for the CIMS application is achieved for $t_B < 1$ nm. In addition, by reducing the barrier thickness below 1 nm, it was found that for sputtered deposited polycrystalline barriers, due to the defects present in the interfaces, the interactions between electronic band structures of CoFeB electrodes and MgO leads to a ferromagnetic exchange coupling. Finally, this coupling influences the effective damping α of the FL which, according to Eq. 2.12 is directly proportional to J_c, and therefore, it is important for the STT-based devices. In this section, we report on time resolved precessional magnetization dynamic measurements of the MgO based MTJs using PIMM [14]. Using this method, the FL precession frequency f as well as α can be determined (see section 5.3).

[14] Silva, T. J., Lee, C. S., Crawford, T. M., and Rogers, C. T. *Journal of Applied Physics* **85**(11), 7849 (1999)

This inductive measurements, in combination with MOKE measurements, allow us to study the influence of MgO tunnel barrier thickness on important properties of MTJs. Other crucial parameters like the TMR ratio and the RA product can be derived using CIPT methods. Therefore, by using all these methods on an unpatterned sample (on the wafer-level), we are able to determine the optimal barrier thickness range for low current STT-MRAM devices, without needing to use the time-consuming nano-lithography process.

3.2.2 Experimental

For PIMM measurements, similar unpatterned MTJ samples were used as in section 3.1. Inductive characterization was performed on 2×4 mm pieces of lateral dimension, whereas pieces of 5×5 mm were used for magnetooptical characterization. Each sample was cut from the wafer with a wedge shaped MgO tunnel barrier. In regards to the size of the characterized pieces, the variation of t_B can be ignored , because the MgO wedge slope was 0.003 nm/mm, and hence each piece is expected to accurately represent a given MgO tunnel barrier thickness.

Inductive PIMM measurements as well as the magnetooptical measurements were performed at room temperature for all t_B. Details of the PIMM measurement technique used are presented in Ref. [15] and in section 5.3.3. From a single PIMM measurement performed at a given external magnetic field, the precession frequency f and the effective damping α of the FL magnetization is obtained. Fig. 3.10 shows the typical PIMM data in a time domain for t_B = 0.76 nm at three different static field values along the easy magnetization axis. These measurements (open dots in Fig. 3.10) can be accurately simulated by an exponentially damped sin wave (red lines in Fig.) [16], showing that the observed magnetization dynamics are always in the linear regime.

[15] Serrano-Guisan, S., Rott, K., Reiss, G., Langer, J., Ocker, B., and Schumacher, H. *Physical Review Letters* **101**(8) (2008)

[16] We estimate the magnetic field pulses generated by the 40 μm wide coplanar waveguide in the PIMM setup to have an amplitude of about $H_p \sim 2$ Oe and a short pulse length (rise time of 65 ps, fall time of 100 ps, and a duration of 200 ps at half maximum), which results in the excursion of FL magnetization out of equilibrium to be relatively small. At these conditions the solution to the Landau-Lifshitz-Gilbert equation is an exponential damped sine wave

The data are fitted to an exponentially damped sine wave with the following formula:

$$s = C \sin(2\pi f t + \phi)\, e^{-t/\tau_C} \tag{3.1}$$

where s is the measured PIMM signal in a time domain t, C is the relative amplitude, the ϕ is a initial phase and τ_C is the decay constant, which is inversely proportional to the damping factor α:

$$\alpha = \frac{2}{\gamma \tau_C \mu_0 M_S} \tag{3.2}$$

It is clear from experimental data that f varies with the applied static field. This field dependence of the FL precession frequency is plotted in Fig. 3.11 (open dots). In order to derive the material parameters from Fig. 3.11, like the anisotropy constant K_{FL} and the FL coupling J_{FL}, we model the precession of the FL of the MTJ multilayer system using a macro-spin model of a coupled trilayer stack consisting of the FL, RL and PL, similar to the one presented in section 2.1.4. A 2.3 nm thick FL with a uniaxial anisotropy energy K_{FL}, and an overall coupling between the FL and the RL of J_{FL} was assumed. Zero net magnetic moment of the RL and PL is assumed due to a strong antiferromagnetic exchange coupling between both layers.

Using this system, the total energy, based on the general approach discussed in section 2, can be expressed as:

$$E = -\mu_0 M_{FL} H \cos\theta \cos\phi - \left(\frac{1}{2}\mu_0 M_{FL} E_D + K_{FL}\right)\cos^2\theta - \frac{J_{FL}}{t_{FL}}\cos\theta\cos\phi \tag{3.3}$$

where (θ, ϕ) are the polar coordinates of the FL magnetization and E_D is the demagnetization energy: $E_D = NM_{FL}$, where N is the demagnetizing tensor. Assuming also that the magnetic field is applied in the sample plane and along the easy magnetization axis, the formula can be rewritten as:

$$E = -\mu_0 M_{FL} H \cos\theta - K_{FL}\cos^2\theta - \frac{J_{FL}}{t_{FL}}\cos\theta \tag{3.4}$$

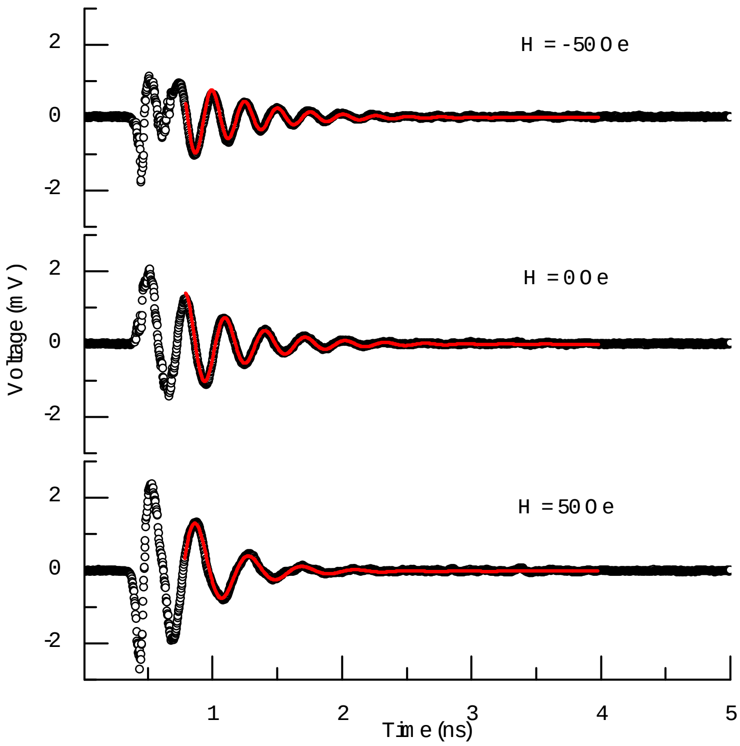

Figure 3.10: PIMM data (open dots) for t_B = 0.76 nm measured with a different magnetic field applied along the easy magnetization axis. Lines show fits using an exponentially damped sinusoid.

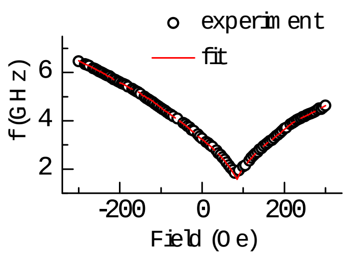

Figure 3.11: Magnetic field dependence of the precession frequency derived from PIMM measurements (open dots) of a sample with t_B = 0.76 nm. The solid line shows the dispersion relation of a Stoner-Wolfarth single-domain model with H_K = 18 Oe and J_{FL} = 20.1 μJ/m^2 - data derived from the MOKE measurement.

Following a method presented in Ref. [17], in order to derive the dispersion relation, one needs to calculate the root of the following matrix:

$$\begin{pmatrix} E_{\theta\theta} & E_{\theta\phi} - iZ \\ E_{\theta\phi} + iZ & E_{\phi\phi} \end{pmatrix} \tag{3.5}$$

where $E_{\theta\theta} = \frac{\partial^2 E}{\partial\theta^2}$, $E_{\theta\phi} = \frac{\partial^2 E}{\partial\theta\partial\phi}$, $E_{\phi\phi} = \frac{\partial^2 E}{\partial\phi^2}$, and $Z = \left(\frac{\omega}{\gamma}\right) M \sin\theta$. From this relation, if we consider just the magnetization dynamics of a single layer we obtain the well-known expression:

$$\left(\frac{\omega}{\gamma}^2\right) = \frac{1}{M^2 \sin^2\theta}\left(\frac{\partial^2 E}{\partial\theta^2}\frac{\partial^2 E}{\partial\phi^2} - \frac{\partial^2 E}{\partial\theta\partial\phi}\right) \tag{3.6}$$

Calculating terms in Eq. 3.6 from Eq. 3.4, we obtain the following formula for f:

$$f = \frac{\gamma\mu_0}{2\pi}\sqrt{(H_s\cos\theta + H_k\cos 2\theta + H\cos\theta)\,(H_s\cos\theta + H_k\cos^2\theta + H\cos\theta + M)} \tag{3.7}$$

where $H_s = \frac{J_{FL}}{t_{FL}\mu_0 M_s}$, $H_k = \frac{2K_{FL}}{\mu_0 M_s}$ and θ is obtained by minimizing the energy term:

$$\mu_0 M_s H\sin\theta + K_{FL}\sin 2\theta + \frac{J_{FL}}{t_{FL}}\sin\theta = 0 \tag{3.8}$$

Eq. 3.7 is a specific example of Eq. 2.19 derived in the section 2.2.3.

Using Eq. 3.7 it is possible to fit the dependence of f on the applied magnetic field, as shown in Fig. 3.11. In addition, this procedure in combination with the Stoner-Wolfarth model fitting enables

[17] Rodriguez-Suárez, R., Rezende, S., and Azevedo, A. *Physical Review B* **71**(22), 224406 (2005)

the derivation of the magnetic multilayer system parameters like M_s, H_k and J_{FL}.

3.2.3 Data and analysis

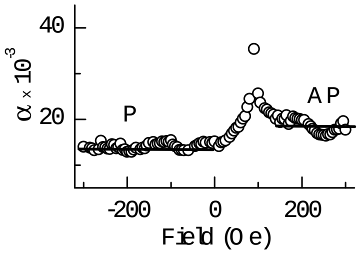

Figure 3.12: The effective damping α dependence on an in-plane magnetic field applied along an easy magnetization axis. α was derived from PIMM signals from a sample with t_B = 0.76 nm, similar to the ones presented in Fig. 3.10. The average α measured at AP state is higher that the one for P state - the lines are a guide for the eye.

Fig. 3.12 presents α derived from a series of measurements similar to the one presented in Fig. 3.10 for a sample with t_B = 0.76 nm. The effective damping is approximately constant at stable P (H = - 300 Oe) and AP (H = 300 Oe), whereas close to the FL switching field it increases slightly. A set of similar curves measured for the MTJs with a different t_B is presented in Fig. 3.13. Clearly, α measured for the P and AP states changes with the tunnel barrier thickness. Three typical α behaviors can be distinguished at different t_B ranges. For the MTJs with $t_B > 0.76$ nm, α is independent on the magnetization state, i.e., P or AP. It was found, that $\alpha = 0.016 \pm 0.003$, which is comparable to the value obtained for a single CoFeB layer. This implies that for $t_B > 0.76$ nm the influence of neighboring layers of the MTJ stack on the FL magnetization dynamics is negligible, and therefore, the observed α seems to be dominated by the intrinsic properties of the CoFeB layer.

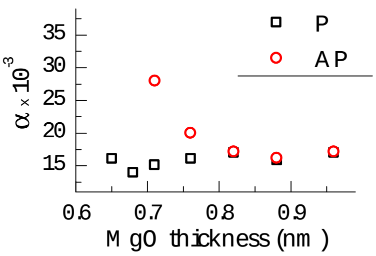

Figure 3.13: Tunnel barrier thickness, dependence of the effective damping measured for the P and AP magnetization states of the MTJs.

The dynamic properties of measured MTJs for two different tunnel barrier thicknesses is presented in Fig. 3.14. For t_B = 0.88 nm, the static external magnetic field dependence of the precession frequency f (Fig. 3.14a), α (Fig. 3.14b) and the calculated FL, RL and PL magnetization orientation for the magnetic fields along the easy axis (Fig. 3.14c) and along the hard axis (Fig. 3.14d) are shown. A macrospin model for three ferromagnetic layers with the additional antiferromagnet (similar to the one presented in section 2.1.4) was used to calculate the data obtained from the measurement. The RL is the upper CoFeB layer of the SAF, and the PL refers to the CoFe layer of the SAF, which is exchange coupled to the PtMn antiferromagnetic layer (for details see section 2.1.4).

For this type of tunnel barrier thickness the FL magnetization reversal of the MTJ stack is similar to an uncoupled ferromagnetic layer (also similar to a single ferromagnetic layer case), where the PL and the RL always stay along an easy magnetization axis, while only the FL is reversed. Although a very small ferromagnetic coupling between FL and RL is present, which as a main consequence shifts the magnetization loop and the resonance frequency f. This is caused by an extra effective bias field along the easy axis induced by the IEC. Such behavior was also measured for all MTJ with $t_B >$ 0.76 nm. In all these cases the FL magnetization dynamics is similar to the single uncoupled ferromagnetic layer. The dependence of α vs. magnetic field is symmetric and shows an enhancement at low fields due to inhomogeneous line broadening near FL switching [18]. This result is of particular importance for STT-MRAM applications as the critical current density J_c in the CIMS process is directly proportional to α of the FL. Hence, an additional dissipation of the STT-based precession, for example, by coupling of the FL to the RL

[18] Silva, T. J., Lee, C. S., Crawford, T. M., and Rogers, C. T. *Journal of Applied Physics* **85**(11), 7849 (1999)

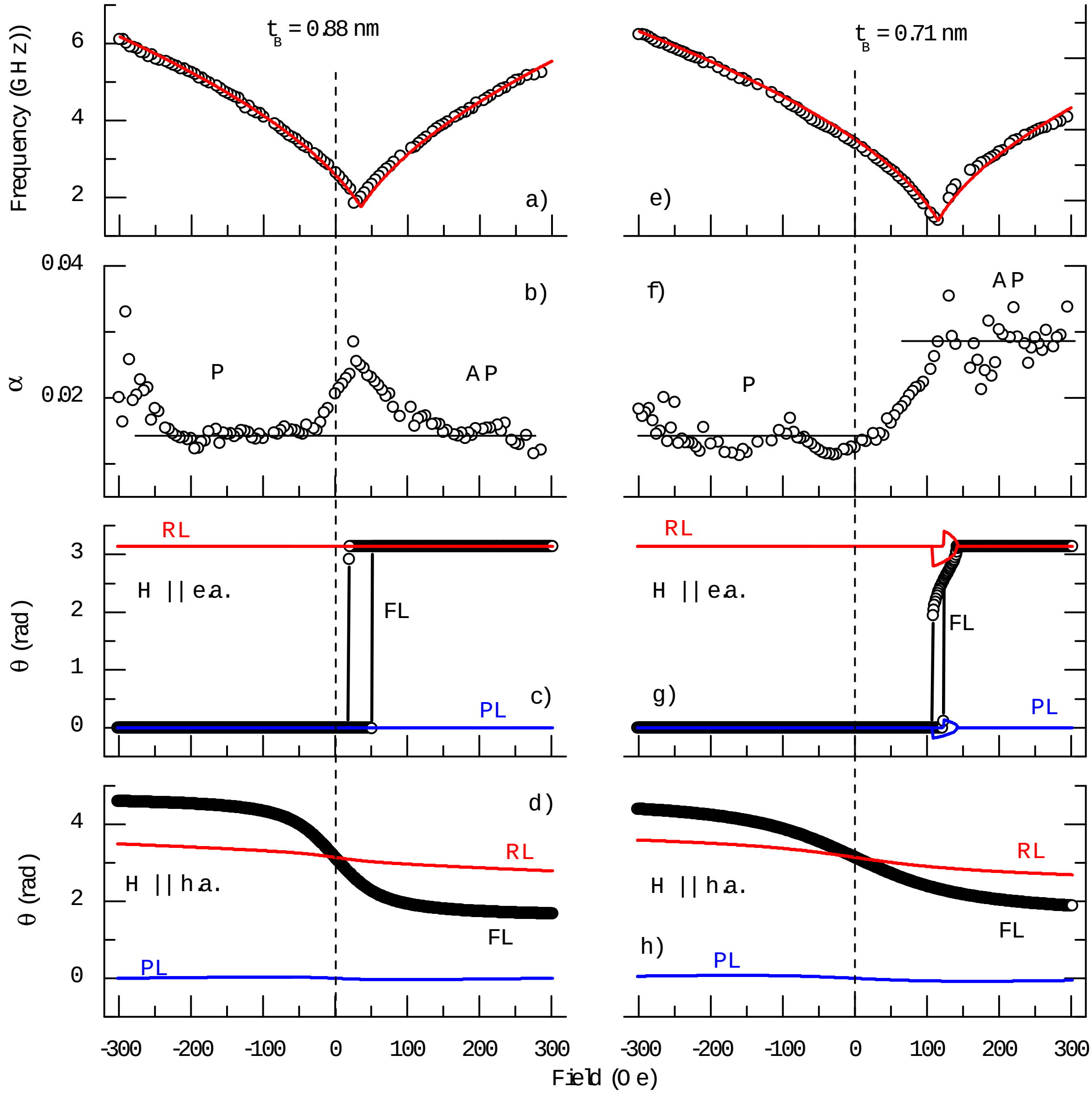

Figure 3.14: (a), (e) Dispersion relation (b), (f) effective damping α dependence on easy axis magnetic fields; and (c d), (g - h) simulated magnetic field dependence of magnetization orientation of each ferromagnetic layer for (c), (f) easy axis (e.a.) and (d), (h) hard axis (h.a.) magnetic fields with t_B = 0.88 nm [(a), (b), (c), and (d)] and t_B = 0.71 nm [(e), (f), (g) and (h)]. (a), (e) Open dots (line) show the measured (simulated) resonance frequency.

layer, would also increase J_c thereby hampering the STT-MRAM cell feature.

For intermediate tunnel barrier thickness (0.68 nm < t_B < 0.76 nm), α becomes asymmetric with respect to the magnetic field and a different effective damping parameter is measured for P and AP configurations ($\alpha_{AP} > \alpha_P$). This tendency is depicted in Fig. 3.12. Note that this difference in α was taken into account when calculating J_{c0} in section 3.1. This difference between α_{AP} and α_P increases with decreasing t_B until, for barrier thickness below $t_B \leq$ 0.68 nm, only a damped oscillatory signal could be observed at P configurations only.

Figure 3.14e-h shows the magnetic field dependence of the precession frequency f (Fig. 3.14e), the effective damping α (Fig. 3.14f) and the FL, RL and PL magnetization orientation for the magnetic fields along both the easy (Fig. 3.14g) and along the hard magnetization axis (Fig. 3.14h) for the MTJ with t_B = 0.71 nm. Except for the reversal process itself, the angular magnetization configurations of the FL, RL and PL are similar to those with t_B = 0.88 nm, as depicted in Fig. 3.14g. However, in spite of this similarity, much larger α is observed when the FL magnetization is in the AP state ($\alpha_{AP} \sim 0.028 \pm 0.004$) than for P configurations ($\alpha_P \sim 0.015 \pm 0.003$). This is the signature that our macrospin model used to derive f and α is not sufficient to model a complete description of the magnetization dynamics of our system for such thin tunnel barriers. Indeed, although the frequency vs. magnetic field spectra can be well fitted by this approximation, a further analysis must be done in order to understand the asymmetry in α. An intuitive explanation for this could be done using the "orange-peel" effect. As mentioned in section 2.1.5, the Néel dipolar coupling resulting from the multilayers roughness, favors parallel alignment of the FL and RL magnetizations. This roughness leads to significant fluctuating coupling fields close to the interface of both ferromagnets which, in turn, will induce a local distribution of the magnetization. For thin MgO barriers, this coupling will be strong enough to rotate the magnetic moments of the FL close to the interface parallel to the RL, so that monolayers closer to the CoFeB/MgO interface in the FL have magnetization that is always parallel to the RL. In addition to the Néel coupling, in MTJs with thin tunnel barriers, interlayer exchange coupling can dominate the overall coupling. This mechanism also contributes to the inhomogeneous precession in the FL as is explained in detail in section 3.3.

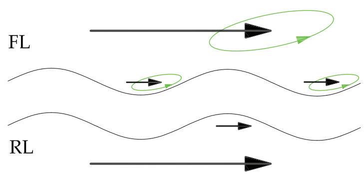

Figure 3.15: Toy picture of the cross-sectional MTJ trilayer magnetization profile at parallel state. The entire volume of the FL is aligned parallel to the RL.

Thus, due to this ferromagnetic coupling, for P configuration of the MTJ, these local moments will be almost parallel to the RL magnetization, and therefore, the effect of the roughness on the magnetization dynamics as well as the interlayer exchange coupling should not be important, thereby being tunnel barrier thickness independent, as observed in our experimental data. This situation is depicted in Fig. 3.15.

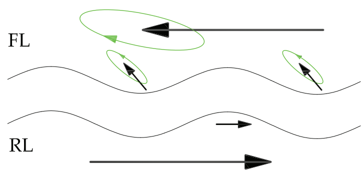

Figure 3.16: Toy picture of the cross-sectional MTJ trilayer magnetization profile at antiparallel state. The Néel coupling induces a ferromagnetic coupling between the RL and the magnetic moments located at the valleys of the rough FL. For the MgO barriers which are thin enough ,this coupling is so strong that these magnetic moments tend to be always aligned along the RL magnetization. The magnetization in the valleys is parallel whereas the rest of the FL is antiparallel to the RL, resulting in inhomogenous magnetization of the precessing layer.

For AP configurations however, strong inhomogeneous magnetostatic fields are developed in the FL. In these conditions, almost all the magnetic moments of the FL are reversed, but some of them, located close to the MgO interface are still influenced by the magnetization of the RL - Fig. 3.16. As the way the magnetization relaxes towards equilibrium is very sensitive to the details of the microscopic interactions, this large magnetic inhomogeneity will lead to an inhomogeneous precessions and hence to an increase of α. The Néel coupling increases when t_B decreases (see Eq. 2.9 in section 2.1.5), this asymmetry in α will be larger for MTJs with thinner tunnel barriers, as measured in our experiments.

Finally, for the MTJs with $t_B \leq 0.68$ nm, the FL magnetization precession is measured only at P configurations. At this thickness range $J_{FL} \sim 180\ \mu\mathrm{J/m}^2$ is of the same order of magnitude as the other couplings in the system: the antiferromagnetic exchange coupling between the RL and the PL ($J_{SAF} \sim$ -221 μJ/m^2) as well as the exchange bias coupling between the PL and antiferromagnet ($J_{EB} \sim$ 188 μJ/m^{2}2). This implies that all ferromagnetic layers of the MTJ stack are strongly coupled, which leads to a scissored state of the SAF layers when the FL magnetization is being reversed. Consequently, at these conditions the whole system is involved in precessional magnetization dynamics and PIMM data can no longer be analyzed by Eq. 3.7. Furthermore, for this MgO tunnel barrier thickness range, the magnetic hysteresis loop is closed and the FL magnetization reversal process is very different from the uncoupled FL. This behavior therefore imposes, a minimum tunnel barrier thickness ($t_B \leq$ 0.68 nm for this particular technology) that must be considered in order to ensure the existence of a bistable state suitable for the STT-MRAM applications.

3.2.4 Conclusion

The magneto-transport measurements presented in section 3.1 showed that J_c exhibits similar barrier thickness dependence as the effective damping parameter to that derived from PIMM measurements. It was shown that for thin tunnel barriers (t_B < 0.76 nm) the evolution of the J_c for AP to P switching is similar the switching from P to AP, which contradicts with Eq 2.12 (if constant α is assumed). This behavior cannot be ascribed to a different polarization factor on Slonczewski's expression of J_c [19], due to the different orientation of the FL magnetization with respect to the RL. However, this effect could be a consequence of the different damping parameters α for P and AP configurations as observed in the PIMM measurements. These results imply that, owing to the close relationship between J_c and the α, inductive measurements in combination with magneto-optical measurements are an excellent tool to investigate the STT-MRAM key parameter J_c without time consuming lithographic processes for patterning MTJ nanopillars and hence derive the optimum tunnel barrier thickness range for efficient STT-MRAM devices.

[19] Sun, J. J. and Freitas, P. P. *Journal of Applied Physics* **85**, 5264 (1999)

3.3 Direct measurements of the spin transfer torque using ST-FMR

The content of this section is based on work: Skowroński W., Czapkieiwcz M., Frankowski M., Wrona J., Stobiecki T., Reiss G., Chalapat K., Paraoanu G. and van Dijken S., *arXiv*:1301.7186. The author's contribution: samples nanofabrication, static and dynamic electric measurements, macrospin simulations, data analysis, manuscript preparation.

3.3.1 Introduction

As introduced in the previous sections, high density magnetic random access memories can be implemented based on MTJs that take advantage of the CIMS effect, [20] which is caused by interactions between spin-polarized current and the magnetization of the FL tunnel junction cell. This phenomenon is caused by the STT effect[21]. In order to optimize MTJ parameters so that they can compete with existing memory and microwave technologies, a deeper insight into STT physics is necessary. The spin-torque diode effect, discovered for the first time by Tulapurkar et al. [22], enables quantitative measurements of STT parameters with respect to the bias voltage [23].

[20] Huai, Y., Albert, F., Nguyen, P., Pakala, M., and Valet, T. *Applied Physics Letters* **84**(16), 3118 (2004)

[21] Berger, L. *Physical Review B* **54**(13), 9353 (1996); and Slonczewski, J. C. *Journal of Magnetism and Magnetic Materials* **159**(1-2), L1 (1996)

[22] Tulapurkar, A. A., Suzuki, Y., Fukushima, A., Kubota, H., Maehara, H., Tsunekawa, K., Djayaprawira, D. D., Watanabe, N., and Yuasa, S. *Nature* **438**(7066), 339 (2005)

[23] Sankey, J. C., Cui, Y., Sun, J. Z., Slonczewski, J. C., Buhrman, R. A., and Ralph, D. C. *Nature Physics* **4**(1), 67 (2007); and Kubota, H., Fukushima, A., Yakushiji, K., Nagahama, T., Yuasa, S., Ando, K., Maehara, H., Nagamine, Y., Tsunekawa, K., Djayaprawira, D. D., Watanabe, N., and Suzuki, Y. *Nature Physics* **4**(1), 37 (2007)

In this section, we use the spin-torque diode effect to investigate the dependence of in-plane and perpendicular spin torques on MgO tunnel barrier thickness. The tunnel barrier determines the transport properties of the device, as it affects the tunneling magnetoresistance (TMR) ratio, the resistance area (RA) product and the coupling between the FL and the reference layer (RL). We show that the spin-torque ferromagnetic resonance (ST-FMR) spectra contain a double resonance mode for very thin MgO barriers due to strong ferromagnetic interlayer coupling. Moreover, the in-plane and perpendicular spin-torques do not depend on MgO barrier thickness, in agreement with free electron models presented in section 2.2.3.

3.3.2 Experimental

For these studies, a similar MTJ stack was used as in section 3.1. After the deposition, three different parts of the sample were selected for patterning into nanometer size pillars (later in this section referred to as S1, S2 and S3, see Table 3.2 for details). Using a three-steps electron beam lithography process, which included ion beam milling, lift-off and oxide deposition steps, nanopillars with an elliptical cross-section of 230 × 130 nm were fabricated. The pillars were etched down to the PtMn layer. To ensure good RF performance of the device, the overlap between the top and bottom leads was about 4 μm^2, which resulted in a capacitance of less than 1 × 10^{-14} F. Each set of MTJs with a constant MgO tunnel barrier consisted of 10 - 15 nanopillars.

No.	t_B (nm)	TMR (%)	RA ($\Omega\mu$m^2)	Hs (Oe)
S1	1.01	170	9.6	-21.7
S2	0.95	165	6.24	-3.7
S3	0.76	110	2.86	47

Table 3.2: Summary of the static parameters of the prepared MTJ nanopillars.

ST-FMR measurements were conducted in a frequency range of 2 - 12 GHz. In these experiments, the application of an RF current to an MTJ generated a DC voltage (also called mixing voltage - V_{mix}) across the device when the current frequency was brought into resonance with the resistance oscillations, arising from the STT. Details of the measurement setups are presented in section 5.3.2. The MTJs were placed in a magnetic field at an angle of $\beta = 70^\circ$ with respect to the easy magnetization axis (except for the case presented in Fig. 3.18(b)), so that a large variety of angles θ between the junction's FL and RL could be obtained. We estimated θ from Eq. 2.5.

In order to obtain the clearest STT results, we kept θ fixed at 90° [24]. The magnitude of the RF input signal, connected to the MTJ through the capacitive lead of a bias tee, was fixed at -15 dBm. This resulted in an RF current (I_{RF}) between 5 μA and 25 μA, depending on the sample resistance. I_{RF} was calculated on the basis of the non-resonant background signal, using a model proposed in Ref. [25]. The bias voltage was fed through the inductive lead of the bias tee. V_{mix} was measured using an AC coupled lock-in amplifier, which was synchronized with the amplitude modulated signal from the RF generator. In this paper, positive bias voltage indicates electron transport from the bottom RL to the top FL.

[24] Wang, C., Cui, Y., Sun, J., Katine, J., Buhrman, R., and Ralph, D. *Physical Review B* **79**(22), 224416 (2009)

[25] Sankey, J. C., Cui, Y., Sun, J. Z., Slonczewski, J. C., Buhrman, R. A., and Ralph, D. C. *Nature Physics* **4**(1), 67 (2007)

3.3.3 *Data and analysis*

Table 3.2 summarizes the tunneling magnetoresistance (TMR), the resistance-area (RA) product and the static offset magnetic field (H_S) for three sets of MTJs with different MgO barrier thickness. The high TMR ratio of 170% for a 1.01 nm barrier and the exponentially decreasing RA product with decreasing MgO thickness confirm the good quality of the MgO barrier. Similar TMR ratios and RA products were measured on full wafers using a current in-plane tunneling (CIPT) technique before patterning[26]. H_S is shifted approximately 30 - 40 Oe with respect to the wafer-level measurements, indicating the existence of dipolar magnetostatic coupling due to stray field interactions in the nanopillar junction. For the MTJ with a 1.01 nm thick tunnel barrier, antiferromagnetic stray-field coupling dominates the interaction between FL and RL (H_S = -21.7 Oe). A reduction of the barrier thickness to 0.76 nm reverses the sign of the offset field (H_S = 47 Oe). In this case, the FL and RL couple ferromagnetically due to direct interactions across the thin tunnel barrier with RL.

[26] Wrona, J., Langer, J., Ocker, B., Maass, W., Kanak, J., Stobiecki, T., and Powroźnik, W. *Journal of Physics: Conference Series* **200**, 052032 (2010)

3.3.4 *ST-FMR*

Typical ST-FMR signals (without DC bias voltage) for samples S1 - S3 are presented in Fig. 3.17. We note that a single symmetric peak is measured for sample S2 in a wide magnetic field range. For this sample, the coupling between FL and RL is negligible. Moreover, the monotonic increase of the resonance frequency with applied

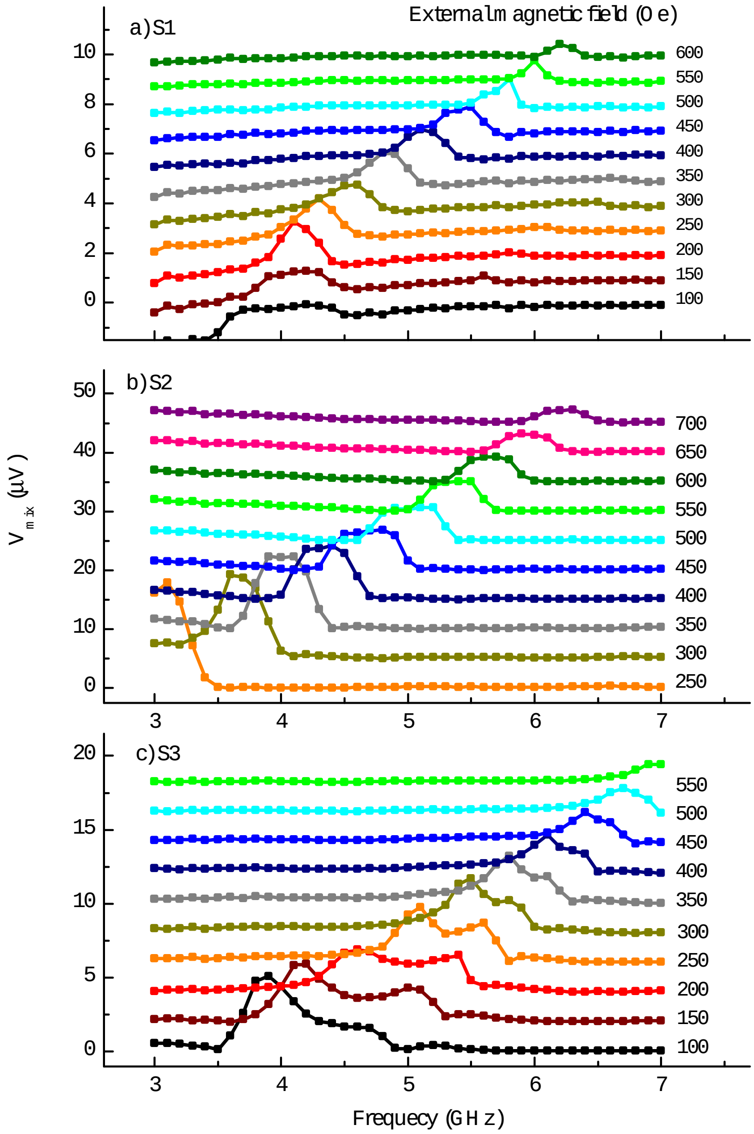

Figure 3.17: ST-FMR spectra of samples S1 (a), S2 (b) and S3 (c) measured with various magnetic field applied at an angle of β = 70° with respect to the easy magnetization axis. Only the RF signal (without DC bias voltage) was supplied to the MTJ. For sample S3 (c) two closely spaced peaks are visible.

magnetic field indicates that the FMR signal originates from magnetization precession in the FL [27]. A similar behavior is observed for sample S1, wherein the effective coupling between FL and RL is weakly antiferromagnetic. However, for sample S3, which is characterized by strong ferromagnetic coupling between FL and RL, an additional peak is measured. The origin of this double resonance mode is not entirely clear. In previous publications, it has been attributed to domain formation in the FL [28], higher-order spin wave excitations [29] and magnetization precession in other layers of spin-valve MTJs [30]. To analyze the double resonance mode in sample S3 in more detail, we performed macrospin simulations using the model presented in section 2.1.4. This model, based on the Stoner-Wolfarth approach, assumes coherent rotation of the FL and RL magnetization. By minimizing the system energy we find the angle of the FL and RL magnetizations with respect to the easy axis and on this basis, we calculate the dispersion relation. The simulated dispersion relations that are obtained for $\beta = 70°$ and for $\beta = 30°$ are presented in Fig. 3.18 together with the measured ST-FMR spectra. For $\beta = 30°$, the experimental and simulated FMR modes of the FL and RL are in good quantitative agreement. We note that the FMR signal of the RL is only measured when a large positive magnetic field is applied to the nanopillar junctions. The resonance frequency of the RL decreases with increasing field strength in this field range. The frequency of the double resonance peak in the spectra for $\beta = 70°$ (Fig. 3.18(a)), on the other hand, increase with applied field strength. The experimental dispersion relations now closely match simulated curve. Based on this analysis, we attribute the double resonance mode to inhomogeneous magnetization precession in the FL rather than FMR in the RL or any other magnetic layer of the MTJ stack and is caused by the strong interlayer exchange coupling between FL and RL.

[27] Cornelissen, S., Bianchini, L., Devolder, T., Kim, J., Roy, W. V., Lagae, L., and Chappert, C. *Physical Review B* **81**(14), 144408 (2010)

[28] Lee, K., Deac, A., Redon, O., Noziéres, J., and Dieny, B. *Nature Materials* **3**(12), 877 (2004)

[29] Helmer, A., Cornelissen, S., Devolder, T., Kim, J. V., van Roy, W., Lagae, L., and Chappert, C. *Physical Review B* **81**(9), 94416 (2010)

[30] Sankey, J., Braganca, P., Garcia, A., Krivorotov, I., Buhrman, R., and Ralph, D. *Physical Review Letters* **96**(22) (2006)

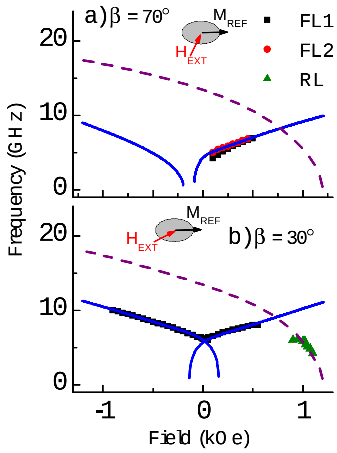

Figure 3.18: The dispersion relation of sample S3 measured with the magnetic field applied at angle $\beta = 70°$ (a) and $\beta = 30°$ (b) with respect to the easy magnetization axis. The solid (dashed) line represents a macrospin simulation result calculated for the FL (RL). (a), both modes (FL1 and FL2) increases its resonant frequency with increasing magnetic field, which is attributed to the FL magnetization precession. (b) both FL and RL magnetizations precession were measured at a range of the magnetic field applied. The macrospin simulations were performed according to the model presented in section 2.1.4, with the parameters listed in section 3.1, with the FL anisotropy energy changed from $K_{FL} = 7$ kJ/m^2.

3.3.5 *Torques and torkances*

In order to obtain the STT components, i.e., in-plane torque $\tau_{\|}$ and perpendicular torque $\tau_{\perp}$, from the ST-FMR measurements, we used the model presented in Ref. [31]. Here, we assume a simplified formula for V_{mix}:

$$V_{\text{mix}} = \frac{1}{4}\frac{\partial^2 V}{\partial I^2} I_{\text{RF}}^2 + \frac{1}{2}\frac{\partial^2 V}{\partial I \partial\theta}\frac{\hbar\gamma\sin\theta}{4eM_S Vol\sigma} I_{\text{RF}}^2[\xi_{\|}S(\omega) - \xi_{\perp}\Omega A(\omega)], \quad (3.9)$$

where $\hbar$ is the reduced Planck's constant, γ is the gyromagnetic ratio, e is the electron charge, Vol is the volume of the FL, M_S is the saturation magnetization of the FL, σ is the linewidth, $\xi_{\|} = 2(e/\hbar\sin\theta)(dV/dI)d\tau_{\|}/dV$ and $\xi_{\perp} = 2(e/\hbar\sin\theta)(dV/dI)d\tau_{\perp}/dV$ are the magnitudes of the symmetric $S(\omega)=[1+(\omega-\omega_m)^2/\sigma^2]^{-1}$ and asymmetric $A(\omega)=[(\omega-\omega_m)/\sigma]S(\omega)$ lorentzians components, and $\Omega_{\perp}=\gamma N_x M_{\text{eff}}/\omega_m$, $N_x=4\pi+(H_z-H_a\sin^2\beta)/M_{\text{eff}}$, where ω_m is the resonant frequency, H_z is the sum of the applied external magnetic

[31] Wang, C., Cui, Y., Sun, J., Katine, J., Buhrman, R., and Ralph, D. *Physical Review B* **79**(22), 224416 (2009)

field and the offset field acting on the precessing FL, H_a is the in-plane anisotropy field of the FL and $4\pi M_{\mathrm{eff}}$ is the effective out-of-plane anisotropy of the FL. We neglected the terms (2c) - (2g) of Ref. [32] because in our case $\theta \approx 90^\circ$.

[32] Wang, C., Cui, Y., Sun, J., Katine, J., Buhrman, R., and Ralph, D. *Physical Review B* **79**(22), 224416 (2009)

The magnetic field acting on the FL (H_z) which is the sum of the external magnetic field and the dipole field ($H_d \approx 100$ Oe) is roughly $H_z \approx 400$ Oe, which is much smaller than M_s and, therefore, $N_x \approx 4\pi$. In order to properly analyze the measurement data, we subtracted the non-resonant background signal from each ST-FMR data set. The background signal V_{bckg} is the ST-FMR spectra measured in similar conditions, however, with a much higher magnetic field that suppress the magnetization precession at a given frequency. This background signal is also used for the estimation of I_{RF}. According to the Eq. 3.9 when no precession in the FL exist, I_{RF} can be calculated from the following formula:

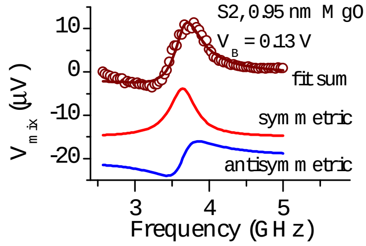

Figure 3.19: An example of the fitting procedure based on Eq. 3.9 to the experimental ST-FMR signal measured for sample S2 for V_B = 0.13 V. The fitting curve is analyzed into a symmetric and antisymmetric lorentzian curve.

$$I_{\mathrm{RF}} = \sqrt{4V_{\mathrm{bckg}} / \frac{\partial^2 V}{\partial I^2}} \tag{3.10}$$

In our case, I_{RF} changes from 6.3 μA for sample S1 up to 21 μA for sample S3. The $\partial^2 V/\partial I^2$ value was obtained by the numerical differentiation of the dynamic conductance ($\partial V/\partial I$) measurements with respect to the applied bias current. Likewise, we measured $\partial V/\partial I$ at angles around θ=90°, and obtained $\partial^2 V/\partial I \partial\theta$. By fitting each ST-FMR spectra under different bias conditions to Eq. 3.9, we obtained the parallel and perpendicular torkances. By numerical integration of the torkance values, both the parallel and perpendicular torques were calculated. An example of the fitting procedure is presented in Fig. 3.20.

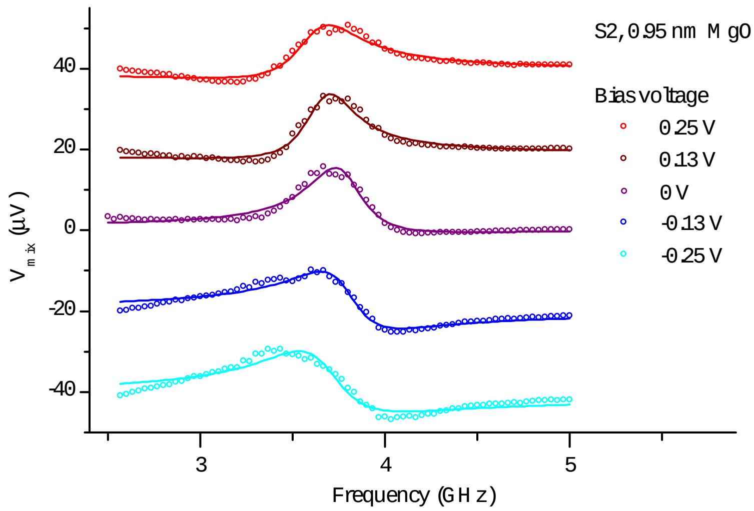

Figure 3.20: The ST-FMR spectra of sample S2 obtained by the application of an RF current to the MTJ nanopillar at different DC bias voltages with a static magnetic field applied. The experimental data are fitted to the sum of the symmetric and antisymmetric components of the Lorentzian function, according to Eq. 3.9

Figure 3.21a presents a comparison of the in-plane torkance in samples S1, S2, and S3. The absolute value of the in-plane torkance increases with decreasing barrier thickness and it only weakly depends on DC bias voltage. According to Slonczewski's free electron model for elastic tunneling in symmetric MTJs, the in-plane torkance is proportional to the differential conductance measured for parallel alignment of FL and RL [33]:

$$\frac{d\tau_{\|}}{dV} = \frac{\hbar}{2e}\frac{2p}{1+p^2}\left(\frac{dI}{dV}\right)_{\|} \tag{3.11}$$

By using Julliere's model to derive the spin polarization of the tunneling current p at V = 0 V, we found a good match between our experimental data and theoretical calculations based on Eq.3.11 (Fig. 3.21(a)). The absolute torque values in Fig. 3.21(b) were obtained by numerical integration of the data in Fig. 3.21(a). Obviously, the in-plane torque varies linearly with DC bias current and it is independent of MgO tunnel barrier thickness. These results are in good agreement with previously published experimental data in Refs [34] and calculations based on an *ab initio* approach [35].

Experimental data on the perpendicular torkance are summarized in Fig. 3.21(c). For samples S1 and S2, the torkance decreases with DC bias voltage and $d\tau_{\perp}/dV = 0$ for zero DC bias voltage as predicted by theoretical calculations. However, a discrepancy is observed for sample S3. In this sample, strong ferromagnetic coupling between the FL and RL of the MTJs results in asymmetrical double resonance modes in the ST-FMR spectra. The fitting procedure based on Eq. 3.9 therefore introduces an error in the experimental torkance values for this sample. A good match with theoretical calculations is obtained when this artifact is compensated by subtraction of a constant torkance value. Figure 3.21(d) illustrates that the absolute perpendicular torque varies quadratically with DC bias current. Moreover, $\tau_{\perp}$ is similar for all samples. We note that different torque versus bias dependencies have been measured recently. Especially, it has been shown that the shape of $\tau_{\perp}$(V) curves can change from quadratic to linear [36]. However, such effects were only measured in asymmetric MTJs with different FL and RL electrodes. In our junctions, the composition and thickness of the CoFeB electrodes are the same

[33] Slonczewski, J. C. and Sun, J. Z. *Journal of Magnetism and Magnetic Materials* **310**(2), 169 (2007)

[34] Sankey, J. C., Cui, Y., Sun, J. Z., Slonczewski, J. C., Buhrman, R. A., and Ralph, D. C. *Nature Physics* **4**(1), 67 (2007); Kubota, H., Fukushima, A., Yakushiji, K., Nagahama, T., Yuasa, S., Ando, K., Maehara, H., Nagamine, Y., Tsunekawa, K., Djayaprawira, D. D., Watanabe, N., and Suzuki, Y. *Nature Physics* **4**(1), 37 (2007); Wang, C., Cui, Y., Sun, J., Katine, J., Buhrman, R., and Ralph, D. *Physical Review B* **79**(22), 224416 (2009); and

[35] Heiliger, C. and Stiles, M. *Physical Review Letters* **100**(18) (2008); and Jia, X., Xia, K., Ke, Y., and Guo, H. *Physical Review B* **84**(1), 014401 (2011)

[36] Chanthbouala, A., Matsumoto, R., Grollier, J., Cros, V., Anane, A., Fert, A., Khvalkovskiy, A. V., Zvezdin, K. A., Nishimura, K., Nagamine, Y., Maehara, H., Tsunekawa, K., Fukushima, A., and Yuasa, S. *Nature Physics* **7**, 626 (2011); and Matsumoto, R., Chanthbouala, A., Grollier, J., Cros, V., Fert, A., Nishimura, K., Nagamine, Y., Maehara, H., Tsunekawa, K., Fukushima, A., and Yuasa, S. *Applied Physics Express* **4**(6), 063001 (2011)

Sample	MgO thickness (nm)	RA product ($\Omega\mu m^2$)	TMR (%)	$\tau_{\|}$ @ V_B = 0.2 V (Nm)
Sankey	1.25	15	160	$8.3e^{-21}$
S1	1.01	9.5	170	$5.2e^{-20}$
S2	0.95	6.5	160	$1.2e^{-19}$
S3	0.76	3.5	110	$6.7e^{-19}$
Kubota	1	2	154	$1e^{-19}$

Table 3.3: Comparison between the in-plane spin-transfer torque measured for the purpose of this thesis and the results obtained in previously published experiments. .

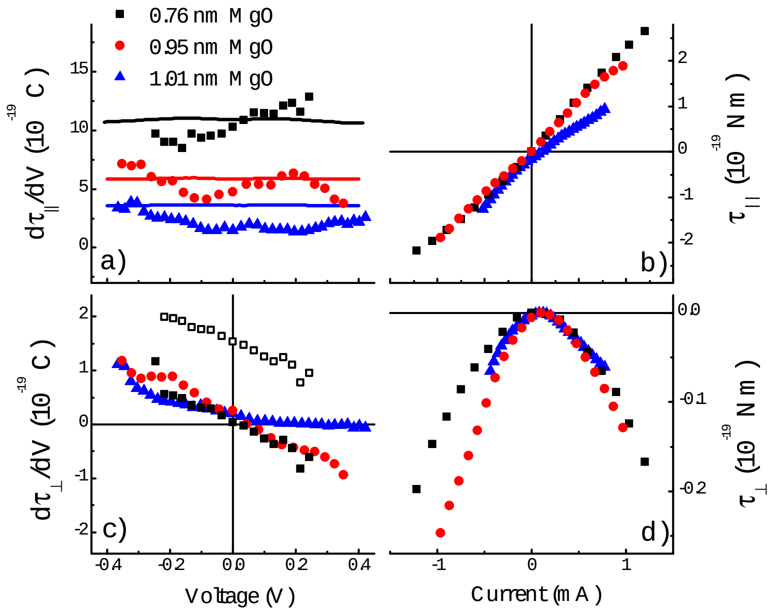

Figure 3.21: Bias dependence of the in-plane torkance (a), in-plane torque (b), perpendicular torkance (c) and perpendicular torque (d) for MTJs with different MgO barrier thickness. The solid lines in (a) represent calculations based on Eq. 3.11. The torque values are numerically integrated from experimentally determined torkances. $\tau_{\perp}$ for sample S3 was compensated for an error originating from asymmetric ST-FMR resonances.

3.3.6 Conclusion

In summary, we have investigated MTJ nanopillars with varied MgO tunnel barrier thickness using the spin-torque diode effect. We measured a symmetric ST-FMR signal for samples with $t_{\mathrm{MgO}} > 0.9$ nm. In this case, the coupling between FL and RL is weakly antiferromagnetic. Contrary, double and closely-spaced resonance modes were obtained for MTJs with a 0.76 nm thick tunnel barrier. Macrospin simulations indicate that the asymmetric double-peaks originate from inhomogeneous magnetization precession in the FL caused by ferromagnetic coupling to the RL. The in-plane and perpendicular torques scale with DC bias current and they are independent of MgO tunnel barrier thickness. The shapes of the torques vs. bias voltage curves are similar to the *ab initio* calculations presented in Fig. 3.22.

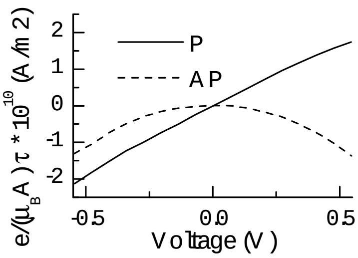

Figure 3.22: In-plane (solid lines) and perpendicular (dashed lines) torques vs. bias voltage calculated for 19 monolayer Fe.

Adapted from Heiliger, C. and Stiles, M. *Physical Review Letters* **100**(18) (2008)

3.4 *Low frequency noise*

3.4.1 *Introduction*

In order to properly design a basic memory cell, the electric noise generated by the device should be taken into account. The simplest memory cell unit consists of a bistable element, that can be initiated in one of the two distinguishable states. In the case of an MTJ, two magnetization states, P and AP, can be controlled by means of a magnetic field or the spin polarized current, using CIMS effect. The memory state can be read by a direct resistance measurement. Therefore, a possibly high TMR ratio is necessary, in order to separate the two magnetization states. In addition, the electric noise influences the readout margin, which can significantly reduce an overall memory speed[37].

[37] Small TMR affects the resistance difference between P and AP states. If this difference is not high enough, a more precise and time-consuming readout is necessary, which affects the memory operation speed.

In this section, the low frequency noise measurement results of MTJs with different tunnel barrier thickness are presented and the contribution of different noise mechanisms introduced in section 2.3 are discussed.

3.4.2 *Experimental*

For the electric and magnetic noise study, the same MTJ sample set (S1, S2 and S3) as in section 3.3 was used. Each characterized sample was mounted onto a chip carrier. The electrical connections to the top and bottom lead were realized by means of wedge bonding. The chip was placed in the magnetic field coils and the MTJ was connected to a low noise amplifier. In addition, the MTJ was supplied with a DC bias voltage. The supply voltage to all electronic components was realized by using a battery source, which reduces the influence of the network noise. The entire setup was placed in a metal box, which screens external magnetic fields.

The gain of the low noise amplifiers was set to 60 dB. The amplified signal was recorded using a 4 MS/s DAQ card . After the FFT calculations of the recorded signal, the results obtained were similar to the ones for a conventional spectrum analyzer. For details of the noise measurement setup, see section 5.3.4.

DAQ - data acquisition card
FFT - fast Fourier transform

3.4.3 *Data and analysis*

Figure 3.23 presents the noise power spectral density vs.the frequency curves of the sample S3 with a tunnel barrier thickness of t_B = 0.76 nm, measured both for the P and AP magnetization state. No magnetic field was applied during the measurement. Both the white noise (which is the sum of thermal and shot noise) and the 1/f noise can be distinguished. The amplitude of the latter increases with increasing bias voltage, which substatiates the previous experimental results [38]. The bottom noise level of $S_n = 1 \times 10^{-17}$ V^2/Hz corresponds to the amplifier noise ($S_{amp} = 1.6 \times 10^{-17}$ V^2/Hz). The thermal noise of the MTJ with a resistance of

[38] Almeida, J. M., Ferreira, R., Freitas, P. P., Langer, J., Ocker, B., and Maass, W. *Journal of Applied Physics* **99**(8), 08B314 (2006)

$R_{S3} = 120$ Ohm at room temperature, calculated on the basis of Eq. 2.20 is $S_n = 4 \times 10^{-18}$ V^2/Hz, which is below the setup resolution and cannot be directly identified. The resistance vs. magnetic field hysteresis loop with colored points, which indicate the MTJ state during noise measurement is presented in Fig. 3.24.

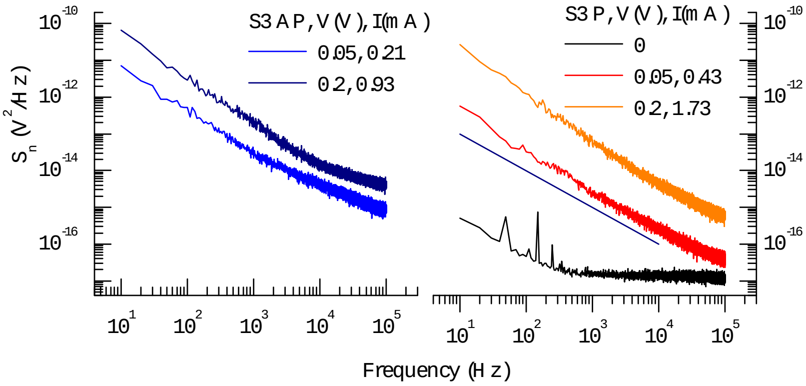

Figure 3.23: Noise power spectral density vs. the frequency measured for sample S3, with $t_B = 0.76$ nm for AP (left) and P (right) state, respectively. The 1/f noise dominates the measurement at this frequency range for $V_B > 0$. At $V_B = 0$, below $f < 500$ Hz the increased noise signal is due to the measurement setup. The spikes correspond to the network frequency (50 Hz) and its multiplications.

In order to quantitatively describe the 1/f noise contribution, a Hooge α_H parameter can be calculated according to the Eq. 2.23. Assuming the MTJ area $A = 22 \times 10^{-15}$ m^2, the derived values are: $\alpha_{H-AP} = 1.1 \times 10^{-22}$ and $\alpha_{H-P} = 0.33 \times 10^{-22}$ for the AP and P states, respectively. These values are comparable to the other experimental findings for a low RA product MTJs[39]. The calculated α_H denotes the noise level of the MTJ, within a low frequency range. This noise is typically higher for the high RA product MTJs. On the other hand, low RA junctions require a smaller area, so that the MTJ resistance is high enough and can be used in practice. Junctions with a small area produce higher 1/f noise, according to the Eq. 2.23, so an optimal physical MTJ parameter must be used for specific applications. It should be noted, that 1/f noise residuals are also present in the case of $V_B = 0$, below 500 Hz, however, this signal is generated by the measurement setup (mainly amplifier) itself.

[39] Lei, Z. Q., Li, G. J., Egelhoff, W. F., Lai, P. T., and Pong, P. W. T. *IEEE Transactions on Magnetics* **47**(3), 602 (2011)

A similar analysis was performed for the MTJ sample S1 with a thicker MgO tunnel barrier - Fig. 3.25. Clearly the shape of the curve measured at the P state differs from an ideal 1/f dependence. Such behavior is typically attributed to the RTN [40]. In order to further support this hypothesis, a time-domain measurement was performed.

[40] Herranz, D., Gomez-Ibarlucea, A., Schafers, M., Lara, A., Reiss, G., and Aliev, F. G. *Applied Physics Letters* **99**(6), 062511 (2011)

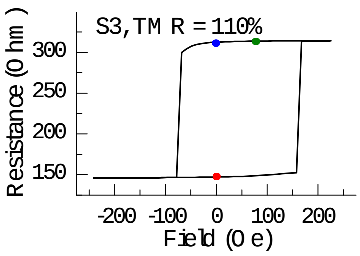

Figure 3.24: Resistance vs. magnetic field loop of sample S3. Points on the loops indicate the MTJ state, for which noise power spectral density was measured.

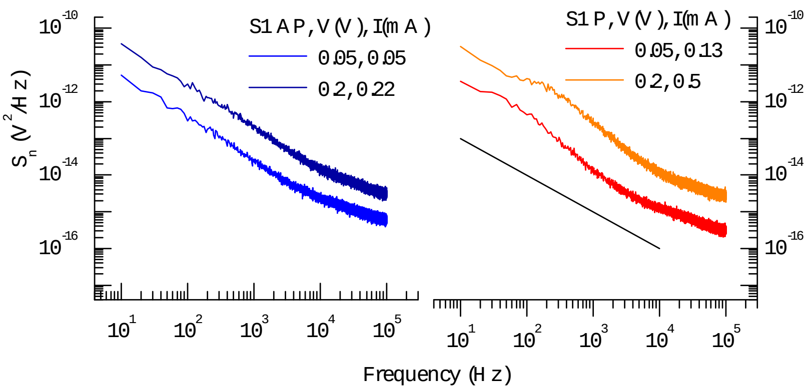

Figure 3.25: Noise power spectral density vs. the frequency measured for sample S1, with t_B = 1.01 nm for AP (left) and P (right) state, respectively. Apart from 1/f noise, another noise source contribution is observed at the P state around the frequency of f = 200 Hz.

Figure 3.26 presents the noise signal in a time domain for V_B = 0.1 V, measured with a sampling rate of 4 MS/s. Clearly, two resistance states can be distinguished in the measurement with random transitions between them. The average time step between these transitions is 5 ms, which corresponds to 200 Hz, the frequency at which deviation from 1/f noise can be seen. These different resistances can be attributed to a different magnetic domain configuration in the FL, which slightly influences the MTJ resistance and, thus, the measured voltage.

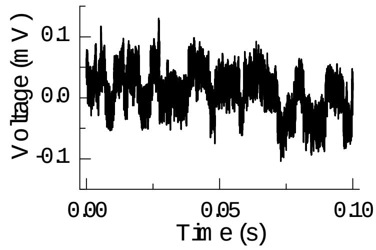

Figure 3.26: Time domain measurement of the RTN for sample S1 with t_B = 1.01 at P state. Clear steps can be distinguished from a measurement with an average duration time of t = 5 ms. These random transitions are responsible for an increased noise value at given frequency $f = 1/t$ observed in Fig. 3.25.

The RTN in this case, is independent of the bias voltage conditions, and the magnetic configuration alone defines its presence. In Ref. [41] the MTJs with two different areas, i.e., the different contribution of the stray fields are discussed. There, the experimental TMR vs. magnetic field curves, together with micromagnetic simulations, prove the existence of the inhomogeneous magnetization in the FL.

[41] Herranz, D., Gomez-Ibarlucea, A., Schafers, M., Lara, A., Reiss, G., and Aliev, F. G. *Applied Physics Letters* **99**(6), 062511 (2011)

In order to support the magnetic origin of RTN in our case, two noise curves of sample S3 (strong ferromagnetic coupling between the FL and RL dominates in this case) at AP state, measured with H_{ext} = 0 Oe and H_{ext} = 90 Oe - are shown in Fig. 3.27.

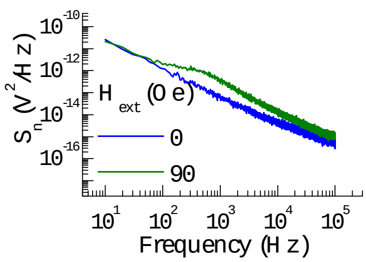

Figure 3.27: Comparison between noise power spectral density measured in sample S3 with t_B = 0.76 at AP state for H_{ext} = 0 Oe (red) and H_{ext} = 90 Oe (green). Colored points on R(H) loop indicating MTJ state during the noise measurement are indicated in Fig. 3.24

Clearly, RTN appeared in the measurement with H_{ext} = 90 Oe. In this case, the competition between stray fields, interlayer exchange coupling and the external magnetic field results in a magnetic domain formation in the FL, which affects the MTJ inherent noise. Due to the thermal activation, the domain wall hops between the pinning centers and this domain hopping is responsible for the RTN appearance [42]. Such pinning centers might originate from imperfect MTJ shape (discussed in section 5.2) or other disorders in the MTJ structure. In the frequency ranges below (f < 100 Hz) and above (f > 10 kHz) RTN, noise power spectral density is independent on the magnetic field.

[42] Ingvarsson, S., Xiao, G., Parkin, S. S. P., Gallagher, W. J., Grinstein, G., and Koch, R. H. *Physical Review Letters* **85**(15), 3289 (2000)

3.4.4 Conclusions

The operation of a device that utilizes MTJs as the active element, like for example a magnetic field sensor is limited by the 1/f noise. An analysis of different noise sources in MTJs with thin MgO tunnel barriers was performed, focusing on thermal, 1/f and random telegraph noise. Typical frequencies in a storage devices lies above 100 MHz, and 1/f noise can be neglected in those cases. However, this kind of noise source is of great importance for the low frequency magnetic fields detection. As shown in Fig. 2.11 in the section on 2.3 at higher frequencies $f > 100$ MHz, apart from the thermal and shot noise, only the noise that originates from the STT self excitation is present. It was found that this noise, described in detail in the next section, can in practice be used in microwave electronics as a high-frequency oscillator.

3.5 High frequency spin torque oscillator based on MTJ with tilted free layer

The content of this section is based on the work: Skowroński, W., Stobiecki, T., Wrona, J., Reiss, G., and van Dijken, S. *Applied Physics Express* **5**(6), 063005 (2012). The authors contribution: nanofabrication of samples, static and dynamic electric measurements, data analysis, manuscript preparation.

3.5.1 Introduction

As introduced in the chapter on 2, DC currents in MTJs can induce a steady-state precession of the magnetic moment due to the interaction between spin-polarized electrons and the local magnetization of the FL. This STT effect [43] induces resistance oscillations in the MTJs, which in turn generate an AC voltage signal across the junction in the GHz frequency range. These STT-based nanometer-scale oscillators could potentially compete with existing LC-tank technologies used in high-frequency electronics. However, one of the main drawbacks of spin torque oscillators (STOs) thus far is the need for an external magnetic field to stabilize their microwave signal. These features have drawn a significant amount of attention because of their potential use as high-density memory cells [44] and microwave electronic components [45].

To reduce the external magnetic field in all-metallic spin valve structures, the use of a perpendicular magnetized reference layer (RL) or FL has been explored [46], and the dynamic response as a function of the magnetization angle has been numerically simulated [47]. , It has also been shown that magnetic vortex oscillators can operate in small magnetic fields [48].Finally, zero-field auto-oscillations of the synthetic ferrimagnet in MTJs have been observed for large tunneling currents that significantly decrease the resistance and tunneling magnetoresistance (TMR) [49].

In this section, we report on a new approach for the generation of STOs in CoFeB/MgO/CoFeB [50] MTJs without the application of an external magnetic field. Our approach utilizes the perpendicular magnetic anisotropy of the CoFeB/MgO interface to tilt the magnetization of the thin FL layer out-of-the film plane. Together with ferromagnetic interlayer coupling across the thin MgO tunnel barrier, this results in a stable magnetization configuration, which can be excited into persistent microwave-frequency oscillations by STT in zero magnetic field. The ability to operate STOs in this mode opens new possiblities for the design of spin torque devices without cumbersome magnetic field sources.

3.5.2 Experimental

The MTJ stack with a CoFeB wedge-shaped electrode was deposited. The multilayer structure consisted of the following materials (thickness in nm): buffer layers / PtMn (16) / $Co_{70}Fe_{30}$(2)

[43] Slonczewski, J. C. *Journal of Magnetism and Magnetic Materials* **159**(1-2), L1 (1996); and Berger, L. *Physical Review B* **54**(13), 9353 (1996)

[44] Takemura, R., Kawahara, T., Miura, K., Yamamoto, H., Hayakawa, J., Matsuzaki, N., Ono, K., Yamanouchi, M., Ito, K., Takahashi, H., Ikeda, S., Hasegawa, H., Matsuoka, H., and Ohno, H. *IEEE Journal of Solid-State Circuits* **45**(4), 869 (2010)

[45] Kiselev, S. I., Sankey, J. C., Krivorotov, I. N., Emley, N. C., Schoelkopf, R. J., Buhrman, R. A., and Ralph, D. C. *Nature* **425**(6956), 380 (2003); and Deac, A. M., Fukushima, A., Kubota, H., Maehara, H., Suzuki, Y., Yuasa, S., Nagamine, Y., Tsunekawa, K., Djayaprawira, D. D., and Watanabe, N. *Nature Physics* **4**(10), 803 (2008)

[46] Boulle, O., Cros, V., Grollier, J., Pereira, L. G., Deranlot, C., Petroff, F., Faini, G., Barnaś, J., and Fert, A. *Nature Physics* **3**(7), 492 (2007); Houssameddine, D., Ebels, U., Delaët, B., Rodmacq, B., Firastrau, I., Ponthenier, F., Brunet, M., Thirion, C., Michel, J., Prejbeanu-Buda, L., Cyrille, M., Redon, O., and Dieny, B. *Nature Materials* **6**(6), 447 (2007); and Rippard, W. H., Deac, A. M., Pufall, M. R., Shaw, J. M., Keller, M. W., Russek, S. E., and Serpico, C. *Physical Review B* **81**(1), 014426 (2010)

[47] Zhou, Y., Bonetti, S., Zha, C. L., and Akerman, J. *New Journal of Physics* **11**, 103028 (2009)

[48] Pribiag, V. S., Krivorotov, I. N., Fuchs, G. D., Braganca, P. M., Ozatay, O., Sankey, J. C., Ralph, D. C., and Buhrman, R. A. *Nature Physics* **3**(7), 498 (2007)

[49] Devolder, T., Bianchini, L., Kim, J., Crozat, P., Chappert, C., Cornelissen, S., de Beeck, M. O., and Lagae, L. *Journal of Applied Physics* **106**(10), 103921 (2009)

[50] Djayaprawira, D. D., Tsunekawa, K., Nagai, M., Maehara, H., Yamagata, S., Watanabe, N., Yuasa, S., Suzuki, Y., and Ando, K. *Applied Physics Letters* **86**(9), 092502 (2005)

/ Ru(0.9) / $Co_{40}Fe_{40}B_{20}$(2.3) / MgO(0.85) / $Co_{40}Fe_{40}B_{20}$(1 - 2.3) / capping layer. The deposition process was similar to that used in previous sections. After deposition, four different parts of the samples with different FL thicknesses of 1.22, 1.35, 1.57, and 2.3 nm were selected for patterning into nanometer-size pillars. For these studies, nanopillars with an elliptical cross section of 250 $\times$ 150 nm^2 were fabricated. Similar to the design presented in section 3.3, the overlap between the top and bottom leads was limited to about 4 μm^2, which resulted in a capacitance of less than 1×10^{-14} F. The DC measurements were conducted at room temperature with a magnetic field applied in the sample plane. The high-frequency measurements were carried out using the setup described in section 5.3.2.

3.5.3 *Data and analysis*

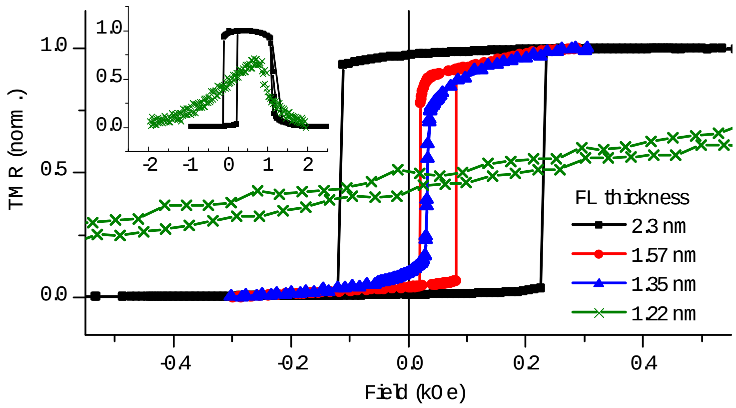

Figure 3.28: Normalized TMR vs magnetic field curves for junctions with different FL thicknesses measured with a bias voltage of V_b = 10 mV. The inset shows the same data for the samples with 1.22 and 2.3 nm FLs for larger applied magnetic fields. The abrupt switching of the 2.3 nm FL indicates an in-plane alignment of the CoFeB magnetization, whereas the linear response of the 1.22 nm FL demonstrates a hard in-plane magnetization axis. For the MTJ with a 1.22 nm FL, a full AP state is not reached, because the RL flips at 0.8 kOe. The TMR for this sample is normalized to the extrapolated AP resistance value.

Figure 3.28 shows TMR loops for all samples, with the field applied along the in-plane easy axis of the MTJ. The shape of the TMR curves change as a function of FL thickness. For 2.3 nm CoFeB, the FL switches abruptly, indicating an in-plane alignment of the FL magnetization. The TMR of the junction with the thinnest FL, on the other hand, varies linearly with applied magnetic field. In this case, the magnetization of the FL is oriented out-of-plane in remanence and the application of a magnetic field coherently rotates the magnetization towards the film plane. The responses of the samples with 1.35 and 1.57 nm FLs are attributed to an intermediate configuration whereby the average magnetization angle of the CoFeB FL is tilted out of the film plane. The out-of-plane tilt of the FL originates from a perpendicular anisotropy effect at the MgO/CoFeB interface [51]. The competition between this interface anisotropy and the in-plane shape anisotropy results in a spin reorientation transition with increasing FL thickness. The thickness range for this transition in our experiments ($\sim$ 1.2-2.3 nm) agrees well with those in the literature [52]. Table 3.4 shows the transport

[51] Yakata, S., Kubota, H., Suzuki, Y., Yakushiji, K., Fukushima, A., Yuasa, S., and Ando, K. *Journal of Applied Physics* **105**(7), 07D131 (2009); and Ikeda, S., Miura, K., Yamamoto, H., Mizunuma, K., Gan, H. D., Endo, M., Kanai, S., Hayakawa, J., Matsukura, F., and Ohno, H. *Nature Materials* **9**(9), 721 (2010)

[52] Wiśniowski, P., Almeida, J. M., Cardoso, S., Barradas, N. P., and Freitas, P. P. *Journal of Applied Physics* **103**(7), 07A910 (2008)

properties of the MTJs. The average tilt angle of the FL magnetization in the zero magnetic field was estimated from the shape of the TMR curves. The observed decrease in the level of the TMR effect with decreasing FL thickness is partly caused by the out-of-plane tilt of the FL magnetization (abrupt switching between P and AP magnetization states is no longer achieved for a 1.22 nm FL) and it is further reduced by a decrease in the spin polarization of ultrathin CoFeB films [53].

[53] Sun, J. J. and Freitas, P. P. *Journal of Applied Physics* **85**, 5264 (1999)

Another important parameter for obtaining zero-field spin torque oscillations is the interlayer coupling between the two CoFeB electrodes. In our junctions, the coupling between the FL and the RL is ferromagnetic as evidenced by the positive field shift in the TMR curves in Fig. 3.28. The ferromagnetic interlayer coupling, whose origin is analyzed in detail in section 3.1 stabilizes the low resistance state of the MTJs in the zero magnetic field.

FL thickness (nm)	TMR ratio (%)	R_p (Ohm)	Average θ (deg)	Power (pW)	I_c (mA)
1.22	8	102	84	-	-
1.35	50	120	43	411	-0.95
1.57	100	110	26	19.3	-1.8
2.3	120	130	4	2.4	-2.4

Table 3.4: Summary of MTJ parameters. The STO integrated power was calculated from the power density spectra curves measured with a current of I_b = -1 mA. The critical current is defined as the current necessary to switch the magnetization from the P state to the AP state in the zero external magnetic field.

In quasi-static transport measurements, the samples with an FL thickness of 1.35-2.3 nm show a clear current-induced magnetization switching for relatively long current pulses of 10 ms. The absolute switching current that is required to switch the MTJ from a low resistance state to a high resistance state in the zero applied magnetic field decreases in thin FLs (Table 3.4). This effect is most likely caused by an increase in the FL tilt angle and a reduction in the FL magnetic moment. Abrupt switching does not occur in junctions with a 1.22 nm FL and, consequently, quasi-static current-induced effects are absent.

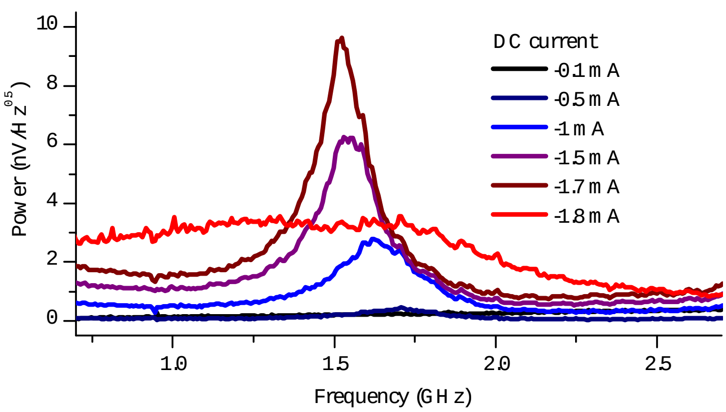

Figure 3.29: The STO spectra of MTJ with a 1.57 nm FL measured in the zero external magnetic field for different negative tunneling currents.

Because the switching voltage is much smaller than the breakdown voltage, steady-state precessions can be induced without destroying the MTJ. A selection of STO spectra for a sample with a 1.57 nm FL is shown in Fig. 3.29. No magnetic field was applied during these measurements. For this MTJ, the perpendicular anisotropy of the CoFeB/MgO interface tilts the magnetization of the FL out of the film plane, while its in-plane component remains parallel to the magnetization of the RL and, thus, a relatively low resistance state is obtained (Fig. 3.28). Under these conditions, the excitation of steady-state precessions requires only a small DC current. An increase in negative tunneling current that favors the AP state (electrons flowing from the FL to the RL) increases the amplitude of the oscillations to more than 9 nV/$\sqrt{Hz}$ (0.14 nW power) at 1.5 GHz and -1.7 mA. Here, corrections due to impedance mismatch were taken into account [54]. A further increase in negative DC current switches the MTJ to the high-resistance AP state, for which the STO peak is broader and less intense.

[54] Kiselev, S. I., Sankey, J. C., Krivorotov, I. N., Emley, N. C., Schoelkopf, R. J., Buhrman, R. A., and Ralph, D. C. *Nature* **425**(6956), 380 (2003)

The peak frequency (f_0) and its evolution with magnetic field strength are consistent with the excitation of the microwave-frequency oscillation in the CoFeB FL of our MTJs, presented in section 3.2. This is also confirmed by simulations that take appropriate magnetic anisotropy values into account. STOs of the synthetic ferrimagnetic RL, which are expected to occur at higher frequencies, are not observed in our experiments [55]. We also noted that the resistance and TMR of the junctions do not change during microwave excitation in the zero magnetic field.

[55] Cornelissen, S., Bianchini, L., Devolder, T., Kim, J., Roy, W. V., Lagae, L., and Chappert, C. *Physical Review B* **81**(14), 144408 (2010)

Figure 3.30 shows the STO amplitudes, f_0, and linewidth (Δf) versus DC tunneling current in the zero external magnetic field. Clearly, the oscillation amplitude increases with decreasing FL thickness. Larger amplitudes are thus obtained when the magnetization of the CoFeB FL is tilted out of the film plane. Moreover, for samples with FL thicknesses of 1.35 and 1.57 nm, a pronounced asymmetry is observed with respect to the polarity of the tunneling current. For these samples, the oscillations are more powerful for negative currents favoring the AP state than for positive currents favoring the P state. This asymmetry is expected because the MTJ is in a near P state and, hence, the spin torque effect tends to destabilize the FL magnetization more for negative polarity. For the MTJ with an FL thickness of 2.3 nm, the oscillation amplitude is smaller and symmetric with respect to the polarity of the current, which is reminiscent of thermally excited resonances [56].

[56] Deac, A. M., Fukushima, A., Kubota, H., Maehara, H., Suzuki, Y., Yuasa, S., Nagamine, Y., Tsunekawa, K., Djayaprawira, D. D., and Watanabe, N. *Nature Physics* **4**(10), 803 (2008)

f_0 in zero applied magnetic field increases with increasing FL thickness as shown in Fig. 3.30(b). This evolution is explained by an increase in the in-plane magnetic anisotropy of the FL, which results in smaller precession trajectories and larger f_0. We noted that a sample-to-sample distribution in both oscillation amplitude and frequency is observed, due to the size and shape distribution after nanolithography processing, however, the overall tendency is retained. For the MTJ with a 1.22 nm FL, we were not able to observe any oscillations in the measured bandwidth even with

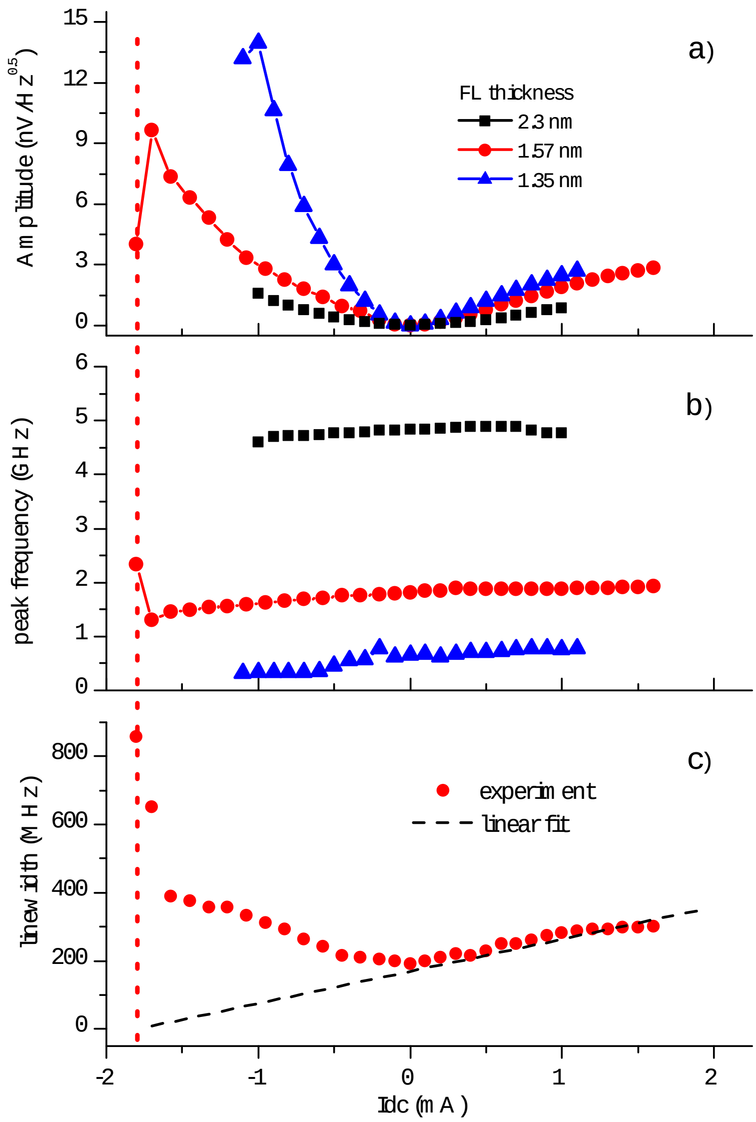

Figure 3.30: DC bias current dependence of the STO amplitude (a), peak frequency f_0 (b), and linewidth Δf (sample 1.57 only) (c). No magnetic field was applied during the measurements. The dashed line in (c) represents a linear fit to the experimental data for positive I_{dc}. Near the switching current (dotted line), both f_0 and Δf increase.

magnetic fields of up to 0.25 T applied parallel or perpendicular to the sample plane.

The dependence of the oscillation linewidth on DC tunneling current can be expressed as

$$\Delta f = \frac{\sigma}{2\pi}\left(I_{c0} - I_{dc}\right), \tag{3.12}$$

where σ is the spin polarization efficiency and I_{c0} is the critical switching current [57]. Extrapolation of Δf at the damping side (when the MTJ is in a near P state and the current direction favors the P state) to zero frequency gives an estimation of the switching current (dotted line in Fig. 3.30) of about -1.7 mA, which is in good agreement with the value of -1.8 mA from quasi-static transport measurements (Table 3.4). Moreover, abrupt changes in f_0 and Δf observed near the switching threshold also indicate a transition from steady-state precessions to current-induced magnetization switching.

[57] Wada, T., Yamane, T., Seki, T., Nozaki, T., Suzuki, Y., Kubota, H., Fukushima, A., Yuasa, S., Maehara, H., Nagamine, Y., Tsunekawa, K., Djayaprawira, D. D., and Watanabe, N. *Physical Review B* **81**(10), 104410 (2010)

Fig. 3.31 presents the measured STO spectra for the MTJs with different FL thickness at I_{DC} = -1 mA without an external magnetic field. Clear dependence of the precession frequency and magnitude is observed in the measurements. Although the highest power was measured for the MTJ with 1.35 nm FL, low frequency and relatively broad oscillations linewidth limits the practical application of such a device.

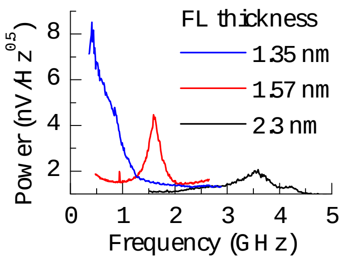

Figure 3.31: STO spectra of MTJs with 2.3, 1.57 and 1.35 nm thick FL, measured at I_{DC} = -1 mA without an external magnetic field.

According to recent theoretical works [58], in-plane oscillations are characterized by a less intense and narrower oscillation peak. This is the case in our experimental data for I_b below I_{c0}. Much broader peaks are measured when I_b is greater than I_{c0}, which signals a transition to the combined chaotic in-plane and out-of-plane oscillations.

[58] Ogrodnik, P., Wilczyński, M., Barnaś, J., and Świrkowicz, R. *IEEE Transactions on Magnetics* **47**(6), 1627 (2011)

3.5.4 *Conclusion*

In summary, we have demonstrated that CoFeB/MgO/CoFeB STOs can produce microwave signals in the zero external magnetic field. Due to the ferromagnetic interlayer exchange coupling in our MTJs, the STOs are in a low-resistance state in the zero field. The perpendicular interface anisotropy of the CoFeB FL on top of the MgO tunnel barrier tilts the FL magnetization out of the film plane and this stabilizes steady-state precessions in small DC tunneling currents. We conclude that by taking advantage of the coupling mechanisms in MTJs and the perpendicular anisotropy of the MgO/CoFeB interface, the performance of STOs can be enhanced without the need of an external magnetic field.

4
Summary and Outlook

This chapter summarizes the theoretical and practical implications of the results obtained throughout this thesis. Firstly, the theoretical predictions of the key parameters of MTJs are discussed and compared with the experimental findings of TMR, critical current density in CIMS, and couplings low and high frequency noise. STT-related effects are thoroughly analyzed as they are the main components of the current-controlled magnetization dynamics. Afterwards, practical implications of the results are considered with respect to the design of the novel STT-MRAM as well as the new microwave electronics components. Finally an outlook on the field of magnetism is provided.

4.1 Theoretical implications

As shown in the previous sections, most of the theoretical predictions of the MTJs are well reflected in the experimental data.

TMR Theoretical prediction on spin filtering in the crystalline MgO tunnel barrier triggered active experimental efforts in optimizing tunnel barriers of the MTJs. The maximum TMR value of below 100% for amorphous barriers (for example Al_2O_3) rapidly increased up to a few hundred for Fe/MgO/Fe MTJs. The theoretically predicted TMR value of above 1000% at room temperature has not yet been reached, mainly due to technological issues. Nevertheless, TMR values of 100 - 200% obtained for the MTJs investigated in this thesis are suitable for the practical applications. It should be noted that competitive non-volatile memory technologies, like PCM offer a much higher resistance difference between logical states, but the durability of such technology is still an issue. MTJ based memory with the TMR exceeding 100% provide the necessary signal for a fast readout operation. However, materials with even higher spin polarization that can further improve the TMR ratios, like Heusler alloys for example, are still under investigation.

PCM - phase change memory

Critical current Previous MRAM designs used the Ampere's field generated by the current lines situated close to the memory cell. These lines were supplied with current pulses to write the magnetic state of MTJ cells. This type of design, has been successfully introduced into the commercial market [1], however, this memory cannot be scaled down to deep sub-micron size elements and therefore its capacity is limited.

[1] http://www.everspin.com/

The introduction of the STT-MRAM design solved the physical scalability problem, however, significant effort has been made in order to reduce the critical current density that is required to initiate one of the two states of the MTJ cell. Numerous ideas have been proposed for this problem, including layers with perpendicular magnetization, and complex materials with a reduced damping factor, etc. In this thesis, the main emphasis was put on tunnel barrier optimization. As presented in section 3.1, the J_{c0} increases with a decreasing tunnel barrier in the investigated MTJ. Based on theoretical predictions, J_{c0} is directly proportional to the effective damping factor α. An increase in J_{c0} was ascribed to both decreased spin polarization and increased damping, investigated in section 3.2. By taking into account the decreased TMR ratio and therefore reduced spin polarization, the estimation of the critical current for the MTJs with different tunnel barrier thickness was provided.

Interlayer exchange coupling In addition to the TMR and J_{c0} dependence on the tunnel barrier parameters, it was found that the interlayer exchange coupling between the FL and RL depends strongly on the MgO tunnel barrier thickness. In this case a strong discrepancy was noted with respect to the previously reported experimental work and theoretical predictions based on the free-electron model. We found ferromagnetic interlayer exchange coupling for all the investigated tunnel barrier thicknesses. This feature is ascribed to the complexity of the interfaces in the MTJ multilayer system fabricated using the sputtering method. Indeed, the interlayer exchange coupling was found to depend on the MgO sputtering conditions [2]. However, for patterned MTJ nanopillars, the interlayer exchange coupling was compensated by the coupling originating for the FL and RL stray field interactions. In case of thick tunnel barriers, where interlayer exchange coupling is weak, in the nanopillars, the overall coupling was thus antiferromagnetic.

[2] Wrona, J., Langer, J., Ocker, B., Maass, W., Kanak, J., Stobiecki, T., and Powroźnik, W. *Journal of Physics: Conference Series* **200**, 052032 (2010)

Noise Electrical noise measurements were performed on fabricated MTJ nanopillars with different MgO thicknesses. It was found that the thermal noise of low resistance MTJs is beyond the measurement resolution. 1/f noise, on the other hand, is present in every investigated device. It's amplitude described using a Hooge parameter increases with increasing bias voltage, which agrees with the theoretical predictions. Moreover, at certain external magnetic field, the RTN was measured in MTJs. Such noise was attributed to the thermally activated magnetic domain hopping in the FL.

Spin torque oscillator Based on the results obtained from the MTJ series with a varied thickness of MgO tunnel barrier, mainly the ferromagnetic coupling between RL and FL, and optimal STT switching conditions (current and voltage), a prototype device generating a high frequency signal was proposed. In addition, recently discovered phenomenon of the perpendicular magnetic anisotropy in the CoFeB/MgO/CoFeB system for thin FL was applied. It was found that up to a few nV/Hz^2 a high frequency signal can be measured from the MTJ supplied with a DC signal without external magnetic fields. Both the oscillation power and frequency strongly depend on the FL thickness.

4.2 Outlook

Work presented in this thesis is a rather small fraction of the total research on nanomagnetism carried out worldwide. To date, the MTJ structure is one of the most successful devices proposed in applied spin electronics. The use of MTJs in memory devices, common usage of the magnetic elements for decades, seems to be one of many possible future applications.

Towards a universal memory unit and beyond Replacing current DRAM or SRAM technologies with magnetic memories seems to be on the horizon. However, further changes in IT devices are possible thanks to the usage of the magnetic devices which have been proposed already. One of them [3] implies a system that is normally in the off-state and consumes a minimum amount of energy. The system turns itself on only when a certain action (interruption) has taken place (like for example, a key on the keyboard is pressed), after which, the device comes back to the idle-state. This architectural change is possible only by using non-volatile, fast and durable memory units, which can be provided by the STT-MRAM technology. Furthermore, by an integration of the deposition process of the magnetic elements with a standard CMOS process, memory units can be distributed within an electronic circuit, reducing the interconnections length and thus increasing operation speed.

In addition, an MTJ can be applied as a component of the logical circuits [4]. Using these magnetic elements, it is possible to combine both non-volatility and ability to process information in a single device, thereby creating a simple logic-memory processor.

Electric-field controlled magnetism Recently, it was discovered that apart from the magnetic field or the spin-polarized current, it is possible to manipulate the magnetic properties (e.g., magnetic anisotropy) of the nanostructures using an electric field [5]. Initial studies led to a prototype design of the memory cells based on electric-field-induced magnetization changes. However, either strong magnetic field [6] or spin-transfer-torque effect [7] are still necessary for the device to operate properly. Nevertheless, an additional way of controlling the magnetic elements in a nano-scale is very promising for future applications. Some effort has been

[3] Takemura, R., Kawahara, T., Miura, K., Yamamoto, H., Hayakawa, J., Matsuzaki, N., Ono, K., Yamanouchi, M., Ito, K., Takahashi, H., Ikeda, S., Hasegawa, H., Matsuoka, H., and Ohno, H. *IEEE Journal of Solid-State Circuits* **45**(4), 869 (2010)

CMOS - complementary metal-oxide semiconductor

[4] Suzuki, D., Natsui, M., Ikeda, S., Hasegawa, H., Miura, K., Hayakawa, J., Endoh, T., Ohno, H., and Hanyu, T. In *VLSI Circuits, 2009 Symposium on*, 80, (2009)

[5] Weisheit, M., Fahler, S., Marty, A., Souche, Y., Poinsignon, C., and Givord, D. *Science* **315**(5810), 349 (2007); Endo, M., Kanai, S., Ikeda, S., Matsukura, F., and Ohno, H. *Applied Physics Letters* **96**(21), 212503 (2010); and Maruyama, T., Shiota, Y., Nozaki, T., Ohta, K., Toda, N., Mizuguchi, M., Tulapurkar, A. A., Shinjo, T., Shiraishi, M., Mizukami, S., Ando, Y., and Suzuki, Y. *Nature Nanotechnology* **4**(3), 158 (2009)

[6] Shiota, Y., Nozaki, T., Bonell, F., Murakami, S., Shinjo, T., and Suzuki, Y. *Nature Materials* **11**(1), 39 November (2011)

[7] Wang, W.-G., Li, M., Hageman, S., and Chien, C. L. *Nature Materials* **11**(1), 64 (2011)

made by the author of this thesis, which resulted in the design of a voltage-tunable magnetic field sensor based on the MTJ [8]. This concept, however, is beyond the scope of this work.

[8] Skowroński, W., , Wiśniowski, P., Stobiecki, T., Cardoso, S., Freitas, P. P., and van Dijken, S. *Applied Physics Letters* **101**(19), 192401 (2012)

Pure spin currents Finally, in the spin electronic devices, charge currents, commonly used nowadays, in the future could be replaced by pure spin currents [9]. This means that a tremendous reduction in the energy consumption could be expected, due to the usage of atomic-scale all-spin-based devices. Spin currents described and used throughout this thesis are generated by the spin to charge convention. One of the goals of the future research will be a concept and devices using only the spin of electrons (or atoms, nuclei, molecules) without any charge dissipation.

[9] Khajetoorians, A. A., Wiebe, J., Chilian, B., and Wiesendanger, R. *Science* **332**(6033), 1062 (2011)

5 Appendices

5.1 Deposition methods

All multilayer systems used throughout this thesis were deposited in the Timaris PVD Cluster Tool System from Singulus Technologies AG by J. Wrona. The sputtering system contains ten sputtering targets in one UHV chamber with a base pressure of below 5×10^{-9} Torr. All the metallic layers were deposited using DC magnetron sputtering, whereas the MgO layer was deposited using RF-sputtering, directly from a sintered polycrystalline MgO target in Ar atmosphere. The RF power during MgO deposition was fixed to 6.6 W/cm^2 and the Ar pressure was set to 3.8 mTorr, which gave an optimal TMR ratio and a low RA products MTJs.

PVD - physical vapor deposition

UHV - ultra-high vacuum

An additional protective oxide layer and the top conducting layer used in the nanofabrication process described below were deposited in a separate deposition machine. This tool utilized metallic source sputtered in pure Ar atmosphere to deposit conducting layers or in Ar and O atmosphere to deposit insulating layers.

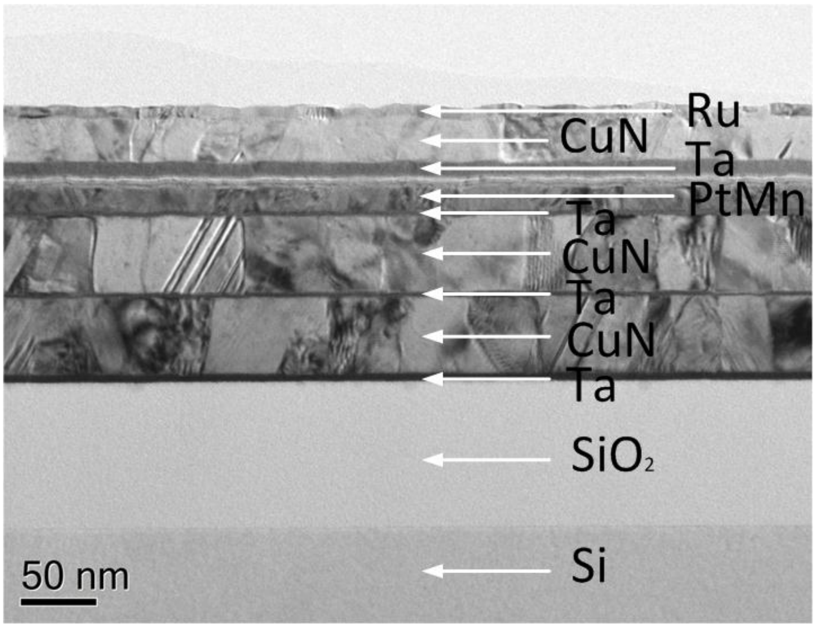

Figure 5.1: A TEM image of the entire MTJ multilayer by L. Yao. Most of the metallic layers can be distinguished. The MTJ trilayer on SAF is placed above PtMn layer.

The Timaris system uses LLD technology for deposition of wedged shape layers [1]. This technology was used for MgO wedge deposition in sections 3.1, 3.2, 3.3 and 3.4, and for the CoFeB FL deposition in the section on 3.5. LLD technology ensured , that exactly the same wafer with only one wedged shape layer was used for systematic research. Ta(5)/CuN(50)/Ta(3) (thickness in nm) buffer and capping layers were used to allow CIPT characterization on the wafer-level. Moreover, these buffer layers ensured minimal surface roughness of the deposited MTJ trilayer, which is crucial for high TMR ratio, low RA products and couplings discussed in chapter 2.

LLD - linear dynamic deposition

[1] Wrona, J., Langer, J., Ocker, B., Maass, W., Kanak, J., Stobiecki, T., and Powroźnik, W. *Journal of Physics: Conference Series* **200**, 052032 (2010)

After the deposition processing, samples were annealed in an in-plane magnetic field of 1 T at 360°C for 2 hours, in order to obtain (001) cubic homoepitaxial crystallization of the CoFeB electrodes - Fig. 5.2, and to induce unidirectional magnetic anisotropy due to an interactions between PtMn and CoFe layers (so called exchange bias structure - see section 2.1).

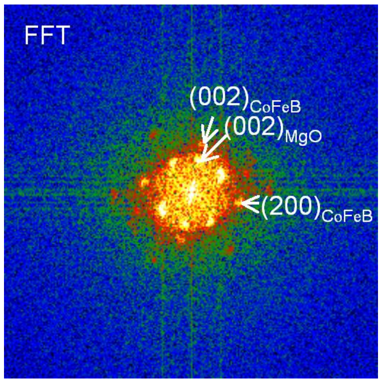

Figure 5.2: FFT pattern calculation from the polycrytalline area of the CoFeB/MgO/CoFeB trilayer marked with an *a* sign on the Fig. 5.3

A cross-section of the entire MTJ stack deposited on the Si/SiO_2 wafer is presented in Fig. 5.1. Most of the layers appear polycrystalline in the used magnification.

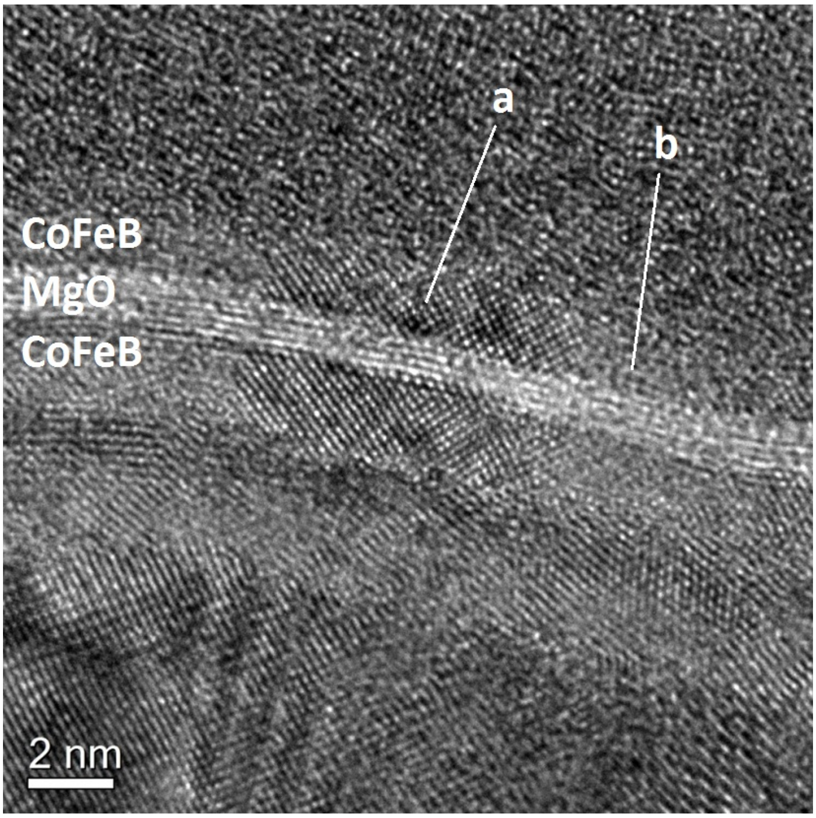

Figure 5.3: A magnified TEM image of the MTJ trilayer by L. Yao. Regions *a* and *b* indicate polycrystalline and amorphous CoFeB areas, respectively.

Figure 5.3 presents the TEM cross-section image of the annealed CoFeB/MgO/CoFeB trilayer used in this thesis. Smooth on atomic scale crystalline MgO tunnel barrier can be identified. Amorphous and crystalline CoFeB areas coexist both in FL and in RL after annealing.

In addition to the samples from Singulus AG, for some studies not described in this thesis, multilayers deposited by means of MBE at prof. J. Korecki's group at the AGH University, were used [2]. Unannealed MTJ consisting of MgO(substrate)/ Fe(30)/ MgO(1-3)/ Co(12)/ Au(5), revealed a TMR ration of up to 40%. A similar nanofabrication process was used to the one described below.

MBE - Molecular Beam Epitaxy

[2] Wilgocka-Ślęzak, D., Freindl, K., Kozioł, A., Matlak, K., Rams, M., Spiridis, N., Ślęzak, M., Ślęzak, T., Zając, M., and Korecki, J. *Phys. Rev. B* **81**, 064421 (2010)

5.2 *Nanofabrication process*

The nanofabrication process of deposited multilayer stacks consists of the following processes:

- bottom electrode definition,
- ion-beam milling,
- nanopillar definition,
- ion-beam milling,
- insulating layer deposition,
- lift-off,
- conducting layer deposition,
- top electrode definition,
- ion-beam milling.

The definition process of each part of the device includes: photo-resist deposition, baking, e-beam exposure and photo-resist development. Negative resist from Allresist AR-N 7520.18 was used for each step. The wafer with a deposited multilayer structure was covered with the above mentioned resist using a spin-coater set to 6000 rpm for 30 s. This procedure resulted in about a 400 nm thick resist layer. Afterwards, it was baked for 2 minutes at 82°C on a hot-plate. This prepared sample was mounted in an SEM LEO 1530 system with Gemini column. The SEM was integrated with a Raith Elphy plus nano-lithography system, which enabled precise control of the e-beam exposure. For the exposure purposes, a voltage of 20kV was used.

SEM - Scanning electron microscope

A few different mask designs were used for the nano-lithography process. Fig. 5.4 presents the first lithography mask of the optimized 3-step process. The exposed sample area of 3.3×3.3 mm was divided into 1089, 100×100 μm squares (corresponding to a write-field size). In the bottom-left, bottom-right and top-left corners of each mask design, the orientation marks were placed. The remaining area was filled with bottom electrodes of 36 elements. After setting a proper beam aperture, performing a beam-current measurement, focusing, making electron-beam corrections and sample alignment procedures, the wafer with a photo-resist on the top was exposed[3].

[3] see manual of the specific SEM and nanolithography system, for this specific design beam sizes of 0.08 μm for electrodes and 0.004 μm for nanopillars were used, with dose of 300 μAs/cm^2

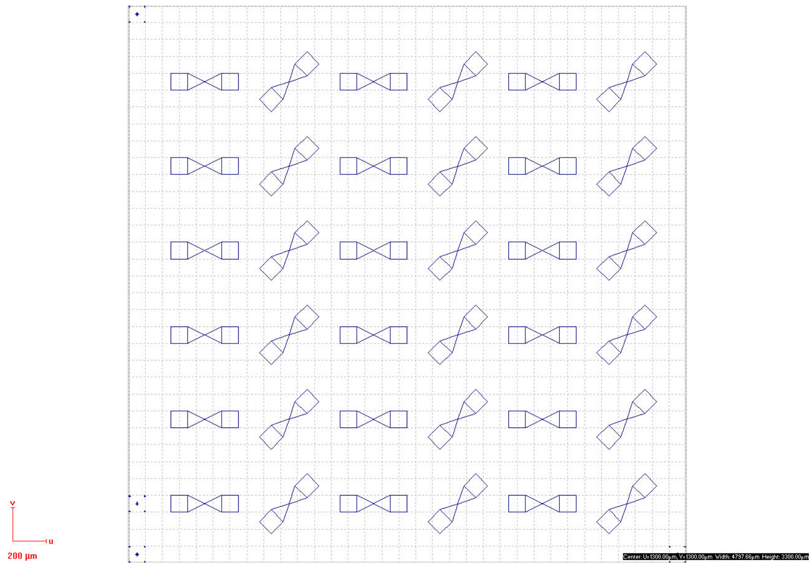

Figure 5.4: First mask design for the nano-lithography process with bottom electrodes of 36 elements. Orientation marks are placed in three corners.

Afterwards, the exposed resist was developed in an Allresist AR 300-47 developer for about 6 minutes, followed by rising in deionized water. This prepared wafer was ready for first ion-beam milling, which was performed in a home-built system at Bielefeld University. The system uses Ar ions (accelerated by a high voltage), which etches layers not covered by photoresist. During the process, the materials that are currently being etched are analyzed using a mass spectrum analyzer, which enables a rough control of the etching depth. In order to etch the materials surrounding the bottom electrode, an entire multilayer system, down to the SiO_2 buffer is removed.

After the etching step, the developed photo-resist is removed in an ultrasonic bath at 80°C for 30 minutes in 1-Methyl-2-pyrrolidinone Chromasolv Plus from Aldrich.

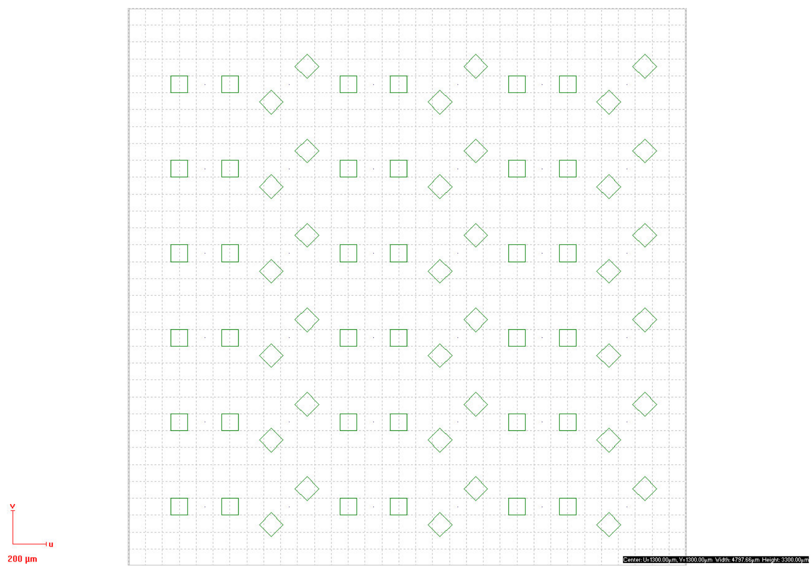

Figure 5.5: The second mask design for the nano-lithography process with MTJ nanopillars and contact to the bottom electrode of 36 elements. Small dot between contacts to the bottom electrode corresponds to 100 × 200 nm ellipse.

The next step included MTJ nanopillar definition together with a contact to the bottom electrode. The photo-resist preparation and exposure process is similar to the one described for the bottom electrode, however, for practical reasons, a smaller beam size was used for the nanopillar and a bigger one for the contact to the bottom electrode. The second mask is presented in Fig. 5.5

The etching process is also similar to the bottom electrode etching, however, in this step, the etching is terminated at the bottom conducting layer, in this case the Ta layer below the PtMn antiferromagnet. In addition, in this step, the developed resist is not removed as it will be used in a lift-off.

Afterwards, an insulating layer was deposited in order to prevent side-shorts through a tunnel barrier of the MTJ nanopillar. In this case the Ta film was sputtered in an oxygen atmosphere resulting in about 200 nm Ta_2O_5 film. Protective oxide was deposited on the entire multilayer structure, especially, covering the nanopillar with a photo-resist on the top. In order to access the top of the pillar, the lift-off process is used. For the lift-off process the same ultrasonic bath was used and set to similar conditions [4].

[4] It was found that this lift-off process is challenging. For the best results, the temperature and ultrasonic power has to be optimized for the specific devices used. In addition, freshly (less than 24h) deposited and exposed photoresist was easier to remove than the older one.

An image presented in Fig. 5.6 shows a comparison between covered (unsuccessful) and uncovered (successful) results. Note, that thick insulating materials (such as used photoresist) appear bright in the SEM. That is because the electrons are reflected more effectively from these surfaces, which results in a higher signal at the detector.

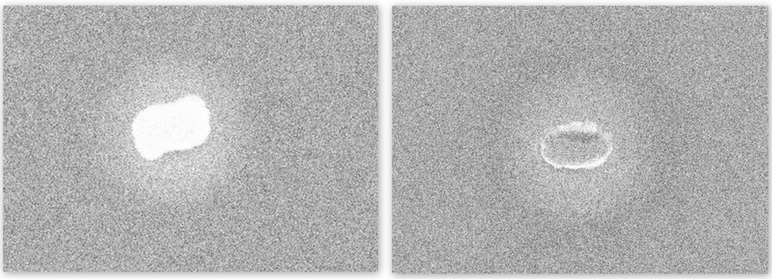

Figure 5.6: An unsuccessful (left) and successful (right) lift-off procedure of the MTJ nanopillar.

Finally, the top conducting bi-layer of 5 nm Ta and 50 nm Au was sputtered on the whole wafer. The third exposure step, defining the top electrode was similar to the bottom electrode definition, with etching terminated on the Ta_2O_5 oxide layer. The final mask is presented in Fig. 5.7. After removing resist residuals, the sample is ready for measurement. An image summarizing the nanolithography process is presented in Fig. 5.8

The procedure described above presents a three-step lithography process. Alternatively, in some cases, the bottom electrode definition step and the first ion-beam milling can be omitted, in order to prepare samples using a simple, two-step process. Before the etching of the MTJ nanopillar, however, some parts of the sample (typically a few mm-wide strip around the edge of the sample)

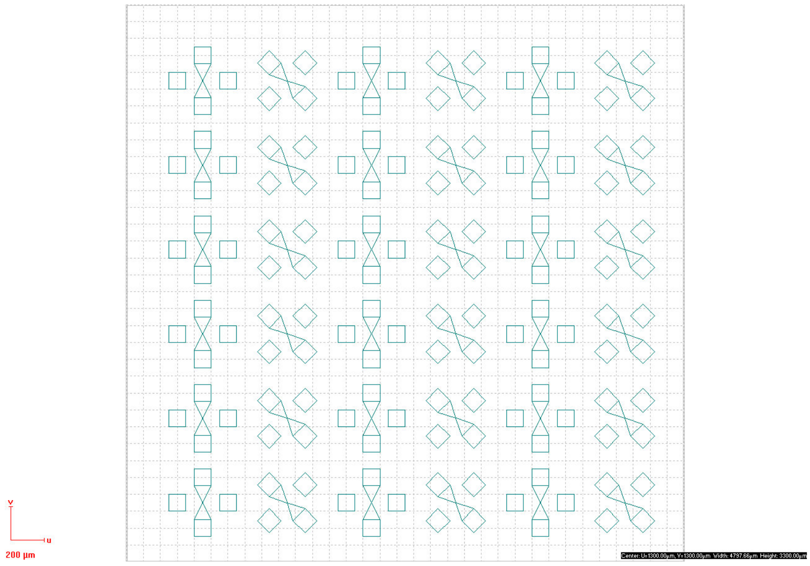

Figure 5.7: The final mask design for the nano-lithography process with top electrodes.

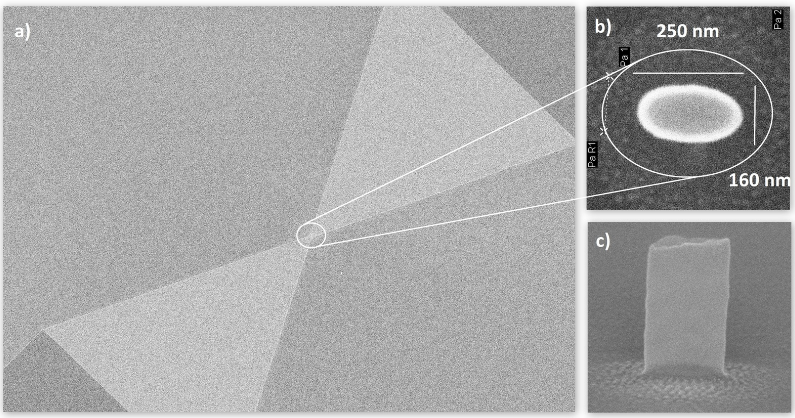

Figure 5.8: SEM images of a nanopillar fabrication process - (a) bottom electrode, (b) nanopillar MTJ from the top and (c) from the side.

must be protected from the ion-beam milling, for example by covering it with a permanent marker. As a result of this approach, MTJ structures with a common bottom electrode are prepared. The electrical contact to the bottom electrode is realized, by contacting the area, which was protected from etching. Note that only a quasi-static measurement can be used in the two-step process (see section 5.3 for details) as the common bottom electrode increases the electric capacitance of the sample. For the three-step process, the capacitance of the device was calculated using a parallel-plate capacitor model $C = \epsilon_r \epsilon_0 A/d$, where ϵ_r and ϵ_0 are the relative and absolute dielectric constants of the Al_2O_3 insulator surrounding the MTJ (the capacity of the MTJ itself is ignored) and d is the Al_2O_3 layer thickness. The overlap between the top and bottom leads of about 4 μm^2, results in a capacitance of less than 1×10^{-14} F, which is important for high frequency measurements. Assuming that the resistance of the MTJ is typically $R = 1$ kOhm, then the time constant can be calculated from an Eq. $t_c = RC$, which in this case is $t_c = 1 \times 10^{-11}$ s. This implies that for used devices, parasitic effects associated with a sample geometry can be ignored for frequencies below a cut-off frequency of $f_c < 1/(2\pi t_c) \approx 16$GHz.

5.3 Experimental methods

This section provides a description of the experimental methods used for electric measurements in this thesis. A detailed description of the magnetometers used - VSM and MOKE can be found in Ref. [5]. The CIPT method is explained in detail in Ref. [6]. Typically, a few mm rectangular sized samples for magnetic and structural measurements were cut from a 4-inch wafer using a diamond knife.

[5] Wrona, J. *PhD thesis*. AGH University of Science and Technology, (2002)

[6] Worledge, D. C. and Trouilloud, P. L. *Applied Physics Letters* **83**(1), 84 (2003)

5.3.1 Quasi-static electrical transport measurement setup

The entire setup uses the following equipment:

- EG&G Lock-in Amplifier 5209,
- GMW 3470 electromagnet,
- Kepco power supply BOP 3612M / Bouhnik power supply,
- Lakeshore 475 DSP Gaussmeter / Cryomagnetics GM-700,
- Keithley Sourcemeter 2636,
- Agilent Generator 81150,
- Agilent Multimeter 34401,
- Home-build dedicated electronic adder and I-V converter,
- Cascade DCM-100 four-probe system,
- Janis cryogen-free micromanipulated probe station with electromagnet CCR10-1-(2TXKEL-2MW40)-0.55T.

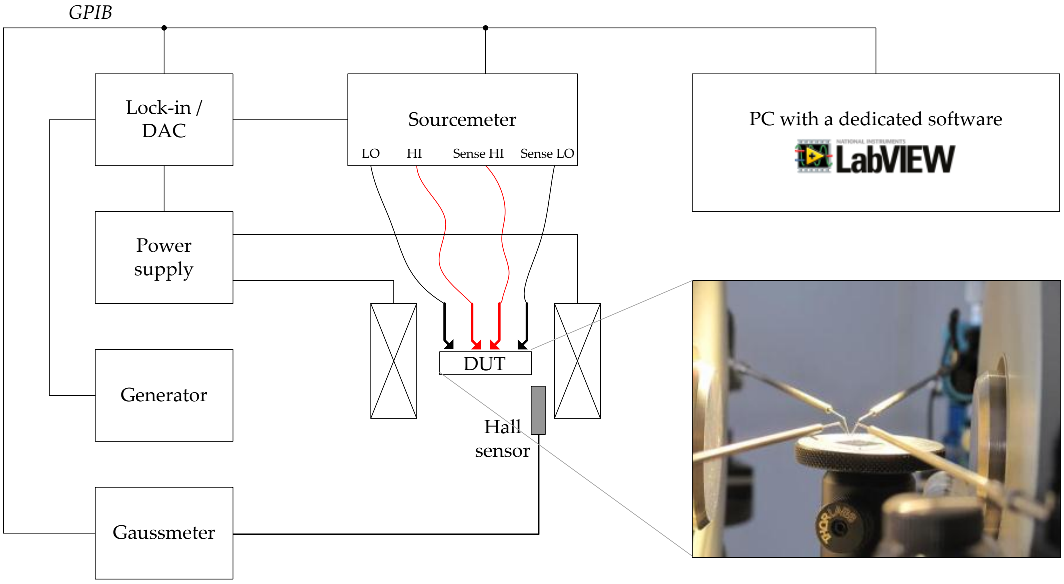

Figure 5.9: The schematics of the quasi-static transport measurement setup.

The magnetic field is generated by the electromagnet supplied from the power supply, which is controlled by the lock-in amplifier using a DAC converter. DC or pulsed current or voltage is sourced by the sourcemeter, which measures the DC voltage, current and resistance. The simple schematics of the setup used for the magneto-transport measurements is presented in Fig. 5.9. An electrical contact with a sample is provided by using a four-probe system. Alternatively, the sample is placed on the cold finger of the cryostat micromanipulated probe station from Janis. This type of system enables basic magneto-transport characterization of a patterned multilayer sample, including, TMR at different bias conditions, I-V or pulsed I-V in the external magnetic field, or CIMS.

DAC - digital to analogue converter

In addition, by using a signal generator that supplies the DUT (in this case a single MTJ) in combination with a synchronized lock-in amplifier and I-V converter, it is possible to measure the dynamic conductance vs. voltage directly, in the presence of the magnetic field.

DUT - device under test

For the magnetic field sensor, a special measurement mode was developed, which enables direct sensitivity measurement. In these experiments, the magnetic field sensor is placed in a sinusoidal magnetic field (typically of the amplitude of H_{AC} = 0.5 Oe). This produced an AC output signal proportional to the sensitivity of the sensor, which is measured directly by using lock-in detection with synchronization to a sinusoidal magnetic field on top of a bias field.

The entire setup is automated in dedicated LabVIEW software[7]. A detailed manual for the experimental setup is provided separately.

[7] Skowroński, W. *MSc thesis*. AGH University of Science and Technology, (2008)

5.3.2 *The dynamic transport measurement setup*

In order to measure the dynamic properties of the patterned MTJ nanopillar, the following additional RF equipment is used:

- Agilent RF Generator E8257D,
- Agilent Signal Analyzer N9030A,
- Mini-circuits Bias-T ZX85-12G+ .

The RF generator is used in the spin-torque diode effect setup, discussed in detail in section 3.3. The RF signal is supplied to the MTJ sample via the RF-terminal of the bias-T using the SMA cables. The DC (V_{mix}) signal on the dc-terminals of the bias-T is measured by using the lock-in amplifier, synchronized with AM modulated (at the frequency of 8 kHz) signals from the RF generator. On the top of the RF-signal, a DC bias sourced from a sourcemeter is also supplied on the DC-terminal of the bias-T. The sample is connected to a sum-terminal of the bias-T.

SMA - SubMiniature version A

AM - amplitude modulation

The sample was mounted on a dedicated sample holder with a CPW designed to operate in a broad frequency range up to 20 GHz. A CPW was fabricated from a Duroid 6010.2LM-0250-1E PCB laminate from Rogers Corporation. This laminate consist of a 635 μm thick duroid dielectric (ϵ_r = 10.2 +/- 0.25) covered on both sides with a 35 μm thick Cu layer. An example of the CPW design used for the PIMM setup, with the dimensions calculated using a TXline[8] software, is presented in Fig. 5.10.

CPW - coplanar wave guide

PCB - printed circuit board

[8] http://www.awrcorp.com

The electrical connections are realized using bonding wires. Alternatively, the MTJ sample can be connected using a special RF-probe with a G-S configuration from Picoprobe, mounted inside the Janis probe station, presented in Fig. 5.11.

G-S - ground-signal configuration

The RF measurement setup schematics are presented in Fig. 5.11.

An inverse effect, that is oscillations generated by the MTJ supplied with a DC signal, as discussed in section 3.5, are measured using a spectrum analyzer. In this setup, the RF signal is connected to the analyzer by using SMA cables to the RF-terminals of the bias-T. The DC bias is supplied in the same way as in the spin-torque diode setup. It was found that the STO signals obtained for the setup using bonding-wire connections have an increased amplitude for frequencies below 200 MHz with respect to the signals measured using an RF-probe, which is due to an additional noise influence. Above this frequency the obtained STO measurement was similar to the RF-probe and bonding-wires.

The measurement setup showing most of the devices is presented in the photograph below - Fig. 5.12.

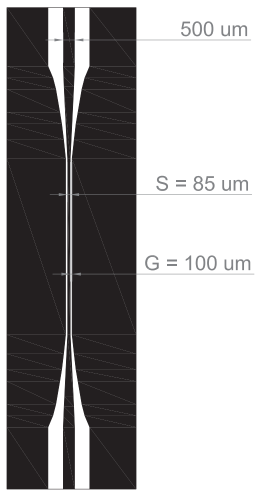

Figure 5.10: The CPW design for the PIMM setup.

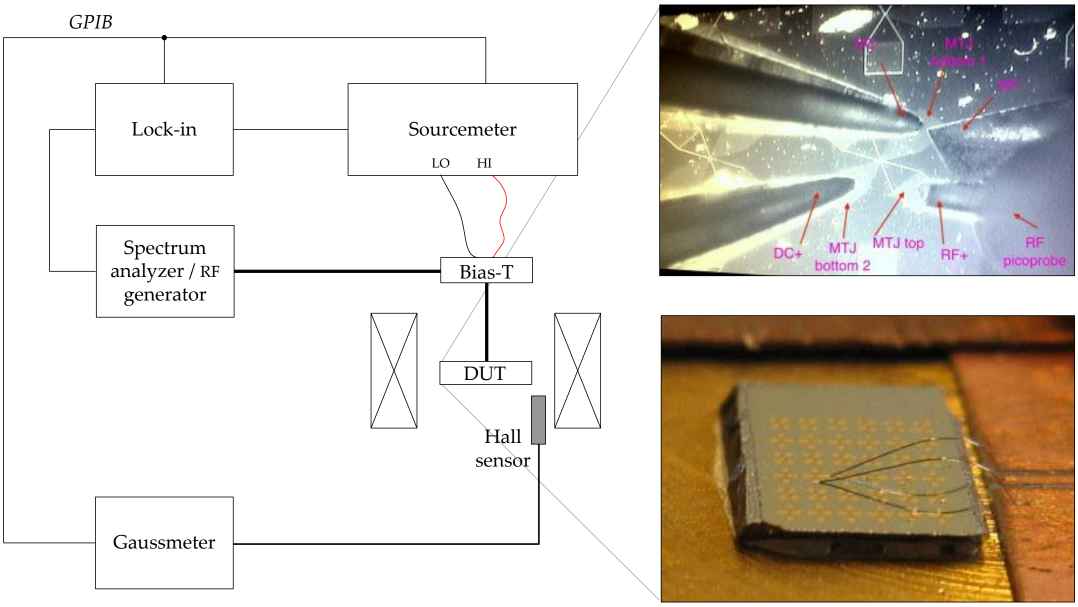

Figure 5.11: The schematics of the RF measurement setup. The power supply and PC are skipped for clarity. The upper photograph shows the MTJ sample mounted in a Janis setup with an RF probe tip. The lower photograph shows the MTJ sample mounted on a dedicated sample holder with the bonding wires.

5.3.3 *The pulse inductive microwave magnetometer*

Results presented in section 3.2 were obtained by using the PIMM setup in cooperation with Dr. Santiago Serrano-Guisan and prof. Hans Schumacher from PTB Braunschweig.

The setup was based on an instrument described in detail in ref. [9]. Fast 10 V voltage pulse, with a rise-time of 65 ps was generated by a Picosecond Pulse Labs Generator, model 10070A. The pulse was fed through a CPW to the sampling oscilloscope Agilent 86100D with a 20 GHz bandwidth. The CPW was designed using the same PCB board described in the section on 5.3.2. The CPW with ground was designed using a G-S-G configuration with an 85 μm wide signal line and the gap between the ground plane of 100 μm. The CPW was connected using SMA terminals at both ends of the PCB, where the signal line is wider - Fig. 5.10. In this case, the signal line has to be as narrow as possible, in order to generate a significant magnetic field pulse. The lithograph process used with wet-etching limited a minimum signal line width to about 100 μm. This design ensured a magnetic field pulse of a few Oe on the top of the CPW, which was able to excite the magnetization precession in the multilayer thin-film placed on it. The magnetic field along an easy magnetization axis (bias field) and hard axis (reference field) were applied from Helmholtz coils controlled with power supplies.

The measurement procedure consists of obtaining the magnetization precession signal excited by the fast magnetic pulse at given static magnetic field applied along a bias field direction using a sampling oscilloscope. From each measurement a reference signal was subtracted, which was obtained by a similar method, how-

[9] Kos, A. B., Silva, T. J., and Kabos, P. *Review of Scientific Instruments* **73**(10), 3563 (2002)

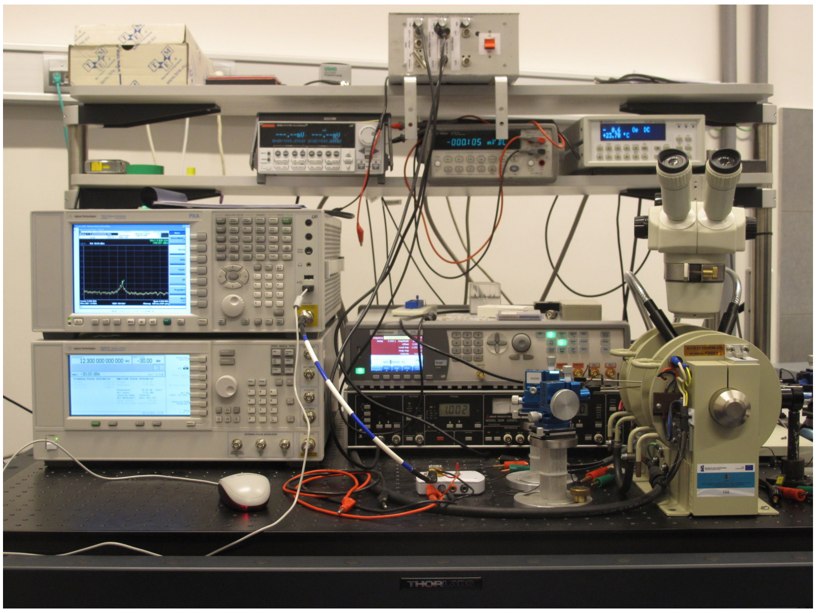

Figure 5.12: A photograph of the DC and RF electrical transport measurement setup.

ever, with the presence of strong reference field, which suppresses a magnetization motion. After this procedure, a series of measurements in investigated static magnetic field range was obtained, similar to the one presented in Fig. 3.10.

The measurement setup block diagram is presented in Fig. 5.13.

5.3.4 *Noise measurement setup*

The electric noise was measured with a home-built setup, based on that presented in Ref. [10]. The sample was mounted on a DIL24 chip carrier using silver paste. A two-point connection was realized using Al-wire bonding. The chip carrier with the bonded MTJ was placed in a dedicated socket, between electromagnet cores placed inside a metal box. The electromagnet was supplied from a battery source, and the strength of the magnetic field was set by a potentiometer connected in series. The maximum field that can be applied in this setup is +/- 90 Oe.

[10] Ferreira, R., Wiśniowski, P., Freitas, P. P., Langer, J., Ocker, B., and Maass, W. *Journal of Applied Physics* **99**(8), 08K706 (2006)

The MTJ under test was biased with a voltage sourced from an additional battery set, also controlled with a potentiometer. In addition, the MTJ connections were fed to low noise FEMTO DLPVA-100-B-S voltage amplifiers set to 60dB gain. The output of the amplifier was connected to a PXIe-6124 4MS/s 16-bit DAQ card installed in a National Instruments PXI computer.

In addition, using a SMU-4132 (sourcemeter) card and the power supply controlled with a DAC output of PXIe-6124 DAQ card, it was possible to measure simple magneto-transport properties (such as the TMR and I-V curves) of the bonded MTJ, similar to the main setup described in the section on the 5.3.1. The measurement setup block diagram is presented in Fig. 5.14.

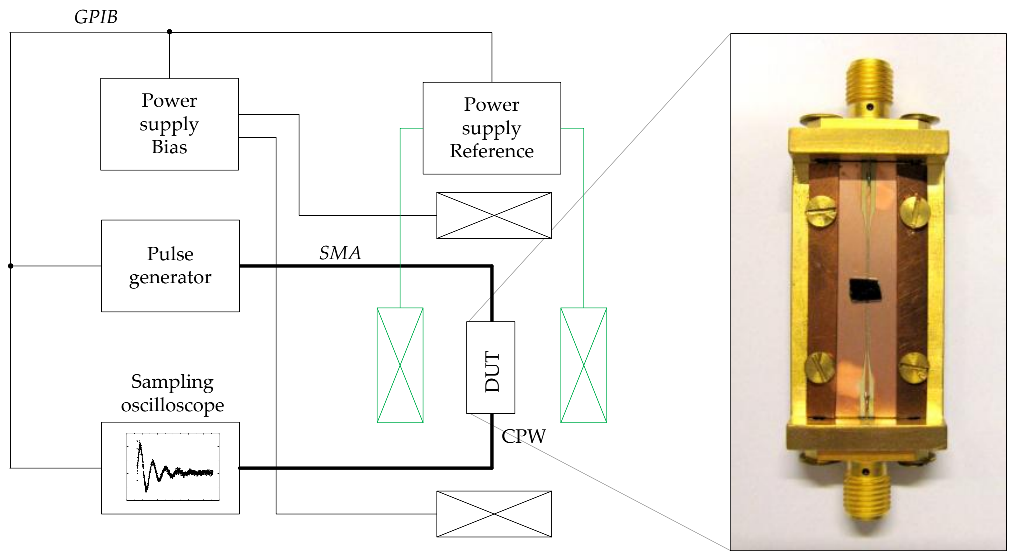

Figure 5.13: The PIMM setup block diagram. The photograph on the righthand side shows the fabricated CPW with the MTJ sample on the top.

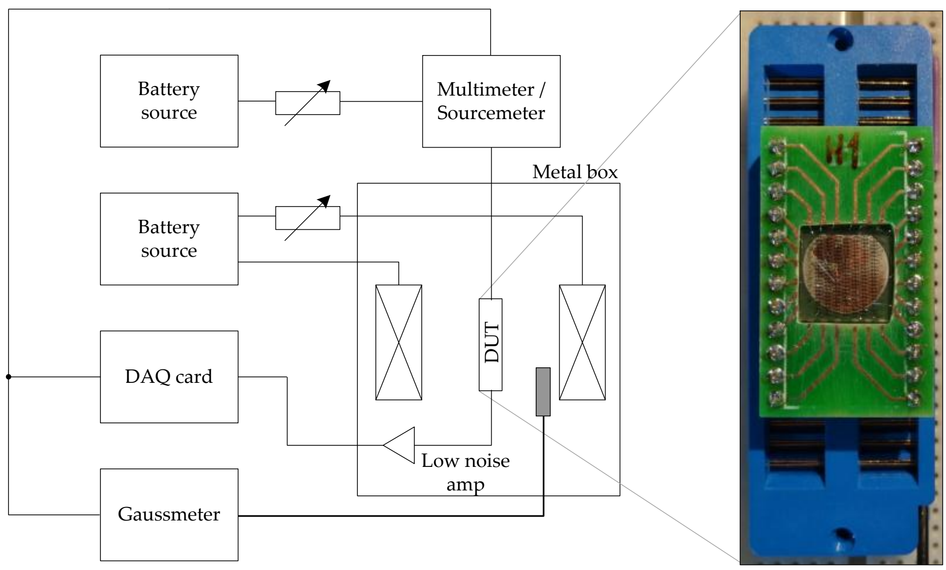

Figure 5.14: The schematics of the noise measurement setup.

Bibliography

1. Almeida, J. M., Ferreira, R., Freitas, P. P., Langer, J., Ocker, B., and Maass, W. *Journal of Applied Physics* **99**(8), 08B314 (2006).

2. Baibich, M. N., Broto, J. M., Fert, A., Van Dau, F. N., Petroff, F., Etienne, P., Creuzet, G., Friederich, A., and Chazelas, J. *Physical Review Letters* **61**(21), 2472 (1988).

3. Berger, L. *Physical Review B* **54**(13), 9353 (1996).

4. Boulle, O., Cros, V., Grollier, J., Pereira, L. G., Deranlot, C., Petroff, F., Faini, G., Barnaś, J., and Fert, A. *Nature Physics* **3**(7), 492 (2007).

5. Butler, W., Zhang, X., Schulthess, T., and MacLaren, J. *Physical Review B* **63**(5), 054416 (2001).

6. Chanthbouala, A., Matsumoto, R., Grollier, J., Cros, V., Anane, A., Fert, A., Khvalkovskiy, A. V., Zvezdin, K. A., Nishimura, K., Nagamine, Y., Maehara, H., Tsunekawa, K., Fukushima, A., and Yuasa, S. *Nature Physics* **7**, 626 (2011).

7. Cornelissen, S., Bianchini, L., Devolder, T., Kim, J., Roy, W. V., Lagae, L., and Chappert, C. *Physical Review B* **81**(14), 144408 (2010).

8. Cornelissen, S., Bianchini, L., Helmer, A., Devolder, T., Kim, J., de Beeck, M. O., Roy, W. V., Lagae, L., and Chappert, C. *Journal of Applied Physics* **105**(7), 07B903 (2009).

9. Czapkiewicz, M. *PhD thesis*. AGH University of Science and Technology, (1999).

10. Deac, A. M., Fukushima, A., Kubota, H., Maehara, H., Suzuki, Y., Yuasa, S., Nagamine, Y., Tsunekawa, K., Djayaprawira, D. D., and Watanabe, N. *Nature Physics* **4**(10), 803 (2008).

11. Devolder, T., Bianchini, L., Kim, J., Crozat, P., Chappert, C., Cornelissen, S., de Beeck, M. O., and Lagae, L. *Journal of Applied Physics* **106**(10), 103921 (2009).

12. Dieny, B., Speriosu, V. S., Gurney, B. A., Parkin, S. S. P., Wilhoit, D. R., Roche, K. P., Metin, S., Peterson, D. T., and Nadimi, S. *Journal of Magnetism and Magnetic Materials* **93**, 101 (1991).

13. Djayaprawira, D. D., Tsunekawa, K., Nagai, M., Maehara, H., Yamagata, S., Watanabe, N., Yuasa, S., Suzuki, Y., and Ando, K. *Applied Physics Letters* **86**(9), 092502 (2005).

14. Drewello, V., Schmalhorst, J., Thomas, A., and Reiss, G. *Physical Review B* **77**(1) (2008).

15. Endo, M., Kanai, S., Ikeda, S., Matsukura, F., and Ohno, H. *Applied Physics Letters* **96**(21), 212503 (2010).

16. Engel-Herbert, R. and Hesjedal, T. *Journal of Applied Physics* **97**(7), 074504 (2005).

17. Faure-Vincent, J., Tiusan, C., Bellouard, C., Popova, E., Hehn, M., Montaigne, F., and Schuhl, A. *Physical Review Letters* **89**(10), 107206 (2002).

18. Ferreira, R., Wiśniowski, P., Freitas, P. P., Langer, J., Ocker, B., and Maass, W. *Journal of Applied Physics* **99**(8), 08K706 (2006).

19. Frankowski, M. *MSc thesis*. AGH University of Science and Technology, (2012).

20. Gilbert, T. *Physical Review* **8**, 153 (1955).

21. Grünberg, P. A., Schreiber, R., and Pang, Y. *Physical Review Letters* **57**(19), 2442 (1986).

22. Hayakawa, J., Ikeda, S., Lee, Y. M., Sasaki, R., Meguro, T., Matsukura, F., Takahashi, H., and Ohno, H. *Japanese Journal of Applied Physics* **45**(40), L1057 (2006).

23. Heiliger, C. and Stiles, M. *Physical Review Letters* **100**(18) (2008).

24. Helmer, A., Cornelissen, S., Devolder, T., Kim, J. V., van Roy, W., Lagae, L., and Chappert, C. *Physical Review B* **81**(9), 94416 (2010).

25. Herranz, D., Gomez-Ibarlucea, A., Schafers, M., Lara, A., Reiss, G., and Aliev, F. G. *Applied Physics Letters* **99**(6), 062511 (2011).

26. Hooge, F. N. *Physica B+C,* **83**, 14 (1976).

27. Houssameddine, D., Ebels, U., Delaët, B., Rodmacq, B., Firastrau, I., Ponthenier, F., Brunet, M., Thirion, C., Michel, J., Prejbeanu-Buda, L., Cyrille, M., Redon, O., and Dieny, B. *Nature Materials* **6**(6), 447 (2007).

28. Huai, Y., Albert, F., Nguyen, P., Pakala, M., and Valet, T. *Applied Physics Letters* **84**(16), 3118 (2004).

29. Ikeda, S., Hayakawa, J., Ashizawa, Y., Lee, Y. M., Miura, K., Hasegawa, H., Tsunoda, M., Matsukura, F., and Ohno, H. *Applied Physics Letters* **93**(8), 082508 (2008).

30. Ikeda, S., Miura, K., Yamamoto, H., Mizunuma, K., Gan, H. D., Endo, M., Kanai, S., Hayakawa, J., Matsukura, F., and Ohno, H. *Nature Materials* **9**(9), 721 (2010).

31. Ingvarsson, S., Xiao, G., Parkin, S. S. P., Gallagher, W. J., Grinstein, G., and Koch, R. H. *Physical Review Letters* **85**(15), 3289 (2000).

32. Itoh, H. *Journal of Physics D: Applied Physics* **40**, 1228 (2007).

33. Jia, X., Xia, K., Ke, Y., and Guo, H. *Physical Review B* **84**(1), 014401 (2011).

34. Jiang, L., Nowak, E., Scott, P., Johnson, J., Slaughter, J., Sun, J., and Dave, R. *Physical Review B* **69**(5), 054407 (2004).

35. Julliere, M. *Physics Letters* **54A**(3), 225 (1975).

36. Kajiwara, Y., Harii, K., Takahashi, S., Ohe, J., Uchida, K., Mizuguchi, M., Umezawa, H., Kawai, H., Ando, K., Takanashi, K., Maekawa, S., and Saitoh, E. *Nature* **464**(7286), 262 March (2010).

37. Kanak, J. *PhD thesis*. AGH University of Science and Technology, (2006).

38. Katayama, T., Yuasa, S., Velev, J., Zhuravlev, M. Y., Jaswal, S. S., and Tsymbal, E. Y. *Applied Physics Letters* **89**(11), 112503 (2006).

39. Khajetoorians, A. A., Wiebe, J., Chilian, B., and Wiesendanger, R. *Science* **332**(6033), 1062 (2011).

40. Khalili Amiri, P., Zeng, Z. M., Upadhyaya, P., Rowlands, G., Zhao, H., Krivorotov, I. N., Wang, J., Jiang, H. W., Katine, J. A., Langer, J., Galatsis, K., and Wang, K. L. *IEEE Electron Device Letters* **32**(1), 57 (2011).

41. Kiselev, S. I., Sankey, J. C., Krivorotov, I. N., Emley, N. C., Schoelkopf, R. J., Buhrman, R. A., and Ralph, D. C. *Nature* **425**(6956), 380 (2003).

42. Kittel, C. *Phys. Rev.* **71**, 270 (1947).

43. Kools, J. C. S., Kula, W., Mauri, D., and Lin, T. *Journal of Applied Physics* **85**, 4466 (1999).

44. Kos, A. B., Silva, T. J., and Kabos, P. *Review of Scientific Instruments* **73**(10), 3563 (2002).

45. Kubota, H., Ando, Y., Miyazaki, T., Reiss, G., Brückl, H., Schepper, W., Wecker, J., and Gieres, G. *Journal of Applied Physics* **94**(3), 2028 (2003).

46. Kubota, H., Fukushima, A., Ootani, Y., Yuasa, S., Ando, K., Maehara, H., Tsunekawa, K., Djayaprawira, D. D., Watanabe, N., and Suzuki, Y. *Applied Physics Letters* **89**(3), 032505 (2006).

47. Kubota, H., Fukushima, A., Yakushiji, K., Nagahama, T., Yuasa, S., Ando, K., Maehara, H., Nagamine, Y., Tsunekawa, K., Djayaprawira, D. D., Watanabe, N., and Suzuki, Y. *Nature Physics* **4**(1), 37 (2007).

48. Landau, L. D. and Lifshitz, E. *Phys. Z. Sowietunion* **100**, 1243 (1935).

49. Lee, K., Deac, A., Redon, O., Noziéres, J., and Dieny, B. *Nature Materials* **3**(12), 877 (2004).

50. Lei, Z. Q., Li, G. J., Egelhoff, W. F., Lai, P. T., and Pong, P. W. T. *IEEE Transactions on Magnetics* **47**(3), 602 (2011).

51. Liu, L., Pai, C.-F., Li, Y., Tseng, H. W., Ralph, D. C., and Buhrman, R. A. *Science* **336**(6081), 555 (2012).

52. MacLaren, J. M., Zhang, X. G., and Butler, W. H. *Physical Review B* **56**(18), 11827 (1997).

53. Maruyama, T., Shiota, Y., Nozaki, T., Ohta, K., Toda, N., Mizuguchi, M., Tulapurkar, A. A., Shinjo, T., Shiraishi, M., Mizukami, S., Ando, Y., and Suzuki, Y. *Nature Nanotechnology* **4**(3), 158 (2009).

54. Mathon, J. *Contemporary Physics* **32**(3), 143 (1991).

55. Mathon, J. *Physical Review B* **56**(18), 11810 (1997).

56. Matsumoto, R., Chanthbouala, A., Grollier, J., Cros, V., Fert, A., Nishimura, K., Nagamine, Y., Maehara, H., Tsunekawa, K., Fukushima, A., and Yuasa, S. *Applied Physics Express* **4**(6), 063001 (2011).

57. Min, T., Chen, Q., Beach, R., Jan, G., Horng, C., Kula, W., Torng, T., Tong, R., Zhong, T., Tang, D., Wang, P., Chen, M.-m., Sun, J. Z., Debrosse, J. K., Worledge, D. C., Maffitt, T. M., and Gallagher, W. J. *IEEE Transactions on Magnetics* **46**(6), 2322 (2010).

58. Moodera, J. and Mathon, G. *Journal of Magnetism and Magnetic Materials* **200**, 248 (1999).

59. Néel. *Comptes. Rendus* **255**, 1676 (1962).

60. Nogues, J. and Schuller, I. K. *Journal of Magnetism and Magnetic Materials* **192**, 203 (1999).

61. Ogrodnik, P., Wilczyński, M., Barnaś, J., and Świrkowicz, R. *IEEE Transactions on Magnetics* **47**(6), 1627 (2011).

62. Paluskar, P., Attema, J., de Wijs, G., Fiddy, S., Snoeck, E., Kohlhepp, J., Swagten, H., de Groot, R., and Koopmans, B. *Physical Review Letters* **100**(5) February (2008).

63. Parkin, S. S. P., More, N., and Roche, K. P. *Physical Review Letters* **64**(19), 2304 (1990).

64. Pribiag, V. S., Krivorotov, I. N., Fuchs, G. D., Braganca, P. M., Ozatay, O., Sankey, J. C., Ralph, D. C., and Buhrman, R. A. *Nature Physics* **3**(7), 498 (2007).

65. Read, J. C., Cha, J. J., Egelhoff, W. F., Tseng, H. W., Huang, P. Y., Li, Y., Muller, D. A., and Buhrman, R. A. *Applied Physics Letters* **94**(11), 112504 (2009).

66. Rijks, T. G. S. M., Coehoorn, R., Daemen, J. T. F., and de Jonge, W. J. M. *Journal of Applied Physics* **76**(2), 1092 (1994).

67. Rippard, W. H., Deac, A. M., Pufall, M. R., Shaw, J. M., Keller, M. W., Russek, S. E., and Serpico, C. *Physical Review B* **81**(1), 014426 (2010).

68. Rodriguez-Suárez, R., Rezende, S., and Azevedo, A. *Physical Review B* **71**(22), 224406 (2005).

69. Sankey, J., Braganca, P., Garcia, A., Krivorotov, I., Buhrman, R., and Ralph, D. *Physical Review Letters* **96**(22) (2006).

70. Sankey, J. C., Cui, Y., Sun, J. Z., Slonczewski, J. C., Buhrman, R. A., and Ralph, D. C. *Nature Physics* **4**(1), 67 (2007).

71. Serrano-Guisan, S., Rott, K., Reiss, G., Langer, J., Ocker, B., and Schumacher, H. *Physical Review Letters* **101**(8) (2008).

72. Serrano-Guisan, S., Skowroński, W., Wrona, J., Liebing, N., Czapkiewicz, M., Stobiecki, T., Reiss, G., and Schumacher, H. W. *Journal of Applied Physics* **110**(2), 023906 (2011).

73. Shiota, Y., Nozaki, T., Bonell, F., Murakami, S., Shinjo, T., and Suzuki, Y. *Nature Materials* **11**(1), 39 November (2011).

74. Silva, T. J., Lee, C. S., Crawford, T. M., and Rogers, C. T. *Journal of Applied Physics* **85**(11), 7849 (1999).

75. Skowroński, W., , Wiśniowski, P., Stobiecki, T., Cardoso, S., Freitas, P. P., and van Dijken, S. *Applied Physics Letters* **101**(19), 192401 (2012).

76. Skowroński, W. *MSc thesis*. AGH University of Science and Technology, (2008).

77. Skowroński, W., Stobiecki, T., Wrona, J., Reiss, G., and van Dijken, S. *Applied Physics Express* **5**(6), 063005 (2012).

78. Skowroński, W., Stobiecki, T., Wrona, J., Rott, K., Thomas, A., Reiss, G., and van Dijken, S. *Journal of Applied Physics* **107**(9), 093917 (2010).

79. Slonczewski, J. C. *Journal of Magnetism and Magnetic Materials* **159**(1-2), L1 (1996).

80. Slonczewski, J. C. *Physical Review B* **39**(10), 6995 (1989).

81. Slonczewski, J. C. and Sun, J. Z. *Journal of Magnetism and Magnetic Materials* **310**(2), 169 (2007).

82. Stobiecki, T., Kanak, J., Wrona, J., Reiss, G., and Brückl, H. *Journal of Magnetism and Magnetic Materials* **316**(2), e998 September (2007).

83. Stoner, E. C. and Wohlfarth, E. P. *Phil. Trans. R. Soc. Lond. A* **240**, 599 (1948).

84. Sun, J. J. and Freitas, P. P. *Journal of Applied Physics* **85**, 5264 (1999).

85. Sun, J. Z. *Physical Review B* **62**(1), 570 (2000).

86. Sun, J. Z., Gaidis, M. C., Hu, G., O'Sullivan, E. J., Brown, S. L., Nowak, J. J., Trouilloud, P. L., and Worledge, D. C. *Journal of Applied Physics* **105**(7), 07D109 (2009).

87. Suzuki, D., Natsui, M., Ikeda, S., Hasegawa, H., Miura, K., Hayakawa, J., Endoh, T., Ohno, H., and Hanyu, T. In *VLSI Circuits, 2009 Symposium on*, 80, (2009).

88. Takemura, R., Kawahara, T., Miura, K., Yamamoto, H., Hayakawa, J., Matsuzaki, N., Ono, K., Yamanouchi, M., Ito, K., Takahashi, H., Ikeda, S., Hasegawa, H., Matsuoka, H., and Ohno, H. *IEEE Journal of Solid-State Circuits* **45**(4), 869 (2010).

89. Tedrow, P. M. and Meservey, R. *Physical Review B* **7**(1), 318 (1973).

90. Tsymbal, E. Y., Mryasov, O. N., and LeClair, P. *Journal of Physics: Condensed Matter* **15**(4), R109 (2003).

91. Tulapurkar, A. A., Suzuki, Y., Fukushima, A., Kubota, H., Maehara, H., Tsunekawa, K., Djayaprawira, D. D., Watanabe, N., and Yuasa, S. *Nature* **438**(7066), 339 (2005).

92. Tumański, S. *Thin film magnetoresistive sensors*. IOP Publishing, Bristol, (2001).

93. Ventura, J., Teixeira, J., Araujo, J., Sousa, J., Wiśniowski, P., and Freitas, P. *Physical Review B* **78**(2), 024403 (2008).

94. Wada, T., Yamane, T., Seki, T., Nozaki, T., Suzuki, Y., Kubota, H., Fukushima, A., Yuasa, S., Maehara, H., Nagamine, Y., Tsunekawa, K., Djayaprawira, D. D., and Watanabe, N. *Physical Review B* **81**(10), 104410 (2010).

95. Wang, C., Cui, Y., Sun, J., Katine, J., Buhrman, R., and Ralph, D. *Physical Review B* **79**(22), 224416 (2009).

96. Wang, W.-G., Li, M., Hageman, S., and Chien, C. L. *Nature Materials* **11**(1), 64 (2011).

97. Weisheit, M., Fahler, S., Marty, A., Souche, Y., Poinsignon, C., and Givord, D. *Science* **315**(5810), 349 (2007).

98. Wilczyński, M. *Journal of Magnetism and Magnetic Materials* **323**(11), 1529–1536 June (2011).

99. Wilgocka-Ślęzak, D., Freindl, K., Kozioł, A., Matlak, K., Rams, M., Spiridis, N., Ślęzak, M., Ślęzak, T., Zając, M., and Korecki, J. *Phys. Rev. B* **81**, 064421 (2010).

100. Wiśniowski, P., Almeida, J. M., Cardoso, S., Barradas, N. P., and Freitas, P. P. *Journal of Applied Physics* **103**(7), 07A910 (2008).

101. Worledge, D. C. and Trouilloud, P. L. *Applied Physics Letters* **83**(1), 84 (2003).

102. Wrona, J. *PhD thesis*. AGH University of Science and Technology, (2002).

103. Wrona, J., Langer, J., Ocker, B., Maass, W., Kanak, J., Stobiecki, T., and Powroźnik, W. *Journal of Physics: Conference Series* **200**, 052032 (2010).

104. Yakata, S., Kubota, H., Suzuki, Y., Yakushiji, K., Fukushima, A., Yuasa, S., and Ando, K. *Journal of Applied Physics* **105**(7), 07D131 (2009).

105. Yang, H. X., Chshiev, M., Kalitsov, A., Schuhl, A., and Butler, W. H. *Applied Physics Letters* **96**(26), 262509 (2010).

106. Yuasa, S. and Djayaprawira, D. D. *Journal of Physics D: Applied Physics* **40**, R337 (2007).

107. Zhou, Y., Akerman, J., and Sun, J. Z. *Applied Physics Letters* **98**(10), 102501 (2011).

108. Zhou, Y., Bonetti, S., Zha, C. L., and Akerman, J. *New Journal of Physics* **11**, 103028 (2009).

109. Zhuravlev, M. Y., Velev, J., Vedyayev, A. V., and Tsymbal, E. Y. *Journal of Magnetism and Magnetic Materials* **300**(1), e277 (2006).

Total number of citations: **109**. *The numbers in the bibliography list (alphabetic order) do not correspond to the numbers used in the main text.*